DEVELOPMENT OF BI-FUNCTIONAL ZEOLITE-BASED CATALYSTS FOR METHANE DEHYDROAROMATIZATION

by

Yungchieh Lai

Bachelor of Science, Chemical Engineering, National Taiwan University, 2008

Master of Science, Chemical Engineering, University of Pittsburgh, 2012

Submitted to the Graduate Faculty of

Swanson School of Engineering in partial fulfillment

of the requirements for the degree of

Doctor of Philosophy

University of Pittsburgh

2015

UNIVERSITY OF PITTSBURGH

SWANSON SCHOOL OF ENGINEERING

This dissertation was presented

by

Yungchieh Lai

It was defended on

September 1, 2015

and approved by

Robert Enick, Ph.D., Professor, Department of Chemical and Petroleum Engineering

John Keith, Ph.D., Assistant Professor, Department of Chemical and Petroleum Engineering

Jill Millstone, Ph.D., Assistant Professor, Department of Chemistry

Dissertation Director: Götz Veser, Ph.D., Professor, Department of Chemical and Petroleum Engineering

DEVELOPMENT OF BI-FUNCTIONAL ZEOLITE-BASED CATALYSTS FOR METHANE DEHYDROAROMATIZATION

Yungchieh Lai, PhD

University of Pittsburgh, 2015

Benzene is one of the most important organic intermediates in the petrochemical industry. Direct methane dehydroaromatization (DHA) under non-oxidative environment has been shown to be a promising pathway to produce benzene since Mo/HZSM-5 was reported as a viable catalyst in 1993. The reaction over this catalyst is generally accepted to proceed via a synergistic mechanism between the metal sites (i.e. MoO_xC_y) and the Bronsted acid sites (BAS) of HZSM-5. The high benzene selectivity is attributed to the similarity in pore size of ZSM-5 with the dynamic molecular size of benzene. However, diffusion of large benzene molecules inside the zeolite micropores also enhances the chance for undesired further reactions on the BAS, resulting in coking and hence deactivation of the catalyst. While the catalyst can be regenerated via burn-off of the coke in an oxidative environment, this burn-off also results in oxidation of the Mo species, and thus requires a (re-)activation period to convert Mo back into its active oxicarbide form. This catalyst deactivation via coking combined with the lengthy reactivation of the catalyst pose a significant hurdle for economic viability of the process.

The objective of this research is to develop a new bi-functional zeolite-based (metal) catalyst that is highly stable while maintaining the high benzene yield from DHA. Towards this goal, we aimed to investigate systematically how the catalytic performance is affected by changes in i) metal sites and ii) porosity of HZSM-5.

To study the impact of the metal site in the zeolite, Zn-HZSM-5 and Fe-HZSM-5 catalysts with different metal dispersion was prepared via different synthetic routes and the structural properties of the catalysts were correlated to their catalytic performance. We found that only well dispersed metal species located within the micropores of the zeolite are active for DHA, confirming the proposed reaction mechanism of bi-functional metal/ZSM-5 catalysts in the literature. Furthermore, for Fe-HZSM-5, we found that atomically dispersed iron is thermally most stable and result in no detectable coke formation (on the metal sites). This observation thus yields a valuable guideline for the preparation of DHA catalysts and can potentially help to resolve the primary issues of state-of-the-art Mo/HZSM-5 catalysts: thermal stability and coking resistance.

As a second target, the micro- and meso-porosity of HZSM-5 was systematically changed by introducing different types and quantities of “porogens” (metal oxide or carbon black NPs) during zeolite hydrothermal crystallization. We found that coke formation within micropores is suppressed if a controlled degree of mesoporosity is introduced into the catalysts, while too much mesoporosity again enhances coke formation, presumable due to “excess space” and BAS for hydrocarbon formation. Moreover, with increasing mesoporosity the microporosity of the zeolite is decreased, which results in lower benzene selectivity (due to the absence of shape/size selectivity in the mesopores). Overall, one hence obtains optimal performance by balancing minimization of coke formation with high benzene selectivity by introducing a controlled (small) amount of mesoporosity into HZSM-5.

TABLE OF CONTENTS

LIST OF TABLES

LIST OF FIGURES

ACKNOWLEDGEMENTS

I am extremely grateful to many people who made valuable additions to my education over the years. I would like to thank my advisor Dr. Götz Veser for his guidance, insight, motivation and great assistance in completing my thesis. I really appreciate everything he has done for me.

I am very grateful to all of the graduate and undergraduate students that have helped to make my work a success. In particular, I want to thank Dr. Christopher S. Ewing for teaching me so much in the laboratory and Dr. Saurabh Bhavsar for experimental advice that contributed greatly to this work.

I want to thank my family for all their support and guidance through these years. Finally, thank you to my wife Yaran, who have encouraged and supported me all the time in these years.

Thank you all.

1.0 INTRODUCTION

1.1 METHANE DEHYDROAROMATIZATION (DHA)

Benzene, which is one of the most important organic intermediates in petrochemical industry, is mainly produced from crude oil nowadays. However, due to the constantly increasing oil price and the discovery of abundant shale gas, methane processing can be considered as an alternative pathway to produce this valuable aromatic product.

However, current methane processing via syngas is a highly energy-consuming process. A direct methane dehydroaromatization (DHA) to benzene product becomes a promising direction to work on.

$$6CH_4 \rightarrow C_6H_6 + 9H_2$$

While the reaction under oxidative environment results in a low selectivity toward benzene and abundant of CO and CO_2[1], the one under non-oxidative environment was demonstrated to give high benzene selectivity over bi-functional zeolite catalysts[2-3]. Under the latter condition, meanwhile, high purity hydrogen which is widely applied on fuel cells is also produced. This dissertation discusses only on the non-oxidative methane dehydroaromatization.

1.2 CATALYSTS FOR METHANE DEHYDROAROMATIZATION

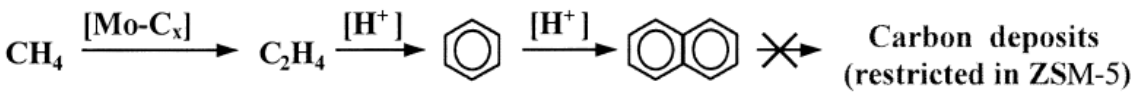

Figure 1. Mechanism of methane dehydroaromatization.

Among the reported bi-functional catalysts, molybdenum loaded H-form ZSM-5 (Mo/HZSM-5) has been generally accepted as the most active one in DHA reaction since it was first reported in 1993 by Wang et. al[2, 4].

ZSM-5, whose framework type is MFI (with micropore size ~0.55 nm), is an aluminosilicate zeolite belonging to the pentasil family of zeolites[5-6]. Its chemical formula is $M_{x/n}[(AlO_2)_x(SiO_2)_y]$ with high Si to Al ratio (SAR). Due to the charge difference between Si^{4+} and Al^{3+}, a cation (M^+) exists to balance the charge in ZSM-5 structure. This position of M^+ is the well-known cationic exchange site widely applied in industry applications[6]. Moreover, as the cation is a proton (H-form ZSM-5), this cationic exchange site becomes Bronsted scid site (BAS) and is one of the active sites of Mo/HZSM-5 for DHA reaction.

It was later proposed that formation of benzene over Mo/HZSM-5 catalyst comes from a synergistic effect between the metal site and the BAS of HZSM-5[7-8] (see figure 1). First, the active molybdenum species MoO_xC_y is responsible for activating methane to generate C-C coupling intermediates[9]. Subsequently, these C2 intermediates form olefinic carbenium, oligomerize and cyclize on neighboring BAS of HZSM-5 to produce aromatic products[10]. The high selectivity toward benzene instead of higher hydrocarbon products is attributed to the similarity in pore size of ZSM-5 with the dynamic molecular size of benzene[11].

However, the detailed mechanism for how the activated methane to C-C coupling intermediates is still only in hypothetic stage. Some researchers proposed that the activated methane molecule reacts with the BAS of HZSM-5 to become a molybdenum carbene-like intermediate (CH_2=MoO_3)[2, 12]. Via dimerization of carbene, ethylene is formed as the C-C coupling intermediate. Chen et al. proposed a free radical mechanism, where methane activation yields free CH_3**.** radicals via the concerted action of MoO_x and BAS[13]. CH_3**.** radicals then dimerize and dehydrogen to form ethylene. Despite the uncertainty in the exact nature of the intermediate formed from methane, C_2H_4 is widely accepted as the primary intermediate after methane activation[14-15]. The C_2H_4 intermediate was confirmed by comparing product distribution of H-ZSM-5 with/without Mo[16], Mo loaded on supports with/without BAS[17], and using CH_4 temperature programmed reaction (TPR) followed by H_2-TPR for Mo/HZSM-5 catalysts[18].

1.3 ISSUES OVER CURRENT CATALYSTS

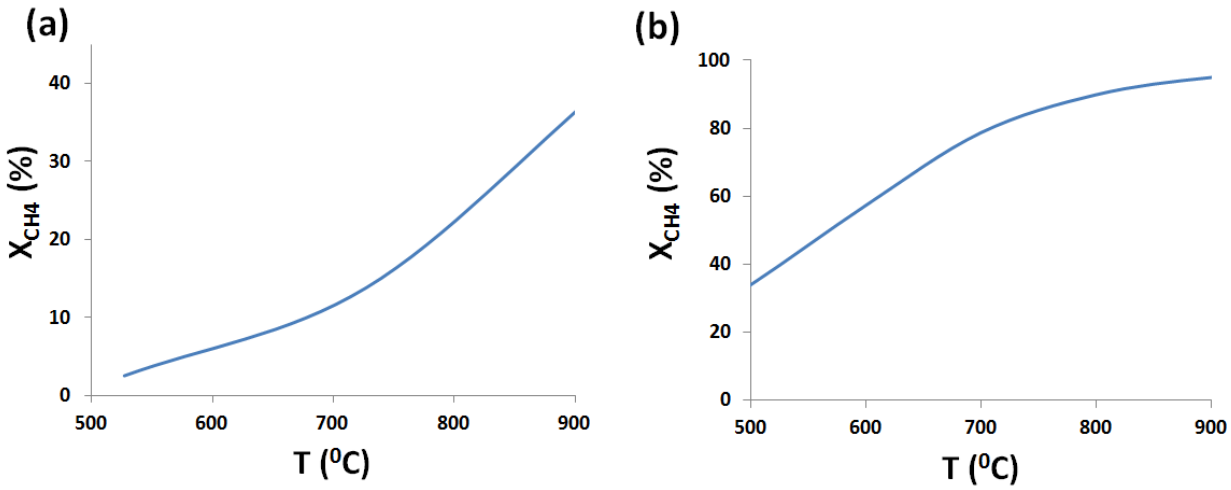

Figure 2. Equilibrium methane conversion to a) benzene and b) carbon[19].

Unfortunately, one of the most challenging issues for Mo/HZSM-5 catalysts is coking problem. Due to only small micropores in the ZSM-5 (MFI structure), poor transport of hydrocarbon products inside zeolite channels can easily result in secondary reaction with BAS to form coke. The formed coke covers active sites or block the zeolite channels to deactivate the catalysts[20-21].

In addition, due to the thermodynamic limitation of an endothermic reaction (Figure 2a), high methane conversion from DHA can only be achieved at very high temperature. For example, the most typically used temperature for DHA study is 700 ^{0}C. Nonetheless, equilibrium methane conversion to benzene at this temperature is only ~12%. Despite that higher temperature thermodynamically favors methane conversion in DHA, more severe coke deposition which results in decreased lifetime of catalysts and lowered benzene selectivity occurs (figure 2b). A proper and limited temperature range for DHA thus was suggested to be between 700- 800 ^{0}C[13].

1.4 RECENT PROGRESS ON DHA REACTION

1.4.1 Membrane Reactors

As discussed above, thermodynamic limitation limits the application of DHA reaction. A possible way to break thermodynamic limits of methane conversion is to apply membrane reactors, which remove hydrogen to pull the reaction forward. Via this technique, methane conversion over bi-functional zeolite catalysts was shown to exceed the thermodynamic limits as hydrogen removal rate is comparable to its production rate[22-25]. The possibility of achieving concomitantly the separation of high purity hydrogen within the same unit also makes the process commercially attractive.

However, stability of hydrogen-separation membrane is also a big obstacle. Typically, the reaction is carried out at 700-800 ^{0}C to achieve higher catalytic reactivity, which is a harsh condition for Pd-coated membranes[23]. Our collaborator NETL has shown that methane conversion gradually decreases due to the ability of membrane to separate hydrogen lost after

long time reaction runs. Moreover, hydrogen withdrawn favors the competitive formation of hydrogen-deficient species, which will further be reacted to form carbon deposition and exacerbate the existing coking problems[22-23]. Apparently, the biggest challenge of Mo/HZSM-5 catalysts in DHA results from the generated coke in zeolite, despite the thermodynamic equilibrium can be broken by process engineering.

1.4.2 Co-reactant in Feeding Methane

The idea of adding co-reactant is taken to react with deposited carbon in order to suppress coke formation. It has been reported that adding small amount of CO, CO_2, O_2 or H_2O into the methane feed indeed suppress part of coke formation in bi-functional Metal/HZSM-5 catalyst[8, 26-28]. As a result, the lifetime of catalysts was able to be significantly extended. However, some side effects will also occur if the concentrations of co-reactant exceed the optimal range (2-12%, depends on which co-reactant used), such as reduced activity in high CO, CO_2 concentration, loss of benzene selectivity with too much oxygen (formation of CO and CO_2), and dealumination of zeolite if water concentration exceeds the optimal value. Nonetheless, with a proper control of the amount of co-reactants, improvement of DHA stability over zeolite-based catalysts could be expected.

1.4.3 Zeolite Support

To date, different types of zeolite have been used for Mo-based catalysts for DHA, including ZSM-5[2, 29], MCM-49[30], MCM-22[31-32], SAPO-11[29], ITQ-13[33], zeolite X[29], etc. All the authors agree that two dimensional structure and pore size near to the dynamic diameter of benzene, ~6

Å, are fine supports of Mo-based catalysts for DHA[15, 29, 34]. For example, ZSM-5, ZSM-8, ZSM-11, MCM-22 were shown to be the most efficient in the studied reaction. Moreover, for MCM-22, which has large cavities (7.1 x 18.2 Å) in addition to small micropores, provides not only high benzene selectivity but also good coke-resistance[32].

1.4.3.1 Hierarchical-Zeolite-Based Catalysts for DHA

The coking problem can be suppressed via modifying porosity of a zeolite. It has been well known that secondary reactions of hydrocarbon products trapped in the inner channels causes coking formation on BAS[35-36]. Consequently, many efforts have been made to enhance the stability of zeolite-based catalyst by reducing the diffusion length (i.e. introduce mesoporosity) in zeolite channels[37-38] . However, the routes to generate mesoporosity for zeolites will greatly impact the cost for catalyst preparation and the catalytic performance in reactions.

Below is the review of well-known approaches for generation of mesopores (in zeolites) and their examples for the DHA reaction. Mesoporous materials such as MCM-41[39] were first explored and were used as a replacement for ZSM-5. However, their low crystallinity and no shape selectivity lower the catalytic reactivity and benzene selectivity in DHA[29, 40]. Alternatively, zeolite nanoparticles were reported[41-42]. However, very delicate conditions to prevent nanocrystals from growing into bulk crystals and low synthesis yield impede its further development on practical applications. Moreover, BAS seems to preferably stay on the external surface of ZSM-5 nanoparticles (NPs)[43]. As a result, shape selectivity of ZSM-5 is not taken and lower benzene selectivity is observed over nanoscale-ZSM-5 catalysts. Recently, a lot of attentions were put on creating mesopores in highly crystalline zeolite crystals, so dual merits of two different pore structures can be taken within a catalyst[44]. The efforts for preparation of such hierarchical zeolite to date can be generally categorized into two[45-46].

First, under certain zeolite conditions, post-synthetic demetallization is applicable to large-scale production with a great amount of mesopores[47-51]. However, a careful treatment needs to be conducted to avoid complete dissolution or loss of crystallinity. Moreover, demetallation alters the SAR in the zeolite and SAR is critical for catalytic performance of zeolite materials, as it determines the availability of BAS[52]. Thus, it is difficult to compare the catalytic performance of Mo loaded hierarchical ZSM-5 catalysts prepared through this approach.[53-57]

Another approach is based on the use of templates during zeolite crystallization. Through this pathway, more regular mesopores can be obtained. This approach can be further categorized depending on the type of template used, i.e. use of soft templates or hard templates. For soft templates, zeolites consisted of ultra-thin nanosheets were synthesized by designing a dual template which is quaternary ammoniums connected with hydrophobic alkyl tails[58]. Mesopores are generated by hydrophobic tails, whereas microporous zeolite frameworks are generated by multiple quaternary ammonium groups. Pore size from such soft template synthesis can be further tuned via surfactant tail length[58-59] or otherwise by adding swelling agents[60-61]. The biggest challenge of this approach, however, commonly comes from time-consuming synthesis procedure and the concerns about the high production cost. Moreover, Y. Wu et al.[62] have used hierarchical zeolites prepared through this way for DHA reaction. However, they reported that such hierarchical zeolite catalysts enable efficient catalytic reactivity only in the initial stage of reaction but their performance were no different to conventional zeolite catalysts in the long term run and the coke formation from hierarchical zeolites is even higher.

On the other hand, the direct generation of ordered mesoporosity was achieved by addition of a hard template with size of desired mesopore diameter during ZSM-5 crystallization. The hard templates could be carbon black, nanofibers or other nanostructured hard-materials[63-65].

All authors using this approach to create hierarchical structure of zeolite conclude that the mesoporous structure can strongly reduce coke formation within micropore channels and hence to extend the catalyst lifetime[66-67].

Despite that there is a controversy against the efficiency on using HZSM-5 with reduced micropore length (mesoporosity), such as lowering benzene selectivity and debate on extending catalyst-life, most studies agrees that extra mesoporosity can enhance the efficiency of product diffusion in zeolites[37, 54, 66-67] and thus less coke formation and better catalyst stability can be achieved.

1.4.4 Metal site

1.4.4.1 Mo species and their locations in Mo/zeolite catalysts

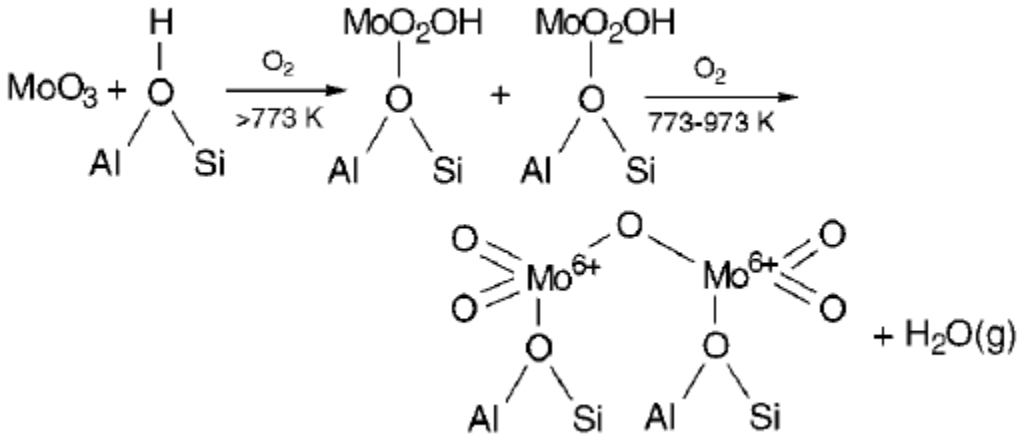

Figure 3. Evolution of MoO_3 within HZSM-5 micropores to form $Mo_2O_5^{2+}$ during calcination[68].

Mo/zeolite catalysts are commonly made by impregnation method, ion-exchange or chemical vapor deposition[2, 7, 69-72]. These approaches introduce Mo into zeolite after zeolite is synthesized. Due to the large size of metal precursor (i.e. $(NH_4)_6Mo_7O_{24}{\cdot}4H_2O$) which could not directly enter the micropore of zeolites[65], these approaches often result in Mo species resides on the external surface[36, 69, 73-74]. Moreover, because of no micropore shape selectivity, it was shown that these Mo species have less contribution to the formation of benzene or even are detrimental to both benzene selectivity and catalyst life[11, 43, 75-77]. The external Mo species commonly increases with increasing Mo concentration in the zeolite catalysts[68].

Since lattice mobility within MoO_3 becomes possible above its Tammann temperature (534K)[7, 43, 68, 78], however, some Mo species are demonstrated to be able to migrate into zeolite channels during calcination process. As these species migrate into micropores, they form an isolated molybdate species (MoO_5^{2+}) structure as shown in figure 3. An optimal temperature (500 ^{0}C) and time (~6 h) for calcination was shown to results in most Mo diffusing into micropores[68, 79]. During DHA reaction, these species undergoes an induction time (reduction and carburization) and form MoO_xC_y clusters which are believed to be the active species for this reaction[7, 52, 79-81]. However, after the catalysts become coked and is regenerated in oxidative environment to burn off carbon, active MoO_xC_y species also become back to inactive MoO_5^{2+} species. An activation time will be again needed to activate the catalyst in the next reaction cycle and this makes the reaction cycle inefficient.

1.4.4.2 Metal Site Tailoring

In many literatures, it has been shown that addition of promoters could have significant effect on the activity, selectivity, and coke resistance of Mo/HZSM-5 in DHA reaction. For example, Cu introduction to HZSM-5 zeolite by ion exchange followed by solid-phase synthesis of

Mo/Cu/HZSM-5 was studied for DHA[82]. It was found that the presence of copper increased the active Mo concentration in the catalyst. Moreover, copper introduction decrease the dealumination and coking rate and thus to increase the catalyst lifetime. As a result, the authors conclude that promotional effect of Cu on Mo/HZSM-5 results in a more active and stable catalyst. The addition of Co[83], W[84-85], Ru[86-87], Ni[88], and Fe[83, 89] to Mo/HZSM-5 catalysts was shown to also increase catalytic activity and selectivity. The use of Pt[90] as the modifying additive increased the stability of Mo/HZSM-5 catalyst due to lower carbonaceous species formed during the reaction.

In addition, other monometallic metal loaded HZSM-5 catalysts (metal: Zn[2, 91], W[3, 36, 92], Fe[3, 36, 93], V[3, 36], Cr[3, 36], or Re[26, 94]) are also documented for DHA reaction. However, except Re/HZSM-5, catalytic reactivity of other catalysts reported is not comparable to Mo/HZSM-5 catalysts. Rare study for Re/HZSM-5 was further reported probably due to high metal price of Re.

However, there are inconsistencies in the reports of promotional effect of second metal or other monometallic metal loaded HZSM-5 catalysts. For example, some reported that Fe as the dopant for Mo/HZSM-5 enhances the catalytic activity but others did not[83, 89, 95]. This could be attributed to different methods and procedures used for catalyst preparation. For example, Fe/HZSM-5 reported by Lunsford[3, 36] was prepared by different approaches and different pretreatments, including solid ion-exchange method, impregnation method, and with or without CO pretreatment before reaction. However, these catalysts prepared behave very differently from each other. The Fe/HZSM-5 prepared by solid ion-exchange shows barely reactivity while another catalyst prepared by impregnation method results in ~4% methane conversion. Both catalysts pretreated in CO shows much improved catalytic reactivity. These differences were attributed to different catalyst structure results from different preparation methods and

pretreatment conditions. Apparently, many reported catalysts were very different and the reaction conditions used were not identical in the literature. The catalytic results thus are not suitable to directly compare even though the catalysts have identical chemical compositions. A metal site study for DHA will require a systematic investigation.

1.4.5 Catalyst Regeneration

Whatever efforts have been made so far, coking issue still exists in DHA over zeolite-based catalysts. Thus, regeneration process to burn off deposited carbon is required, especially as DHA is operated at a high-coking tendency environment (i.e. Mo/HZSM-5 catalysts usually could not survive over 10 hr reaction at the typical reaction condition[13]). However, major concerns with regard to regeneration is the induction time of bi-functional zeolite catalysts and the regenerability[36, 74, 96]. Based on this, the gas content and regeneration processes were studied to maintain the regenerability and the efficiency of catalysts[97]. Oxygen is the one which can completely remove coke formed in the zeolite-based (Mo) catalysts and can be operated at relatively lower temperature (~500 ^{0}C). However, the regenerated catalysts are at the inactive phase (as discussed above) and require an activation time to become active Mo species[7,40,68-70]. Hydrogen was also reported to remove coke and restore the zeolite-based (Mo) catalyst before the catalyst becomes highly coked. No recurrence of the activation period was needed[7, 96]. However, hydrogen could not remove carbon in a highly coked catalysts and lower catalytic reactivity was observed in the next reaction cycle. As a result, a periodic mode by switching feeding gas between methane and hydrogen was studied[98]. However, the switching cycle has to be as short as 5-10 mins. Thus, a choice between a completely regenerated catalyst in inactive phase and a partly regenerated catalyst in active phase has to be made for DHA regeneration process.

2.0 OBJECTIVES

Mo/HZSM-5 catalyst has made non-oxidative methane dehydroaromatization (DHA) a potentially alternative pathway to produce benzene. However, as discussed in section 1.3.4.1, the catalyst deactivation via “coking” combined with “the lengthy reactivation of regenerated catalyst” poses a significant hurdle for economic viability of the process. The former issue results from the large network of micropores in ZSM-5 while the latter issue results from the MoO_xC_y as the active species.

The objective of this research is to develop a new bi-functional HZSM-5-based (metal) catalyst that is highly stable while maintaining the high benzene yield from DHA. Towards this goal, we aimed to investigate systematically how the catalytic performance is affected by changes in i) metal sites and ii) porosity of HZSM-5.

In order to systematically investigate how the catalytic performance is affected by metal sites, different metal sites have to be introduced into zeolites so correlation between metal sites and the correspondent reactivity can be built. There are several conventional routes to introduce metal species into zeolites, including impregnation, ion-exchange, and isomorphous substitution. These approaches could result in metal species at the framework and at the cationic exchange site (extra-framework), nanoclusters within micropores, and nanoparticles on the external surface of zeolites. However, these species are often inhomogeneously distributed. A new approach has to be developed to introduce well-dispersed NPs into zeolites so the effect of NPs alone can be

studied. In chapter 3, we aimed to use a bottom-up synthetic approach to achieve this goal. The developed synthesis approach then can be combined with other conventional approaches (described above) to study the effects of metal sites on catalytic performance.

Due to the lengthy reactivation issue of Mo species, which results from the reduced state of Mo (MoO_xC_y) as the active site, a metal which is active in high oxidation state is desired. In the literature, zinc was claimed to be this kind of metal, but no experimental results were reported for demonstration. In chapter 4, we aimed to systematically study different zinc sites in HZSM-5. The prepared zinc sites then can be correlated with the correspondent catalytic reactivity to investigate the active and stable zinc sites. Recently, atomically dispersed iron was reported to be very active for methane activation and result in no coke formation. However, such iron site is very difficult to synthesize over silica support as they reported. To easily prepare such iron site as well as take advantage of shape selectivity of ZSM-5, in chapter 5, we aimed to conduct a research for atomically dispersed Fe loaded on HZSM-5 and use it for DHA. To demonstrate the superior catalytic properties of atomically dispersed iron, we further aimed to prepare different iron sites for comparison.

In addition, hierarchical zeolites (i.e. zeolite with mesoporosity) have been shown to effectively suppress coke formation and thus extend the catalyst lifetime. Recently, however, some literature reported oppositely. However, rare work in the literature studied the effect of hierarchical zeolite in DHA systematically. Usually, the catalytic performance was compared between one conventional Mo/HZSM-5 with one Mo/hierarchical HZSM-5 and then a conclusion was made. The trend of changing porosity on DHA may be neglected. As a result, there is an apparent controversy for mesoporisity in suppression coke formation and extending lifetime of catalysts. In chapter 6, we target to systematically create hierarchical ZSM-5 structure and study the effect of mesoporosity on catalytic performance of Mo/HZSM-5 catalysts.

3.0 CONTROLLED EMBEDDING OF METAL OXIDE NANOPARTICLES IN ZSM-5 ZEOLITES THROUGH PRE-ENCAPSULATION AND TIMED RELEASE

Zeolites are among the most important heterogeneous catalysts in the chemical industry due to their desirable material properties, including high thermal stability, intrinsic acidity, and their unique shape selectivity.[99-100]. However, the small pore size of zeolites in the micropore regime (< 2nm), which is the basis of their desirable shape selectivity, also results in poor reactant and product transport within zeolite crystals.[37] This can lead to undesirable sequential reactions and—specifically for hydrocarbon conversions, which constitute a key application of zeolites in industry—can result in coke formation and subsequently deactivation of the catalyst.[38] This effect can be mitigated through the formation of additional pores with larger pore sizes in zeolite crystallites, i.e. through formation of hierarchical pore networks.[37, 44] To-date, the efforts for preparation of such a hierarchical zeolite fall broadly into two categories[45, 101]. First, post-synthetic de-metallization which is applicable to large-scale production can create a large amount of mesopores[49, 102-103]. This has already recently found application in de-aluminated zeolites for cumene synthesis in the Kellogg-Dow process.[104] The second approach is based on the use of templates during zeolite crystallization and can be further categorized depending on the type of template used, i.e. use of soft templates (such as co-surfactants or dual-templating surfactant[105-107]) or hard templates (such as carbon black or nanofibers[63-65]). The templating strategies generally result in more ordered mesopores, but require the use of sacrificial chemicals. Overall,

despite the success in creating mesoporosity within zeolites from these methods, they are either zeolite-type sensitive[53] or require sacrificial chemicals and/or expensive synthesis procedures.[106-107]

In parallel, much efforts has also been focused on introducing guest metals into zeolites in order to further tailor their reactivity for desired functionalities. Towards this goal, impregnation and ion exchange are the two most commonly used techniques with chemical vapor deposition emerging more recently as an alternate approach.[108] However, none of these "top-down" methods can entirely avoid the (undesirable) deposition or formation of some metal nanoparticles on the external surface of the catalyst particle, resulting in uneven dispersion of the metal and typically in undesired, unselective reactions.[109]

Recently, an alternative, bottom-up approach has been proposed, based on inducing in-situ crystallization of zeolites using a zeolite precursor with embedded guest species (such as metal ions or nanoparticles).[110-113]. This early work furthermore suggested that the metal species used in the ZSM-5 crystallization are well dispersed in the final product and that some mesoporosity is simultaneously created in this synthesis strategy.[110, 112]. Although the mesoporosity largely seemed to result from inter-crystallite porosity and showed low mesopore volume, a one-pot synthesis to achieve both well-dispersed guest metals and zeolites with mesoporosity is remarkable and seems worth further investigation. Furthermorer, the size of metal NPs which are embedded in this novel in-situ encapsulation approach has to-date not been controlled (i.e. the size of introduced NPs reported to-date depends on the choice of zeolite type or zeolite precursors[110, 112-113]), and no systematic study of the effect of introduced metal nanoparticles on the zeolite matrix and its mesoporosity has been reported to-date.

Building on this previous work, we describe in the present contribution a straightforward and flexible synthesis strategy to embed uniform metal oxide NPs in ZSM-5 and demonstrate the approach with zinc oxide, iron oxide, and nickel oxide nanoparticles. The approach consists of three successive steps: Starting with the synthesis of size-controlled metal oxide NPs, these NPs are first encapsulated in silica, and then the amorphous silica is converted to ZSM-5. This synthesis approach allows for a straightforward size control of the embedded NPs (using the vast and growing literature on synthesis of size-controlled metal and metal oxide NPs) and results in an excellent dispersion of the NPs in the host ZSM-5. Furthermore, this systematic synthesis approach reveals a direct correlation between the embedded metal oxide nanoparticles and the morphology and mesoporosity of the final composite composite (ZnO@ZSM-5).

3.1 EXPERIMENTAL

3.1.1 Material synthesis

ZnO@ZSM-5. ZnO NPs were prepared via a sol-gel process adapted from previous reports.[114-116] Typically, $Zn(OAc)_2 \cdot 2H_2O$ (1.48 g) in methanol (62.5 ml) was preheated to 60^0C under reflux. Then, NaOH (0.52 g) dissolved in methanol (32.5 ml) was added to initiate hydrolysis and condensation of ZnO. The mixture was stirred isothermally for 20 hrs. After the reaction, the supernatant was removed by centrifugation, the ZnO NPs were re-suspended in ethanol to wash away unreacted precursors and impurities, and the washing process was repeated three times.

Next, ZnO was encapsulated in amorphous silica via a modified Stöber synthesis. First, a specific weight loading of as-synthesized ZnO was re-dispersed in 200 ml of ethanol under

ultrasound. 9.5 ml of tetraethoxysilane (TEOS), 4 ml DI water was added, and the mixture sonicated for 20 mins. Next, 15.25 ml ammonia (28 wt%) dissolved in 32.5 mL of ethanol was added slowly to the solution under continuous stirring and aged for 3 hrs at 55 ^{0}C. The product solution was then centrifuged and re-dispersed in ethanol three times. The purified particles were dried and calcined at 500 ^{0}C for 2 hrs. Pure silica NP as a reference silica source wea synthesized using the same condition as above, omitting the ZnO NPs.

The ZnO@SiO_2 composites were converted to the ZnO@ZSM-5 via a hydrothermal treatment. Typically, ZnO@SiO_2 was added to a mixture of 0.02 g NaOH, 2.05 g tetrapropylammonium hydroxide (TPAOH, 20 wt %), 0.02 g $NaAlO_2$ and 2.57 g deionized (DI) water to get a molar ratio of Al_2O_3:180SiO_2:36TPAOH:5Na_2O:4280H_2O:xZnO. The mixture was stirred for 2 h and then transferred to a Teflon-lined autoclave and heated to 180 °C for 48 h. After cooling down to room temperature, the product was recovered by centrifuging, washed with deionized water, and dried at 100 °C overnight. Pure ZSM-5 was synthesized as reference material via the same procedure, replacing ZnO@silica with pure (i.e. ZnO-free) silica NPs. It is noteworthy that consistency in the nominal ZnO weight loading with the actual measured weight loadings throughout the synthesis steps suggests that the ZnO NPs remain intact and Zn dissolution from the NPs does not play a significant role in this synthesis.

MeO@ZSM-5 (MeO= Fe_2O_3, NiO). Following the same bottom-up synthesis strategy, MeO@silica was utilized as the silica source for MeO@ZSM-5 preparation. MeO@silica material was directly synthesized in a reverse-microemulsion mediated sol-gel process,[117] i.e. without first synthesizing metal oxide NPs separately. A mixture of Brij58 (>99%, Sigma-Aldrich)(20 g for Fe_2O_3@silica and 10g for NiO@silica) and 60 mL cyclohexane was heated to 50 ^{0}C in oil bath under stirring. Then, the iron nitrate or nickel nitrate aqueous solution and

finally the ammonium hydroxide solution were added dropwise. Finally, 5g tetraethoxysilane was added dropwise to the microemulsion. Hydrolysis and condensation of the silica precursors were allowed to proceed for 2 hours at 50 °C. MeO@SiO_2 was precipitated by adding 2-propanol, and washed three times by centrifugation and redispersion. The product was dried at room temperature and calcined at 500 ^{0}C to remove residual surfactant. The conversion of MeO@silica to MeO@ZSM-5 was then conducted at the same hydrothermal conditions described above for ZnO@ZSM-5 preparation.

ZnO/ZSM-5. Zn/ZSM5 was prepared by incipient wetness impregnation using a $Zn(NO_3)_2$ solution. This impregnated Zn/ZSM5 sample was dried under vacuum at 373 K for 12 h and treated in flowing dry air at 773 K for 5hrs.

3.1.2 Characterizations

X-ray diffraction (XRD) X-ray diffraction (XRD) measurements were performed with a high-resolution powder X-ray diffractometer (Bruker D8 Discover) using monochromatic Cu radiation at the wavelength of 1.54 Å using a beam voltage of 40 kV at a current of 40 mA. The diffraction patterns were recorded with a step of 0.02^0 (2θ) at 0.5 sec/step. The particle size of ZnO was estimated from this data via the standard Debye-Scherrer formula. SEM (JEOL JSM-6510LV field emission scanning electron microscope) was used to determine material morphology at beam voltage of 20 kV. A thin palladium film was sputter-coated on the sample before measurement. The actual compositions were determined via Energy Disperse X-ray spectroscopy (EDX) on the SEM, with a collection time of 120-180 s. The materials nanostructure was determined by both TEM (JEOL-2000FX electron microscope) and high-resolution TEM (HRTEM, JEOL-2100) after dispersing the samples on a copper type-B support grid (Ted Pella

Inc.). Surface area and mesoporosity are determined via nitrogen sorption in a Micromeritics ASAP 2020. Samples were degassed for 24 hours at 300 °C under high vacuum prior to each analysis. Both nitrogen adsorption/desorption measurements were performed at liquid nitrogen temperature (77 K). A typical test involved a 6-point Brunauer- Emmett-Teller (BET) analysis for total surface area measurement in the relative pressure range $0.1<P/P0<0.35$. Mesopore size and mesopore volume determination were calculated by the Barret-Joyner-Halenda (BJH) method. All reported pore properties were acquired by analyzing the adsorption isotherm data. Due to a well-known strong artificial peak at pore size ~2nm for ZSM-5 materials[118-119], all 2 nm peaks in the mesopore size distribution were removed by subtraction of the scaled 2 nm peak in the pure ZSM-5 samples to eliminate this artifact. A real mesopore generated through the embedding of oxide NPs in the hydrothermal synthesis thus can be reliably evaluated. Finally, micropore analysis was conducted for a 8wt% ZnO@ZSM-5 sample via Argon adsorption/desorption at 77 K using a Micromeritics 3Flex system. Micropore pore size distribution was calculated by the Non Local Density Functional Theory (NLDFT) method. It is noted that NLDFT is an integral equation which is solved to determine density of adsorbed molecules as a function of distance from adsorbent wall. The NLDFT method is modified from DFT model which omits short-ranged correlations. Thus, NLDFT accounts for the oscillations of the density profile near pore walls and was demonstrated to give a more precise analysis of micropore size distribution.[120-121]

3.1.3 Thermal stability test

Thermal stability tests were carried out at 700 ^{0}C in air for 1h for 8wt% ZnO@ZSM-5 composites. TEM images and XRD were recorded before and after the calcination treatment.

3.2 RESULTS AND DISCUSSION

ZnO NPs. Following the above outlined three-step synthesis strategy, we first synthesized ZnO NPs with the desired particle size (typically around ~6 nm in the standard synthesis) using a sol-gel process. XRD of the resulting powder (Figure 4a) indicates that ZnO was successfully synthesized, and the size of ZnO NP is calculated from the peak width (FWHM) using the Scherrer equation to be around 6 nm. Particle size distributions from TEM measurements (Figure 4b) show a narrow size distribution with an average particle size that is consistent with the size suggested by XRD.

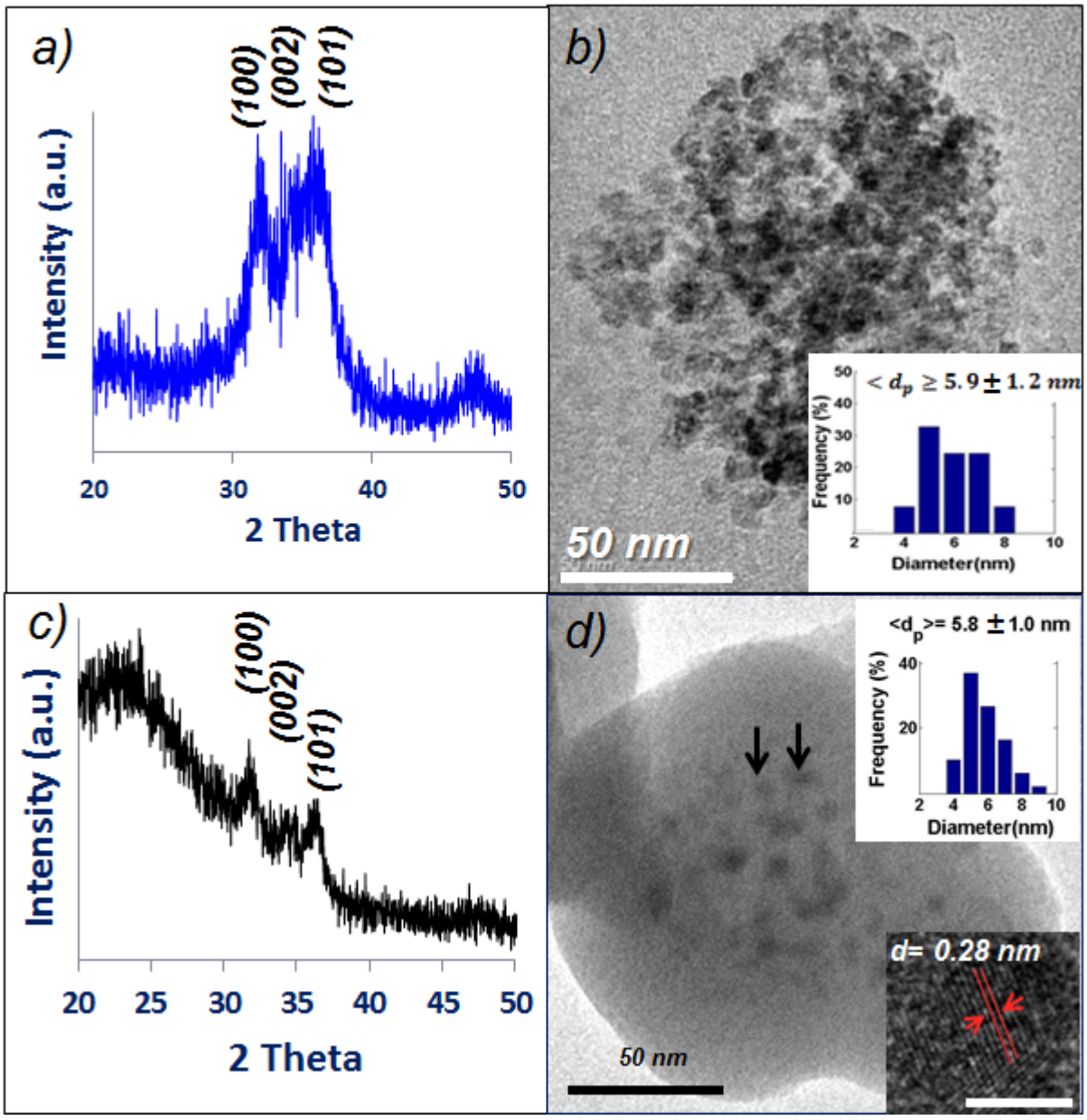

Figure 4. XRD pattern of a) ZnO NPs and c) 8 wt% ZnO@silica along with their respective TEM images (b) ZnO NPs and d) 8 wt% ZnO@silica). The inset in the TEM image shows the particle size distribution with >100 particles counted, and the second inset in (d) shows the HRTEM image of a embedded ZnO NP.

ZnO@silica. Amorphous silica was utilized as a host matrix to confine ZnO NPs via in-situ encapsulation by a Stöber synthesis[122]. XRD (Figure 4c) of ZnO@silica with 8wt% ZnO (from EDX results) shows a broad, diffuse diffraction peak at about 23 ^{0} assigned to amorphous

silica. Diffraction peaks from ZnO are also observed and remained broad, in agreement with the small size of the embedded ZnO NPs. TEM (Figure 4d) shows that the particle size of the ZnO NPs (~6 nm) is not affected by the encapsulation step and that the ZnO NP are well dispersed in silica (no particles were found on the external surface of the silica). HRTEM further indicates that the d-spacing value of the embedded particles agrees well with the lattice spacing of the (100) plane of ZnO (d_{100}, see bottom right inset in fig. 4d). Thus, ZnO NPs were successfully confined within the silica without obvious changes to the NPs.

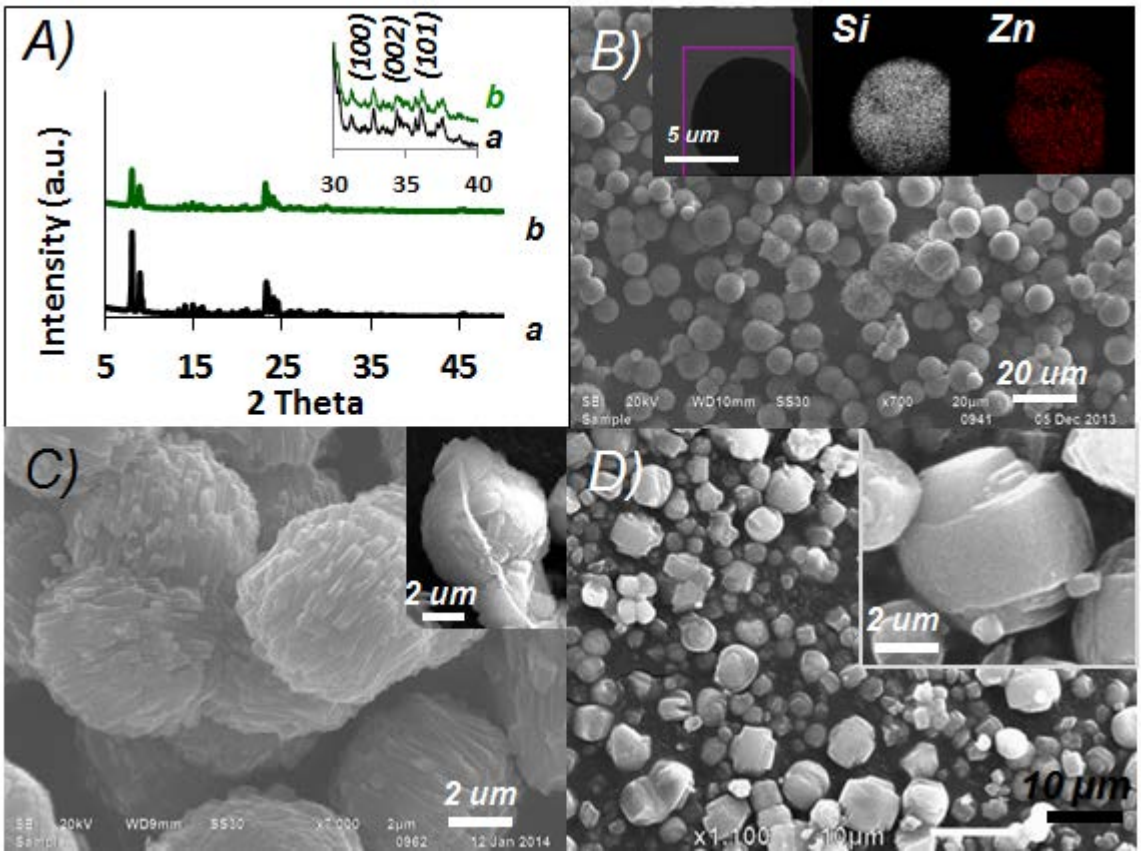

Figure 5. A) XRD patterns of a) ZSM-5 synthesized from ZnO-free silica, b) ZnO@ZSM-5 (8wt% ZnO). Inset: zoom in for XRD pattern between 2 theta 30 to 40, and ZnO reflection peaks in this range are 31.5^0 (100), ~34.5^0 (002), and ~ 36^0 (101); B) SEM image of ZnO@ZSM-5 at low magnification. The inset shows STEM image and the corresponding EDX mapping of a microsphere.; C) SEM image of ZnO@ZSM-5 at high magnification. Inset: a broken microsphere with numerous nanorods inside; D) SEM image of ZSM-5 synthesized from ZnO-free silica, and the inset shows SEM image of a representative crystal at a high magnification.

ZnO@ZSM-5. The synthesized ZnO@silica was used as the silica source for the subsequent zeolite growth in a hydrothermal environment. Following this step, XRD of the resulting ZnO@ZSM-5 (8wt% ZnO; Figure 5A) shows a diffraction pattern typical for MFI structures, confirming that the obtained zeolite structure is ZSM-5 and that the zeolite shows good crystallinity. However, no distinct diffraction peaks from ZnO were observed (see inset in

Figure 5A; ZnO diffraction peaks are at ~31.5^0 (100), ~34.5^0 (002) and ~ 36^0 (101)) likely due to a combination of the small particle size of ZnO and the shielding effect of the zeolite matrix. This also suggests that no larger ZnO particles were formed in the course of the hydrothermal conversion of the silica matrix to ZSM-5.

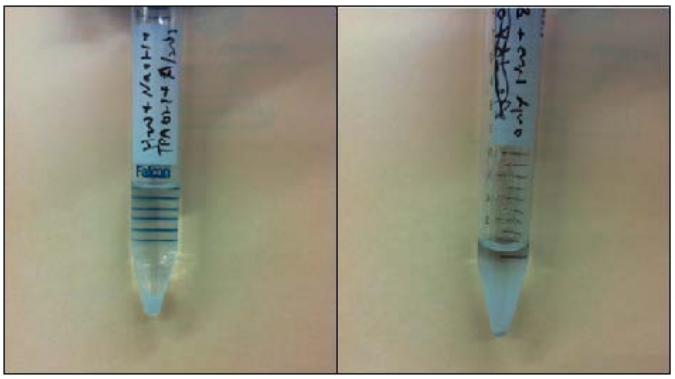

Figure 6. Aggregation of ZnO was confirmed by leaving ZnO NPs solely in the same hydrothermal solution as the one for ZnO@ZSM-5 synthesis without silica source. ZnO NPs in hydrothermal synthesis solution (left), and in water (right) for comparison. Photos were taken after the mixture stayed 10 minutes at room temperature.

The ZnO@ZSM-5 nanocomposite particles exhibit a spherical shape with rather uniform size (5~10 um) throughout the sample as observed in SEM (Figure 5B). Remarkably, however, the surface of each micron-size sphere is composed of well-defined, densely packed nanorods (Figure 5C). SEM images of the cross section of broken particles (after crushing the sample, see inset of Figure 5C) further indicates that the microspheres are composed of stacked nanorods throughout the particle. In contrast, a hydrothermal synthesis with ZnO-free silica as the silica source was conducted at identical hydrothermal conditions. In this case, only typically intergrown “coffin-shape” crystals were obtained (Figure 5D). Clearly, the aggregated nanorod

structure of ZnO@ZSM-5 is distinctly different from the morphology of pure ZSM-5 and a result of the presence of the ZnO NPs which cause the ZSM-5 crystals to break up into stacks of small nanorods. This suggests a strong impact of the ZnO NPs on ZSM-5 crystallization (which will be further discussed in the following sections). STEM images of a microsphere sample combined with EDX elemental mappings (Figure 5B, inset) shows that Zn is homogeneously dispersed in the composite. Small ZnO NPs are well-known to aggregate quickly in basic/aqueous solutions (Figure 6),[123] which are typically used for zeolite growth. However, our observations suggest that ZnO NPs did not aggregate during the conversion of ZnO@silica to ZnO@ZSM-5.

TEM was conducted for further characterization of this nanocomposite. A representative area of a crushed ZnO@ZSM-5 samples is shown in Figure 7a. A fragment of a rod-like object is shown with many small NPs dispersed throughout this region. The Fourier transform (FFT) of this image (Figure 7a, inset) supports the presence of both ZSM-5 and ZnO: The strong hexagonal spots in the center stem from the large single crystal of ZSM-5 while the outer spotty rings are consistent with the d-spacing of multiple embedded ZnO NPs. Furthermore, HRTEM lattice fringes of these small nanoparticles (Figure 7b) show a 0.28 nm d-spacing, in good agreement with the d_{100} spacing of ZnO. To confirm the location of these ZnO NPs inside the nanorod, i.e. their embedding into the zeolite matrix (albeit obviously not in the zeolitic micropores, due to the comparatively large size of the NPs), treatment in 5% hydrogen at 700 ^{0}C was used to remove ZnO NPs in the ZnO@ZSM-5 composite. At these conditions, ZnO is reduced to metallic Zn and the high vapor pressure of Zn results in rapid evaporative loss of Zn from the sample (thus also indicating facile access to the embedded NP surface for the reducing gas as well as efficient transport of the evaporating Zn out of the nanocomposite). The TEM image in Figure 7e reveals indeed a very holey (“swiss-cheese”) structure of the sample after this

treatment, i.e. a large number of pores were formed with diameters in the size range of the NPs, suggesting that most ZnO NPs were indeed embedded inside the zeolite nanorods. However, some ZnO NPs were also observed in between the primary nanorods, as shown in Figure 7c.

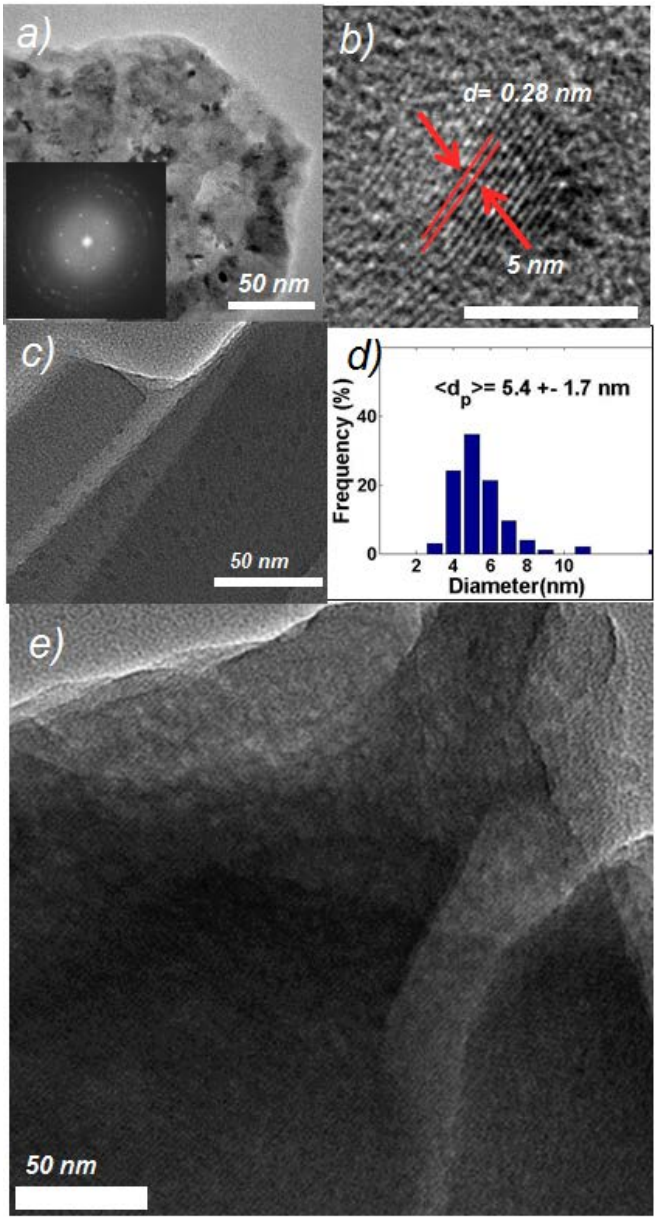

Figure 7. TEM image for 8 wt% ZnO@ZSM-5 composite. a) TEM images of a cracked nanorod, and the inset is FFT of image a); b) HRTEM image of a ZnO NP from a); c) TEM image for ZnO NPs located in between primary nanorods; d) ZnO NP size distribution in ZnO@ZSM-5 composites; e) A cracked sample of ZnO@ZSM-5 after ZnO was removed by a thermal treatment.

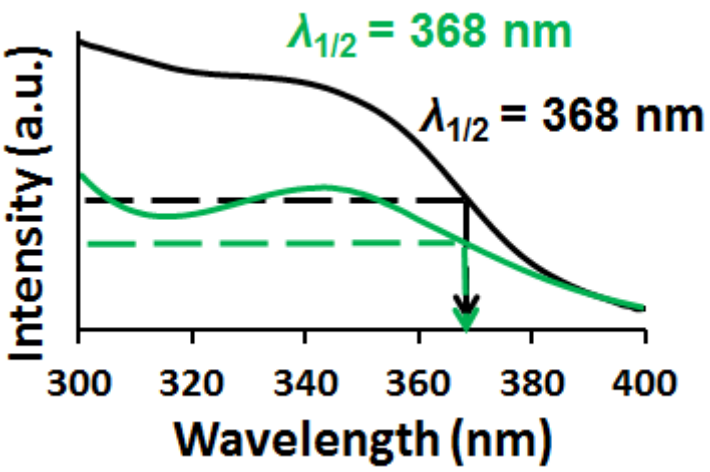

Figure 8. UV/vis spectrum for (8 wt% ZnO) ZnO@silica (black curve) and ZnO@ZSM-5(green curve). It should be noted that due to the different background absorption (i.e. silica and ZSM-5), the absorbance intensity are different. $\lambda_{1/2}$: the absorption at 50% of that of excitonic peak.

Particle size statistics of ZnO NPs (from TEM; see Figure 7d) suggests the size of ZnO NP is essentially unchanged by the transformation process from amorphous silica to zeolite (d~ 5.4±1.7 nm). This is further confirmed via UV/vis measurements. ZnO NPs are known to show quantum confinement effects for particle sizes <6 nm, and UV absorbance is thus commonly used to study the particle size of ZnO NPs.[123-125] Meulenkamp, who used $\lambda_{1/2}$ (i.e. the absorption at 50% of the characteristic excitonic peak) as ZnO NP size descriptor,[123] reported a $\lambda_{1/2}$ of ~365 nm for 6 nm ZnO NPs. Using this measure and comparing the UV absorbance spectrums of ZnO@silica before and after hydrothermal conversion (Figure 8), the two curves show virtually the same $\lambda_{1/2}$ (368 nm), again confirming that the ZnO NP sizes are unaffected by the conversion and remain ~ 6nm.

The Ar adsorption isotherm (Figure 4a) for the ZnO@ZSM-5 sample exhibits a sharp uptake at a low relative pressure (P/P_0), indicating the existence of microporosity, as expected for a zeolite. Moreover, a H4 type hysteresis loop starting from the relative pressure 0.45 to 0.85 is

observed, suggesting mesoporosity also exist in this nanocomposite. The calculated micropore size (Figure 4b) is centered at 0.55 nm, in agreement ith the micropore size of ZSM-5 (note that the small peak at ~1 nm is a well-known artifact in Ar isotherms for MFI zeolites, caused by a phase transition of Ar trapped in the zeolite[118, 126]). In addition, the mesopore size distribution indicates pores centered at ~3 nm with a small shoulder indicating another pore population with diameters ~7 nm (inset of Figure 9b).

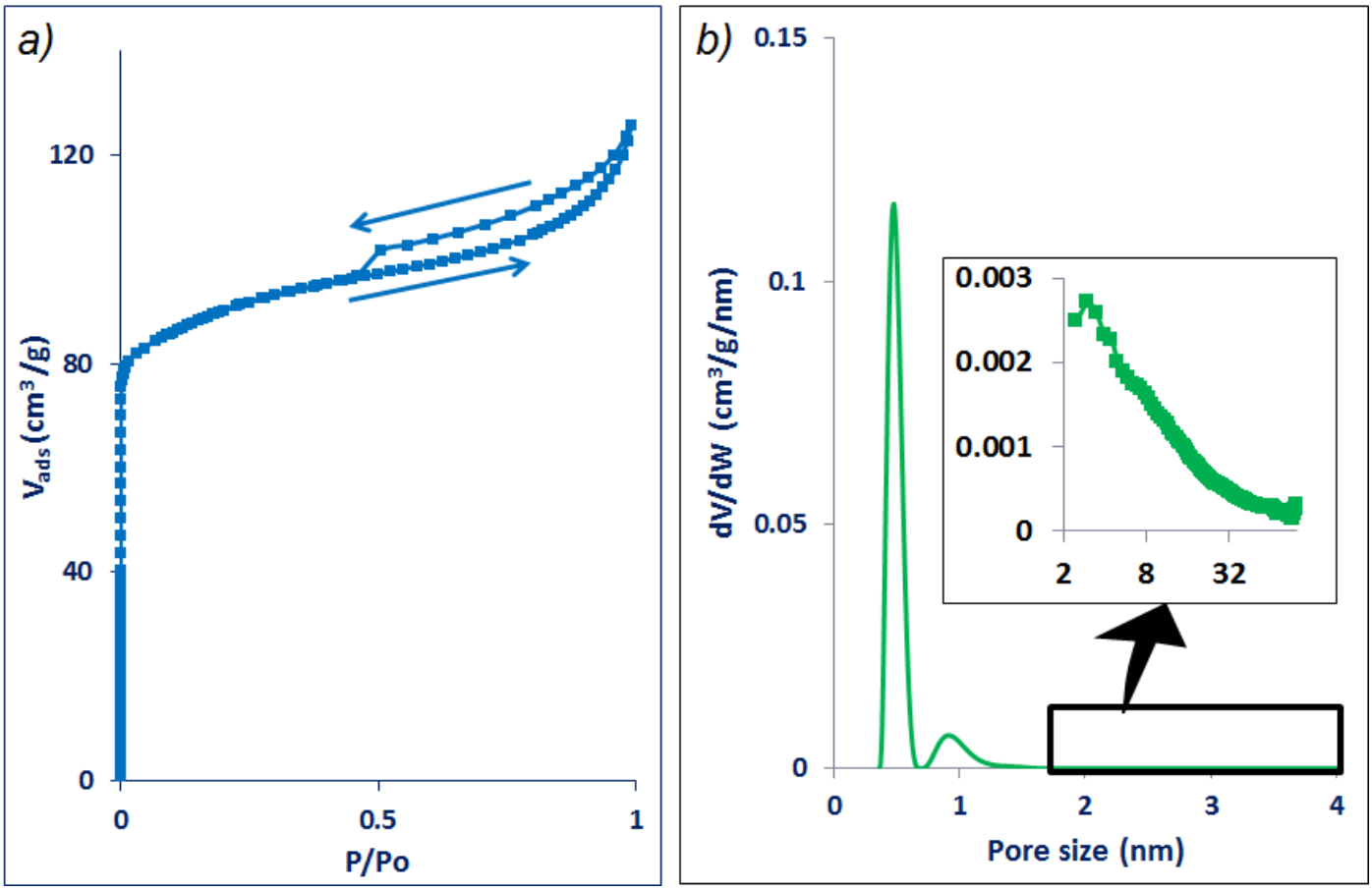

Figure 9. a) Ar adsorption/desorption isotherms for 8 wt% ZnO@ZSM-5. b) Micropore size distribution calculated from the adsorption isotherm via the NLDFT method. The inset shows the mesopore size distribution calculated from the adsorption isotherm by the BJH method**.**

3.2.1 Impact of Synthesis Parameters during Hydrothermal Treatment

3.2.1.1 Impact of hydrothermal reaction time

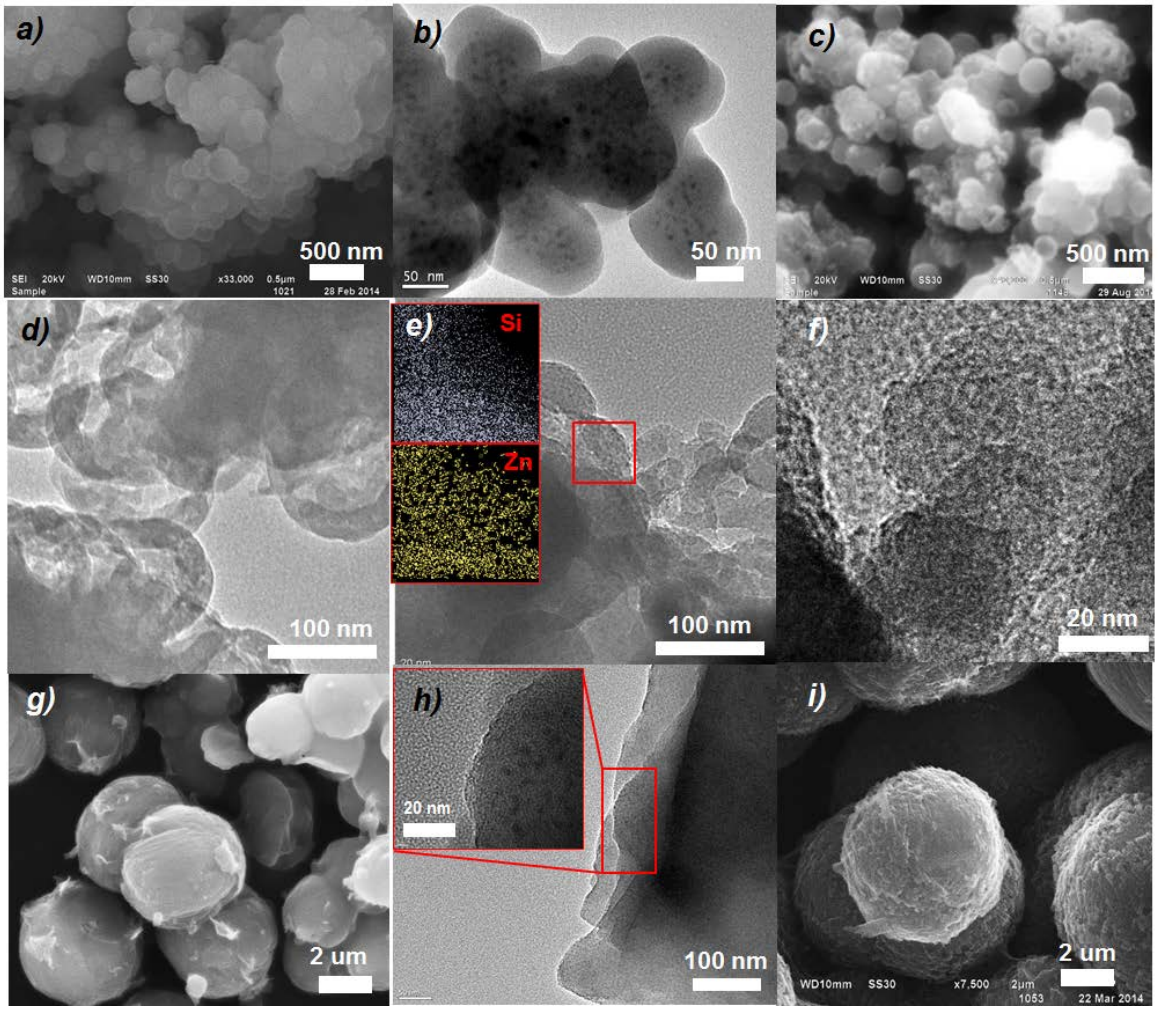

Figure 10. a) SEM and b) TEM of ZnO@silica composites; c) SEM and d~f) TEM of samples after 0.75h treated in hydrothermal conditions. The inset in e) is the EDX mapping for the red square area, while f) is the HRTEM image of this red square area with ~30 nm aggregates surrounded by ~6 nm ZnO NPs; g.h) SEM and TEM of microsphere-like particle after 6h hydrothermal treatment; i) SEM of microsphere-like particle after 48h treatment.

To elucidate the evolution of the formation of the ZnO@ZSM-5 microspheres, products were collected at different reaction time intervals. At beginning, ~6 nm ZnO NPs are well confined in ~ 100-300 nm silica particles (8 wt% ZnO), as indicated by SEM and TEM images in Figure 10a,b. After 45 min. hydrothermal treatment, most silica particles are etched in the base hydrothermal solution, resulting in hollow silica shell structures (Figure 10c,d). In the vicinity of these structures, TEM shows the presence of small particle aggregates (<50 nm; Figure 10e,f). The much smaller size of these aggregates compared to the silica precursor particles suggests that these are likely ZSM-5 nuclei (or aluminosilicate gel) which result from a reaction between dissolved silica and TPAOH. Importantly, the ZnO NPs which are released from ZnO@silica during the etching of the silica matrix are located on and in between these small aggregates - no ZnO aggregates were observed anywhere in the sample (Figure 10f).

When the hydrothermal time is prolonged to 6 h, the sample is entirely composed of spherical particles in the micron-size range (Figure 10g). Some rectangular sharp edges are observed on the sample surface, indicating the formation of crystal domains at this point. The corresponding TEM image (Figure 10h) confirms this transformation, with sharp edges of crystal domains visible. ZnO NPs are already observed to be encapsulated within these domains. Finally, after 48h of hydrothermal treatment, the microsphere size has grown uniformly to that of the larger spheres observed at 6h. At this point, all microspheres appear composed of densely packed ZSM-5 nanorods stacked uniformly throughout the microspheres (Figure 10i), in agreement with the detailed structure information of this sample after 48h hydrothermal treatment discussed further above (Figure 5 and 7).

3.2.1.2 Impact of number of embedded metal oxide nanoparticles

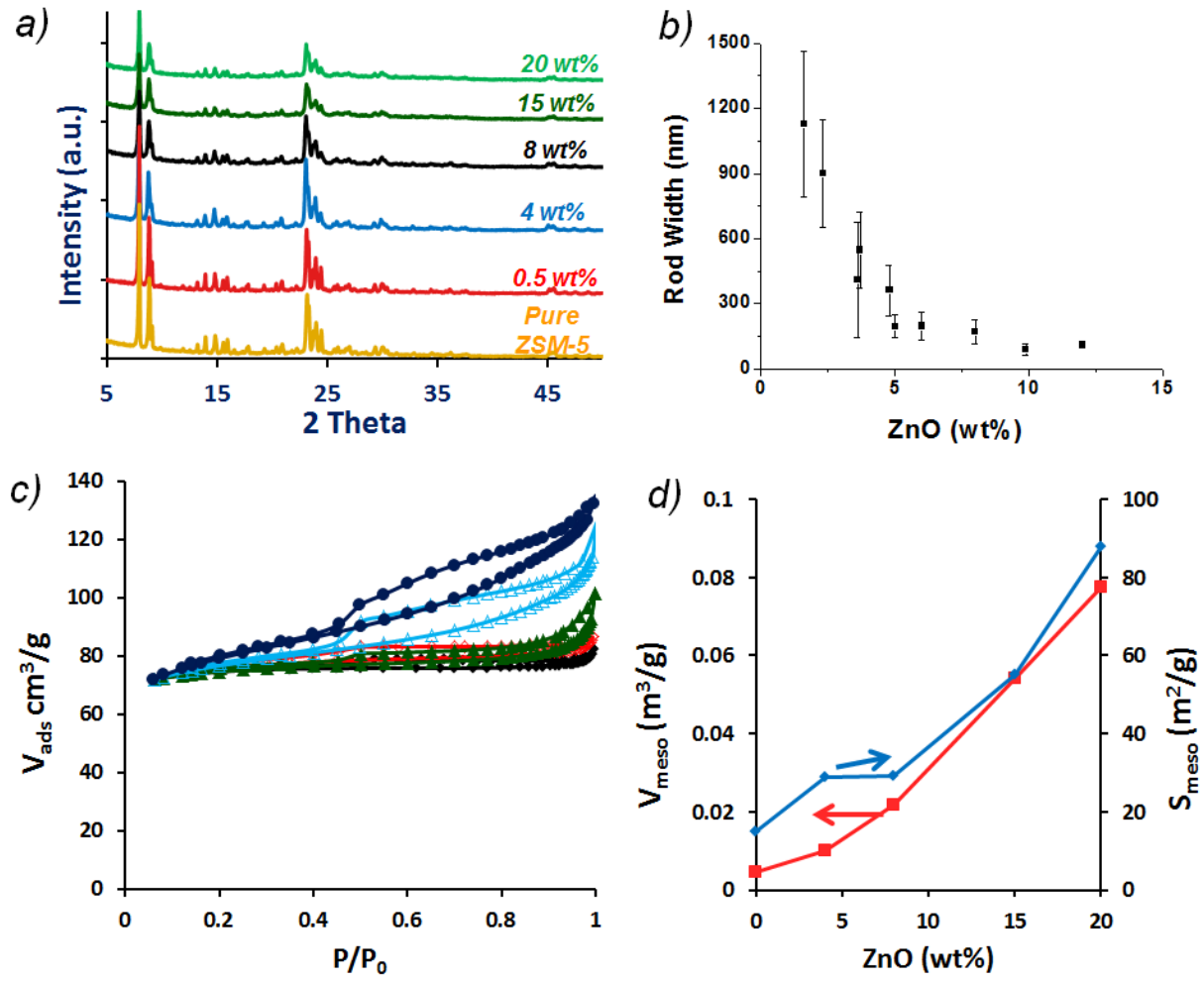

Figure 11. Impact of ZnO weight loading on the ZnO@ZSM-5 nanocomposite structure and porosity. a) XRD pattern, b) nanorod width, c) N_2 adsorption/desorption isotherms, and d) mesopore surface area and volume of ZnO@ZSM-5 versus ZnO weight loading. Weight loadings in the N_2 isotherms in (c) are: 0 wt% ZnO (solid diamonds), 4 wt% ZnO (empty diamonds), 8 wt% ZnO (solid triangles), 15 wt% ZnO (empty triangles), and 20 wt% ZnO (solid circles). Mesopore surface area and volume in (d) are calculated from adsorption isotherms by BJH method.

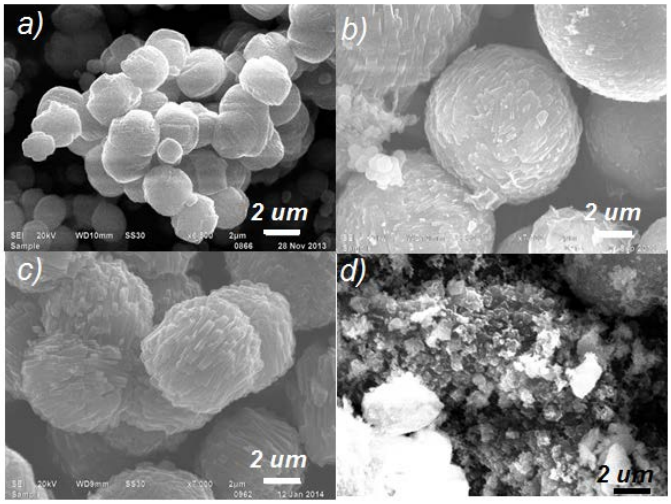

Figure 12. Morphological and textural transformation of ZnO@ZSM-5 with increasing weight loadings of ZnO: a) 0.5 wt%, b) 4 wt% c) 8 wt% d) 30 wt%.

Several parameters related to the embedded ZnO NPs in ZSM-5 can be expected to impact the properties of the ZnO@ZSM-5 nanocomposites and were hence investigated separately. Based on the above observations, one can expect that the number of embedded ZnO NPs should impact the ZSM-5 structure The ZnO NP loading in the ZnO@ZSM-5 nanocomposite can be adjusted in a very straightforward way by controlling the amount of ZnO NP used in the Stöber synthesis of the ZnO@SiO_2 precursor. As expected, XRD of the resulting samples (Figure 11a) indicates that the crystallinity of the formed ZSM-5 decreases with increasing NP numbers, suggesting again that the embedded NPs have a strong impact on the ZSM-5 crystallization behavior. This is further confirmed by a change in morphology of the ZnO@ZSM-5 nanocomposites with changing ZnO weight loading: ZnO@ZSM-5 samples with very low Zn loading (0.5wt%, figure 12a) exhibit only an “intergrown coffin” morphology, suggesting that a small amount of NPs barely affects the crystallization behavior of ZSM-5. As the amount of ZnO NPs is increased, the product gradually transforms to the aggregated-nanorod spherical morphology (Figure 12b,c).

Interestingly, we found that the width of the nanorods in these microspheres decreases monotonically with increasing ZnO NP amount (Figure 11b), suggesting that the NPs play a key role in the break-up of the zeolite crystallites into nanorod structures. It seems likely that with increasing NP content, the increasing number of NPs can no longer be accommodated within the zeolite crystals and instead align along the external surface of the rods (see Figure 7c), thus stabilizing the nanorods at increasingly small sizes.

Finally, a further increase in the NP loading results in the formation of irregular aggregates, with fewer and fewer well-defined microspheres observable (Figure 12d). Clearly, uniform microspheres consisting of aggregated ZSM-5 nanorods require a minimum amount of NPs for formation and stabilization while an excess of NPs strongly hinders the formation of larger ZSM-5 crystallites. This observation is consistent with the XRD observation that crystallinity decreases strongly with increasing NP loadings.

Significantly, the ZnO NP loading also has a strong impact on the mesoporosity of the ZnO@ZSM-5 nanocomposites. The N_2 adsorption isotherm becomes steeper with increasing NP loading, and the hysteresis loop at higher relative pressure (P/P_0) becomes more and more pronounced (Figure 11c). Both characteristics indicate that an increasing amount of embedded ZnO NPs results in increasing mesoporosity within the zeolite microspheres, as confirmed by an almost linear increase in mesopore volume and surface area with ZnO weight loading (Figure 11d).

3.2.1.3 Impact of ZnO NP size

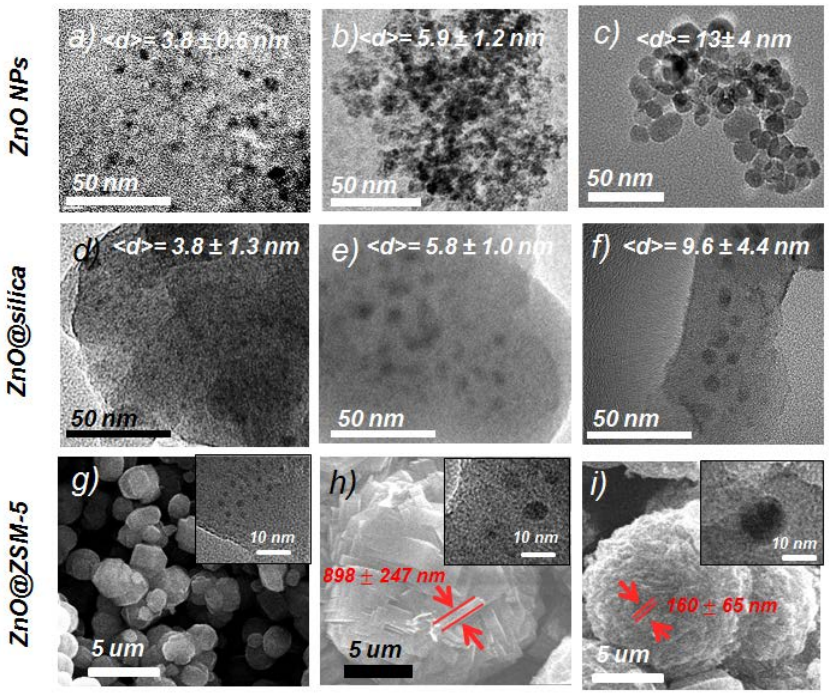

Figure 13. ZnO@ZSM-5 synthesized from different size of ZnO NPs. a), b) and c) are TEM images for ZnO NPs with size 3.8±0.6 nm, 5.9±1.2 nm and 13± 4 nm, respectively; d), e) and f) are TEM images for ZnO@silica synthesized from a), b) and c), respectively. The size of ZnO NP embedded in silica is 3.8±1.3 nm, 5.8±1.0 nm and 9.6±4.4 nm for d), e) and f), respectively; g), h) and i) are SEM images for ZnO@ZSM-5 synthesized with d), e) and f) as the silica source, respectively. The insets g), h) and i) show the TEM images of ZnO NPs which are embedded within ZnO@ZSM-5 microspheres, with ZnO NP size 3.8± 0.8 nm, 5.4± 1.7 nm, and 13.7± 6.3 nm, respectively. Ps. The size of bare ZnO NPs was tuned by changing the synthesis time length (2 hours for 3.8 nm ZnO) and precursor concentrations (x10 for 13 nm ZnO compared to the other two).

Beyond the number of embedded oxide nanoparticles, one can expect that NP size should have a significant impact on the structure of these nanocomposites. The bottom-up synthetic scheme again makes it possible to control the embedded NP size through straightforward modification of

the ZnO NP precursors (Figure 13). Again a strong dependence of the morphology of the nanocomposite particles on the embedded NPs is evident: ZnO@ZSM-5 synthesized from 3.8 nm ZnO NPs yields only intergrown coffin-shape crystals (Figure 13g), while composites from larger NP sizes show again the aggregated-nanorod morphology. Moreover, the average nanorod width of ZnO@ZSM-5 from larger (13 nm) ZnO NPs is significantly smaller than that from smaller (5.9nm) NPs (160 65 nm vs 898 247 nm, respectively, see Figure 13i and 13h). The reason for this size dependence is not as easily understood as the dependence on the number of nanoparticles. It seems reasonable that larger nanoparticles are less favorable for embedding into the nanorod structure itself, i.e. growth of the zeolite crystallite around the NP is increasingly hampered with increasing particle size, resulting in a larger fraction of NPs that are located at the nanorod surface instead. Hence, an increase in particle size should have a similar effect as an increase in NP number. However, it is challenging to get a sufficient number of NP counts to proof or disproof this hypothesis on a statistically sound basis, and the explanation hence remains speculative at this point. (It should be noted that in these tests, the *number* of embedded NPs was held constant by changing the weight loading to account for the different NP sizes).

3.2.1.4 Impact of silica precursor

The results discussed so far suggest an intricate interplay between the transformation of the silica matrix to zeolite and the embedded ZnO NPs. However, it is well known that the transformation reaction does not occur as *in-loco* liquid-solid reaction between silica and the aluminum precursor but via dissolution of silica followed by nucleation of the zeolite structure from the liquid-phase.[127] In order to further probe the importance of the core@shell structure of the precursor, experiments were conducted using a separated feed of ~6 nm ZnO NPs and ZnO-free silica NPs as source materials for the hydrothermal reaction with a target weight loading of 8

wt%. In contrast to the previous syntheses, the resulting materials from this synthesis showed widely disparate morphologies and spatially inhomogeneous composition (see Figure 14). SEM shows the formation of a wide range of different aluminosilicate aggregates with both coffin shape, aggregated nanorod structure, and entirely irregular shape (Figure 14a), in stark contrast to the highly homogeneous structures formed in the syntheses from the ZnO@Silica precursors. Similarly, the local ZnO concentration fluctuates widely within the sample. In particular, the ZnO concentration in the irregular aggregates is much higher than the nominal weight percent of ZnO in the product (Figure 14b). Similarly, the intergrown-coffin shape morphologies (Figure 14c) indicate ZSM-5 with no or very low ZnO NP loading, as discussed further above. With increasing overall ZnO concentration in the synthesis, the occurrence of the intergrown-coffin morphology is somewhat reduced while the frequency of irregular aggregates with very high zinc concentration increase dramatically (Figure 14d). Hence, a highly inhomogeneous distribution of ZnO NPs in the zeolite matrix results when ZnO and silica are added as separate feeds to the synthesis.

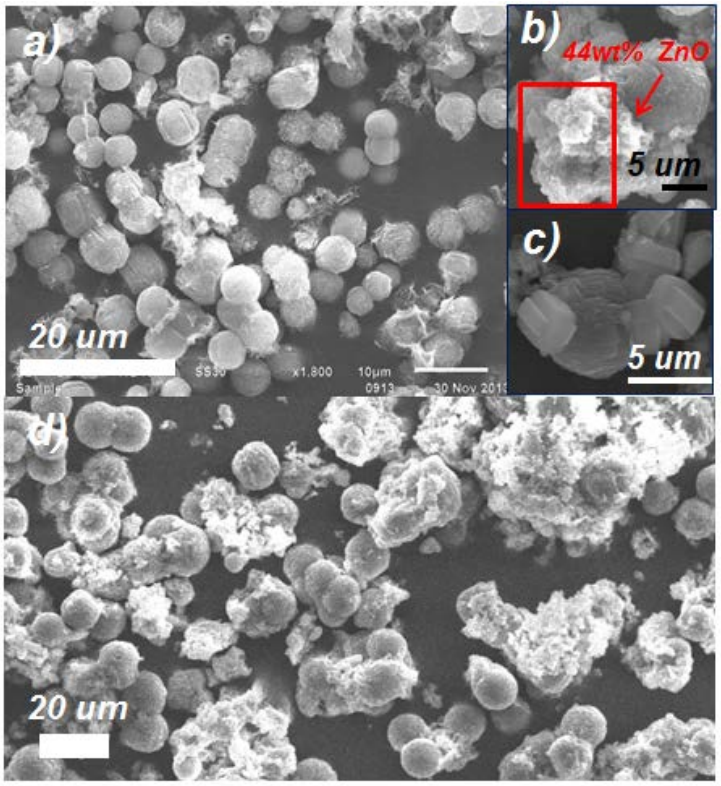

Figure 14. SEM images of ZnO@ZSM-5 synthesized by adding silica and ~6 nm ZnO NPs separately into hydrothermal solutions. (a) 8 wt% ZnO sample. b) and c) are higher magnifications of areas from a). EDX indicates 44 wt% ZnO for the area marked by the red box in (b), well in excess of the nominal 8 wt%. d) 20 wt% ZnO sample.

3.2.2 Proposed mechanism

Based on above observations, we propose a formation mechanism for this unique stacked-nanorod ZSM-5 structure obtained from the described bottom-up synthesis (Scheme 1). The synthesis builds onto the well-established synthetic capabilities for the production of size-controlled metal (oxide) nanoparticles, and their encapsulation into a silica matrix. When this ZnO@silica composite is heated in a hydrothermal solution (with well-defined composition, such as Al_2O_3: 180SiO_2: 36TPAOH: 5Na_2O: 4280H_2O: xZnO), the amorphous silica matrix

gradually dissolves, releasing both soluble silicate species (such as SiO_4^{-2}) and ZnO NPs (Figure 10c,d) (Scheme 1a). Nucleation of aluminosilicate occurs from a reaction of the dissolved silica with TPAOH and, as previously reported for similar hydrothermal conditions (temperature and molar ratio of the mixture), aggregation of the nuclei occurs quickly in parallel with formation of new nuclei, i.e. nucleation and aggregation take place at comparable rates.[38, 112] This timing is critical to assure that the released ZnO NPs are quickly captured and encapsulated by the aluminosilicate aggregates in order to avoid precipitation and/or aggregation of the ZnO NPs and hence inhomogeneous distribution of the NPs in the final zeolite structure (Scheme 1b). This is evidenced by TEM images taken at an intermediate stage of the formation of the ZnO@ZSM-5 structure shown in Figure 10e,f, where one can find ~6nm NPs distributed homogeneously between ~30 nm aluminosilicate aggregates. The fine balance between the time scales of dissolution of the silica matrix, nucleation, and aggregation of the aluminosilicate phase, and capture of the concurrently released ZnO NPs is hence critical to maintain a homogeneous ZnO NP distribution in the final ZnO@ZSM-5 nanocomposite. The “timed release” of the ZnO NPs hence assures a continuous feed of ZnO NPs that is intrinsically well-matched to the capacity of the synthesis reaction to incorporate these NP into the forming zeolite structure, similar to the well-established timed-release mechanisms in drug delivery which assure a continuous, low-level dose of a required drug. Correspondingly, if the ZnO concentration in the precursor ZnO@silica is increased to very high density, the resulting increased NP release rate starts to exceed the rate of encapsulation and instead results in the formation of irregular aggregates in addition to regular microshperes (Figure 12d). Moreover, if ZnO NPs are directly added into hydrothermal solution without pre-embedding in the silica matrix, rapid aggregation and settling occurs in the alkaline environment of the hydrothermal synthesis broth (Figure 6), resulting in

highly inhomogeneous materials composed of largely ZnO-free zeolite crystallites and poorly defined structures which contain mostly ZnO aggregates (Figure 14). Clearly, a very fine balance between NP release and encapsulation must be maintained to achieve a well-controlled, highly homogeneous NP@zeolite product structure.

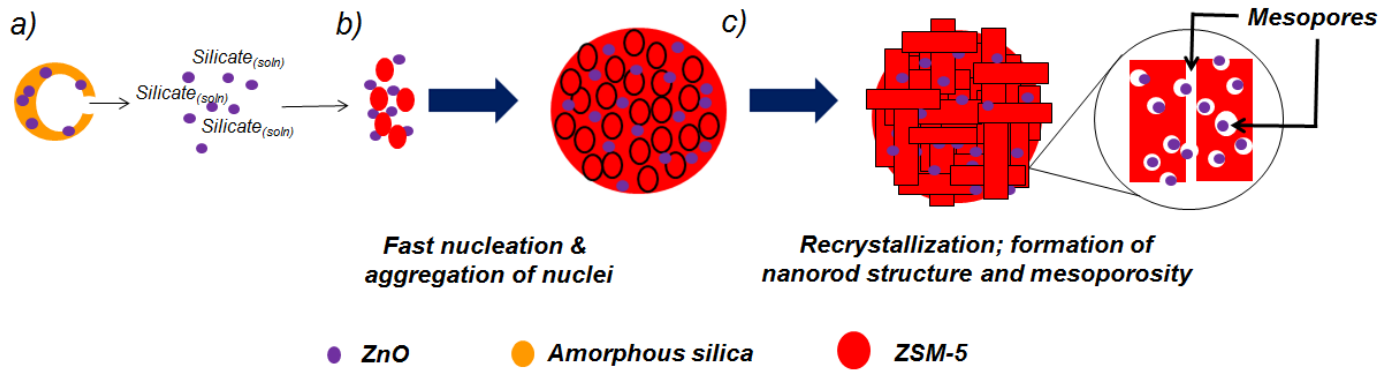

Scheme 1. Proposed "timed release mechanism" resulting in the formation of ZnO@ZSM-5 with aggregated nanorod structure: a) Dissolution of silica results in coordinated release of soluble silicate and metal oxide NPs; b) zeolite nuclei form and quickly aggregate around the NPs, forming a largely amorphous core@shell precursor structure; c) During re-crystallization of the zeolite, nanorod crystallites are formed, resulting in the final "stacked nanorod" morphology and in the formation of mesoporosity between the nanorods and surrounding the embedded NPs.

As the hydrothermal reaction progresses further, these aggregated aluminosilicate nuclei enter the growth stage. Normally, such aggregated ZSM-5 nuclei grow into single, larger crystals via an Ostwald ripening process[128]. However, the presence of the ZnO NPs in between the aggregated nuclei in the present synthesis alters the crystallization behavior of the zeolite significantly. As recently shown by Li et al.[112] the presence of embedded NPs changes the crystallization of the ZSM-5 phase to a surface-initiated crystallization which proceeds towards the core of the individual aggregate particles and during which the particle is broken up into the

striking “aggregated nanorod” structure due to the intercalation of the NPs (Scheme 1c). The larger the number of nanoparticles or the larger the particle size of the ZnO NPs, the more they disrupt the growth of the zeolite crystals. Energetically, it should be more favorable to align nanoparticles along the external surface of a nanorod-shaped crystallite rather than embedding them into the crystallite where they will result in a strong disruption of the zeolite lattice (since the NPs are much too large to be accommodated inside the zeolite micropores). Hence, an increase in NP number or size will favor the crystallization into more, and hence smaller, nanorods within a zeolite particle.

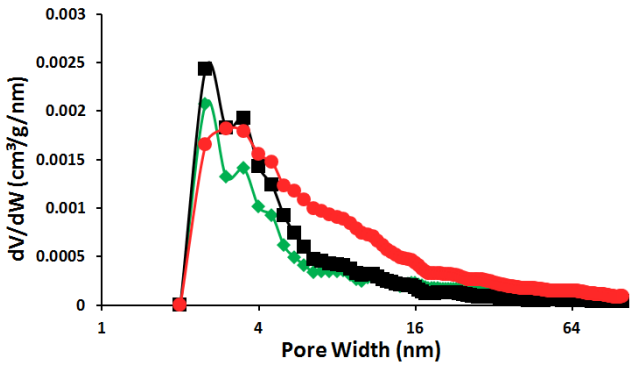

Figure 15. Pore width distribution of ZnO@ZSM-5 synthesized from different sizes of ZnO NPs: 3.8 nm ZnO@ZSM-5 (0.59 wt%; green-diamonds), 5.9 nm ZnO@ZSM-5 (2.3 wt%; black squares), and 13 nm ZnO@ZSM-5 (18.5 wt%; red circles). Note that in these tests, the number of embedded NPs was held constant by changing the weight loading to account for the different NP sizes.

At the same time, the incorporation of NPs both within the nanorod crystallites as well as between the nanorods creates significant mesoporosity (Scheme 1c), likely resulting from a combination of some mesoporosity around the embedded NPs as well as mesoporosity in between the nanorod crystallites. As a result, the mesopore volume scales close to linearly with the NP number (Figure 11d). However, albeit mesoporosity also increases with the NP diameter

(see Figure 15), the mesopore diameter does not scale in a simple way with NP size. While the mesoporosity that is created in this way (0.01-0.08 cm^3g^{-1}) is significantly lower than typical mesoporosities achieved via demetallation (0.10-0.50 cm^3g^{-1},[103]), the present approach is synthetically much more straightforward. More importantly, demetallation has to be conducted carefully to avoid non-uniform mesoporosity[48], while the present synthetic approach yields highly uniform mesoporosity in a straightforward way due to the homogeneous distribution of NPs throughout the sample (as for example indicated by the narrow pore size distribution; figure 15). Finally, demetallation alters the Si:Al ratio (SAR) in the zeolite – again often in a non-uniform way – and SAR is critical for catalytic performance of zeolite materials, as it determines the availability of Bronsted acid sites.

3.2.3 Flexibility of the synthesis strategy

The above described mechanism should in principle be applicable to virtually any metal or metal oxide nanoparticle that can be embedded into silica (for which a plethora of synthetic recipes exist in the literature). Since the encapsulation mechanism does not rely on (species-specific) capping agents or similar steps, but simply on the fine-tuned rates of the "timed release" of embedded NPs and subsequent capture by aluminosilicate nuclei, transfer to other NPs should be straightforward. To test the flexibility of the approach, we applied the same synthetic strategy to Fe- and Ni-based materials and found the same formation of aggregated-nanorod zeolite particle morphologies with embedded metal oxide nanoparticles and similar mesoporosity for these materials (figure 16).

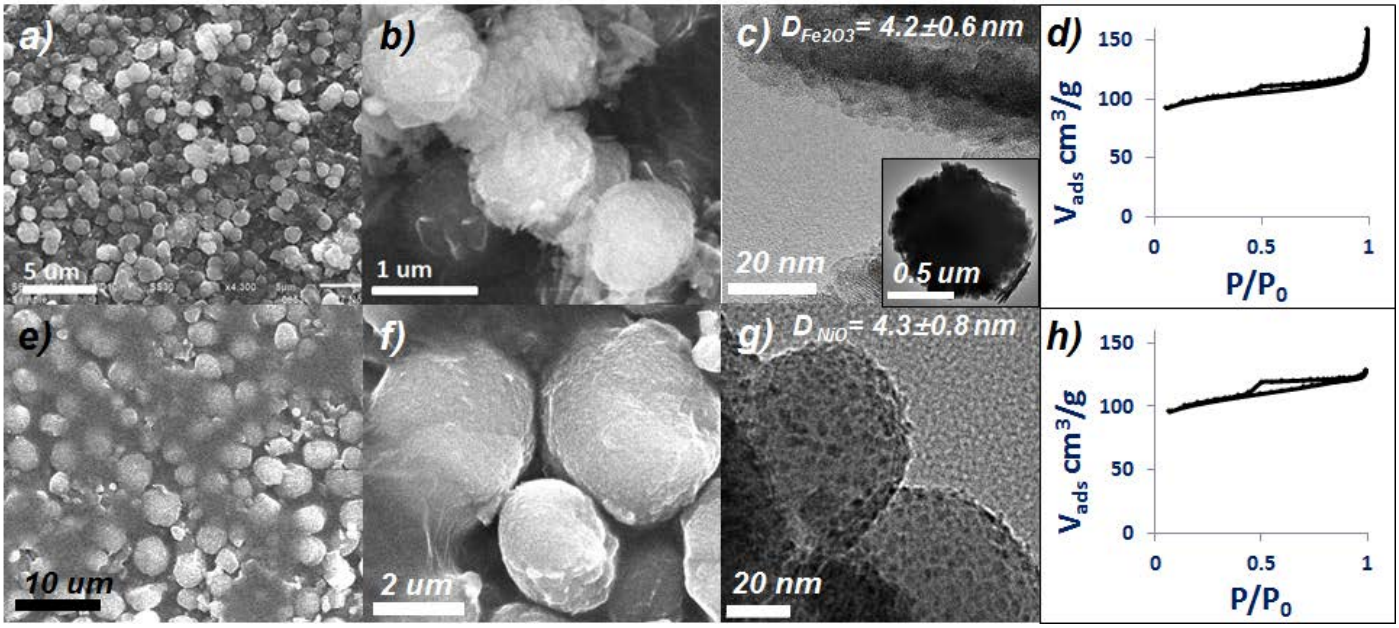

Figure 16. 8wt% Fe_2O_3@ZSM-5(a-d) and 8 wt% NiO@ZSM-5(e-h) synthesized from MeO@silica with the same hydrothermal condition used for ZnO@ZSM-5. (a), (b), (e), and (f) show SEM images of the morphology, while (c) and (g) are HRTEM images showing the presence of the oxide NPs. (d) and (h) show N_2 adsorption/desorption isotherms indicate the presence of mesopores.

3.2.4 Thermal stability of metal oxide @ ZSM-5

Finally, one can expect that zeolite encapsulation should result in strong stabilization of the embedded metal oxide NPs, protecting them in particular against thermal sintering due to the embedding in the micropore framework of the zeolite. In order to test whether the formation of the mesoporosity in the sample compromises this expected stabilization, samples were calcined at elevated temperature and then analyzed. TEM images were recorded before and after calcination of 8 wt% ZnO@ZSM-5 at 700 ^{0}C in air for 1hour (Figure 17). Before calcination, the majority of the ZnO NPs were generally about 6nm in diameter (Figure 17a). After calcination,

no significant change in particle size is observed (Figure 17b), indicating that the ZnO NPs of ZnO@ZSM-5 have an enhanced stability towards sintering. The successful stabilization of ZnO NPs is further corroborated by XRD before and after calcination (700 ^{0}C in air, 1hour; Figure 17d). No differences between the two XRD patterns of ZnO@ZSM-5 are discernible, and no distinct ZnO reflections (i.e. 2θ ~31.5^0 (100), ~34.5^0 (002) and ~ 36^0 (101)) can be observed in either XRD pattern. In contrast to the nanocomposite ZnO@ZSM-5, an 8wt% ZnO/ZSM-5 sample prepared by conventional wet impregnation showed severe sintering after the same thermal treatment, as seen in both TEM (figure 17c) and XRD (figure 17d). Thus, the described synthesis yields MeO@ZSM-5 nanocomposites which not only exhibit highly uniform structure and significant mesoporosity, but also enhanced sintering stability of the embedded metal oxide nanoparticles.

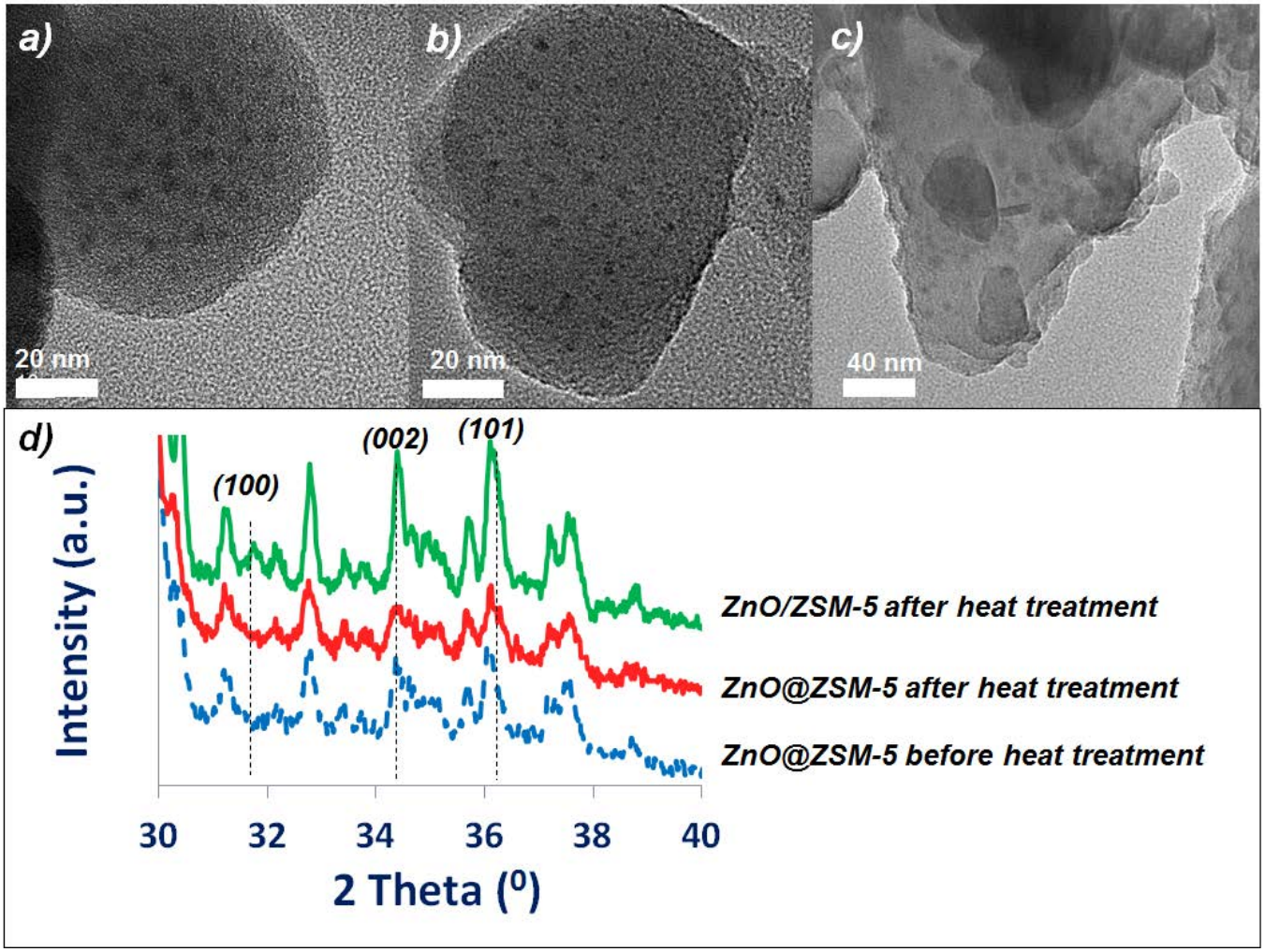

Figure 17. TEM of (8wt%) ZnO@ZSM-5 a) before and b) after a thermal treatment at 700 ^{0}C in air. c) TEM of ZnO/ZSM-5 prepared by impregnation after heat treatment at 700 ^{0}C in air. d) XRD patterns for ZnO@ZSM-5 before and after a thermal treatment at 700 ^{0}C in air and ZnO/ZSM-5 prepared by impregnation after a thermal treatment at 700 ^{0}C in air.

3.3 SUMMARY AND CONCLUSIONS

The formation of metal oxide @zeolite core-shell nanocomposite materials is of great technological interest due to the bifunctional catalytic properties of the resulting materials which combine catalytic functionality of metal oxide nanoparticles and of the zeolite matrix. For example, Mo_xO_y/HZSM-5[74] and ZnO/HZSM-5[129] catalysts are reported for methane dehydroaromatization reaction, where the metal site is responsible for methane activation and active site of HZSM-5 works for oligomerization. The core-shell nanocomposite materials furthermore constitute an efficient structure for stabilization of NPs against thermal sintering and/or shielding against chemicals that are larger than the zeolite micropore dimensions (~5.5 A for ZSM-5). However, the formation of such structures is to-date typically the subject of a costly and tedious trial-and-error procedure.

We presented here a straightforward and transferrable approach towards formation of such metal oxide@ZSM-5 nanocomposite materials. The approach consists of three steps: Synthesis of (size-controlled) metal oxide nanoparticles, encapsulation of these NPs into silica shells through a modified Stöber synthesis, and conversion of the silica shell to ZSM-5. The systematic bottom-up approach of building this material allows for straightforward, precise control of the metal weight loading as well as of the size of the embedded NP, enabling use of the vast literature on synthesis of size-controlled NPs for these nanocomposite materials. Key to the synthesis is the "timed release" of the embedded NPs during dissolution of the silica matrix in the hydrothermal conversion step: While metal oxide nanoparticles typically agglomerate and precipitate rapidly in solution, the present metal oxide@silica precursor structure results in a rate of NP release which is intrinsically balanced with the rate of Si dissolution and subsequent (rapid) formation of aluminosilica nuclei.

It can be expected that the synthetic approach should be applicable for encapsulation of metal and metal oxide nanoparticles into other zeolite structures as well, as long as the nucleation of the zeolite phase is a sufficiently rapid process and hence does not disturb the fine balance between the relative time scales of the different reaction steps.

4.0 ZN-HZSM5 CATALYSTS FOR METHANE DEHYROAROMATIZATION

Benzene is one of the most important organic intermediates in the petrochemical industry. Currently, it is mainly produced from crude oil processing. However, the increasing price difference between oil and natural gas due to the availability of abundant shale gas has renewed interest in the development of a process for the direct conversion of methane to benzene. This can be achieved via non-oxidative methane dehydroaromatization (DHA) with reported methane conversions of up to ~10% X_{CH4} and benzene selectivity of 80% at a typical reaction temperature of 700 °C over bi-functional Mo-HZSM-5 (catalysts)[2]. Over this catalyst, methane is activated on Mo sites (present in their active form as oxicarbide clusters) resulting in C-C coupling intermediates. Subsequently, these intermediates oligomerize on Bronsted acid sites (BAS) of HZSM-5 to form benzene[13, 16-17, 74]. The high benzene selectivity over this catalyst is attributed to the shape selectivity of ZSM-5 micropores[29].

However, the diffusion of large benzene molecules inside the micropores simultaneously enhances the chance for undesired further reactions on the BAS[13, 130], resulting in coking and hence deactivation of the catalyst. Regeneration is typically conducted via burn-off of the coke in an oxidative environment[15]. However, this burn-off also results in oxidation of the Mo species, and hence requires a lengthy activation period to convert Mo back into its active oxicarbide form[131]. Typically, Mo-HZSM-5 catalysts require regeneration every few hours (~5 hrs, although depending on the reaction conditions, this time can be even shorter[13]), and the required 0.5-1 hr activation time (along with low conversions) hence pose a significant hurdle for economic viability of the process.

While the existing literature for DHA predominantly focuses on Mo/HZSM-5 catalysts[15, 19, 132], the sensitive nature of the Mo-oxycarbide species motivates the search for alternate metals. Table 1 summarizes some of the reported transition metal/zeolite catalysts for methane DHA. Since coking is virtually unavoidable in aromatization reactions, and catalyst regeneration is hence required, a desirable feature of a DHA catalyst would hence be active in the oxidized state at which it exists from regeneration in order to avoid lengthy re-activation. However, similar to the Mo-based system, the majority of transition metals have been reported to be active in their reduced state. A rare exception is the claim by Wang et al.[2] that ZnO is the active phase in Zn/HZM-5 catalysts for DHA. However, the reported literature on Zn as DHA catalyst is limited [2, 91-92], and none of the published reports experimentally verified this claim. Nonetheless, zinc-containing zeolites have been extensively studied for aromatization of light alkanes (C_2 and C_3) [133-135]. Despite a debate whether the active zinc species is isolated Zn^{+2} or a multinuclear oxygenated zinc clusters, general agreement exists that the active phase is divalent Zn[70, 136-138]. Since Zn is expected to play a similar catalytic role in methane DHA as in light alkane aromatization, it hence seems reasonable to assume that Zn^{+2} is the active oxidation state in catalytic DHA.

Table 1. (Partial) literature survey of nonoxidative dehydroaromatization over transition metal loaded HZSM-5 zeolites.

Transition metal	Temp (^{0}C), GHSV (cc/g/h)	Initial oxide → Active phase	X_{CH4}	Benzene selectivity (S), yield (Y)	References
Mo	700, 1000	MoO_3 → Mo_2C	6-15%	S:60-85%	[2, 139]
Mn	700, 1600	Mn_3O_4 → MnO_xC_y	2.1%	Y:1.9%	[140]
Zn	700,1440	ZnO → ZnO	~3%	S:>90%	[2, 91]
W	700,960 (Or 750, 800)	WO_3 → WO_2	3~4% (or 0.3%)	S: 67% (0%)	[3, 141]
Fe	750, 800	Fe_2O_3 → Fe_3O_4	4%	S: 67-74%)	[3, 93]
V	750, 800	V_2O_5 → V_2O_3	0.6%	S: 63.1%	[3]
Cr	750, 800	CrO_3 → Cr_2O_3	0.3%	S:19.4%	[3]

In the present study, we therefore investigated the catalytic performance of various Zn-HZSM-5 catalysts in methane DHA. Three different synthesis approaches were used to prepare catalysts which contain different Zn species in order to obtain conclusive insight into the activity and stability of different Zn species for this reaction.

4.1 MATERIALS AND METHODS

4.1.1 Catalyst preparation

4.1.1.1 Wet ion exchange (Zn/HZSM-5) and impregnation method (ZnO/HZSM-5)

NaZSM-5 zeolite was synthesized by a hydrothermal condition. Typically, the molar composition used for synthesis is: Al_2O_3 : $80SiO_2$: 36TPAOH : $5Na_2O$: $4280H_2O$, from the mixture of sodium hydroxide (NaOH), silica particles (100- 300 nm), sodium alumina ($NaAlO_2$), and tetrapropylammonium hydroxide (TPAOH, 20 wt % in aqueous solution). The crystallization was conducted at 180 ^{0}C for 48 h in a Teflon-lined stainless steel autoclave. The solid product was recovered by centrifugation and washing with deionized water (DI water) for 4 times, followed by drying at 100 ^{0}C overnight and calcination at 550 ^{0}C for 6h in air. Converting the synthesized NaZSM-5 to HZSM-5 was achieved by ion exchange with aqueous NH_4NO_3 solution (1M) at 80 ^{0}C for 12h and subsequent drying at 100 ^{0}C and calcination at 500 ^{0}C for 5h.

Zn/HZSM-5 by ion exchange was acquired by stirring HZSM-5 powder in $Zn(NO_3)_2$ solution (0.005M) at 70 ^{0}C for 1h (Zn/HZSM-5-1) or for 24h (Zn/HZSM-5-24). The product was then washed with DI water for 4 times and dried at 100 ^{0}C overnight, followed by calcination at 500 ^{0}C for 20h. ZnO/HZSM-5 was prepared by incipient wet impregnation of HZSM-5 in $Zn(NO_3)_2$ solution, followed by drying at 100 ^{0}C overnight and calcination at 500 ^{0}C for 5h.

4.1.1.2 Core-shell method (ZnO@HZSM-5):

Core-shell approach was implemented with the following order[142]: (i) synthesis of ZnO NPs, (ii) encapsulation of ZnO NPs in amorphous silica, and (iii) convert the silica shell into ZSM-5 zeolite.

ZnO NPs were prepared by a sol-gel process. Typically, $Zn(OAc)_2 \cdot 2H_2O$ (1.48 g) in methanol (62.5 ml) was preheated to 60 ^{0}C with reflux, and then NaOH (0.52 g) dissolved in methanol (32.5 ml) was added to initiate hydrolysis and condensation of ZnO. The mixture was kept stirring at this temperature for 20 hrs. After the reaction, supernatant was removed by centrifuging. The ZnO NP was re-suspended in ethanol to wash away unreacted precursors and impurities, and the washing process was repeated three times.

ZnO was then encapsulated by amorphous silica via a Stöber synthesis condition. First, as-synthesized ZnO was re-dispersed in 200 ml of ethanol under ultrasound. 9.5 ml of tetraethoxysilane (TEOS) and 4 ml DI water were added into above colloid separately, and the mixture was treated with ultrasound for 20 mins. Next, 15.25 ml of ammonia (28 wt%) dissolved in 32.5 mL of ethanol was added slowly to the solution with continuous stirring and kept for 3 hrs at 55 ^{0}C. The product solution was then centrifuged and re-dispersed in ethanol for three cycles. The purified particles were dried and clacined at 500 ^{0}C for 2 hrs.

ZnO@SiO_2 composites were converted into the ZnO@ZSM-5 materials by a hydrothermal treatment. Typically, ZnO@SiO_2 composites was added to a mixture of NaOH, tetrapropylammonium hydroxide (TPAOH, 20 wt %), $NaAlO_2$ and deionized (DI) water to get a mole ratio of Al_2O_3 : 80SiO_2 : 36TPAOH : 5Na_2O : 4280H_2O : 10.5ZnO. The mixture was stirred for 2 h. Then the mixture was transferred to a Teflon-lined autoclave which was heated to 180 °C for 48 h. After cooling down to room temperature, the product (ZnO@NaZSM-5) is recovered

by centrifuging, washed with deionized water, and dried at 100 °C for overnight. Converting the synthesized ZnO@NaZSM-5 to ZnO@HZSM-5 was achieved by ion exchange with aqueous NH_4NO_3 solution (1M) at 80 ^{0}C for 12h and subsequent drying at 100 ^{0}C and calcination at 500 ^{0}C for 5h.

4.1.2 Catalyst characterization

4.1.2.1 X-ray diffraction (XRD)

Powder X-ray diffraction (XRD) measurements were performed with a high-resolution powder X-ray diffractometer (Bruker D8 Discover) using a monochromatic Cu radiation at the wavelength of 1.54 Å. The beam voltage was 40 kV at a current of 40mA. The diffraction patterns were recorded with a step of 0.02^0 (2θ), 0.5 sec/step.

4.1.2.2 Electron microscopy and X-ray microanalysis

JEOL JSM-6510LV field emission scanning electron microscope (SEM) was used to determine material morphology at beam voltage of 20kV. A thin palladium film was sputter coating on the sample before measurement. Nanoscale morphology was determined by a high resolution transmission electron microscopy (HRTEM, JEOL-2100). Samples were dispersed on a copper type-B support grid (Ted Pella Inc.). The actual chemical composition of Zn-HZSM-5 catalysts was determined by energy dispersive analysis of X-ray (EDX) equipped on SEM (JEOL JSM6510LV), with a collection time of 240- 300 s.

4.1.2.3 Ammonia adsorption-temperature programmed desorption (NH3-TPD)

NH_3-TPD experiments were carried out using a flow system with a thermal conductivity detector (Micromeritics Autochem 2910). Prior to each TPD run, the catalyst (~0.2 g) was heated to 500 ^{0}C for 30 min under pure He (50 sccm, ramp 5 ^{0}C/min) to remove all moisture. The catalyst was then cooled to 150 ^{0}C and exposed to 30 sccm 15% NH_3 in He for 30 min. The catalyst was purged with pure He gas to remove excess ammonia before the temperature was ramped up to 600 ^{0}C at 5 ^{0}C/min ramp rate to obtain NH_3-TPD data profile.

4.1.2.4 Temperature programmed reduction (H_2-TPR)

H_2-TPR was operated with a Micromeritics Chemisorb 2750 system equipped with a thermal conductivity detector. During the TPR analysis, the samples were first oxidized in 5% O_2/He at 500°C for 1 h, and then TPR was performed by heating the sample (100 mg) at 2 °C/min to 1000 °C in a 10% H_2/Ar flow (20 ml/min). A cold trap filled with acetone-dry ice mixture was placed between reactor and TCD to remove water vapor.

4.1.2.5 Micropore analysis

Microporosity was determined by using a Micromeritics ASAP 2020 unit. In order to remove surface humidity and preadsorbed gases, samples were degassed for 10 h at 300 °C under high vacuum prior to each analysis. Both nitrogen adsorption/desorption measurements were performed at liquid nitrogen temperature (77 K). The surface area was calculated from the N_2 isotherm data using the Brunauer–Emmett–Teller (BET) model. The micropore size distribution (PSD) was calculated by Saito and Foley (SF) method.

4.1.3 Reactivity evaluation

The reaction was carried out in a fixed-bed reactor at 700 ^{0}C and atmospheric pressure. Typically, catalysts were charged into a 5.0 mm i.d. quartz tubular reactor. The reactor tube was heated from room temperature up to 500 ^{0}C for catalyst pretreatment in air, and then heated to reaction temperature 700 ^{0}C under helium flow. After temperature equilibration, methane (12.5 sccm) was introduced onto the catalyst for various reaction times up to 300 min. The typically used gas hourly space velocity (GHSV) was 3750 (cc/g/hr) for catalytic performance comparison between different catalysts. Different GHSV which was achieved by changing the catalyst amount (while keeping methane flow rate) was only tested on ZnO@HZSM-5 catalyst. The effluent gas products were analyzed by both Balzers Quadstar GSD 300 mass spectrometer (MS) and Agilent 3000A Micro GC equipped with thermal conductivity detectors (TCD). An amount of 50% He was added to the methane feed as an internal standard. The methane conversion, selectivity of products was evaluated according to the carbon mass balance. Total coke formation was determined based on CO and CO_2 signal detected in MS during regeneration (under 20% O_2) of the spent catalysts.

4.2 RESULTS

4.2.1 Material characterization

Table 2. Chemical composition of the catalysts used in this study, as determined by EDX.

Sample	Prep. Method	Si/Al	Zn (wt%) *as synthesized*	Zn (wt%) *after reaction/regeneration cycles*
Zn/HZSM-5-1	Wet ion exchange, 1hr	31	0.31	0.32
Zn/HZSM-5-24	Wet ion exchange, 24hr	31	0.75	0.40
ZnO/HZSM-5	Wet impregnation	31	6.4	0.40
ZnO@HZSM-5	Core-shell synthesis	40	6.20	0.52
HZSM-5	Parent support	31	- -	- -

Table 2 shows the chemical composition of the catalysts used in this study. The Si/Al ratio is similar for HZSM-5 and zinc catalysts prepared by post-introduction of zinc on HZSM-5 (Si/Al = ~31), while this ratio is slightly higher (Si/Al = 40) in ZnO@HZSM-5 prepared by direct embedding of ZnO NPs during ZSM-5 crystallization/growth (core-shell method). The zinc content in ZnO/HZSM-5 is in good agreement with that in ZnO@HZSM-5 (~6.0 wt% Zn). Much lower Zn loading was obtained via ion-exchange, depending on the duration of the ion-exchange, ranging from 0.31 wt% Zn (1h exchange) to 0.75 wt% Zn (24 hr exchange).

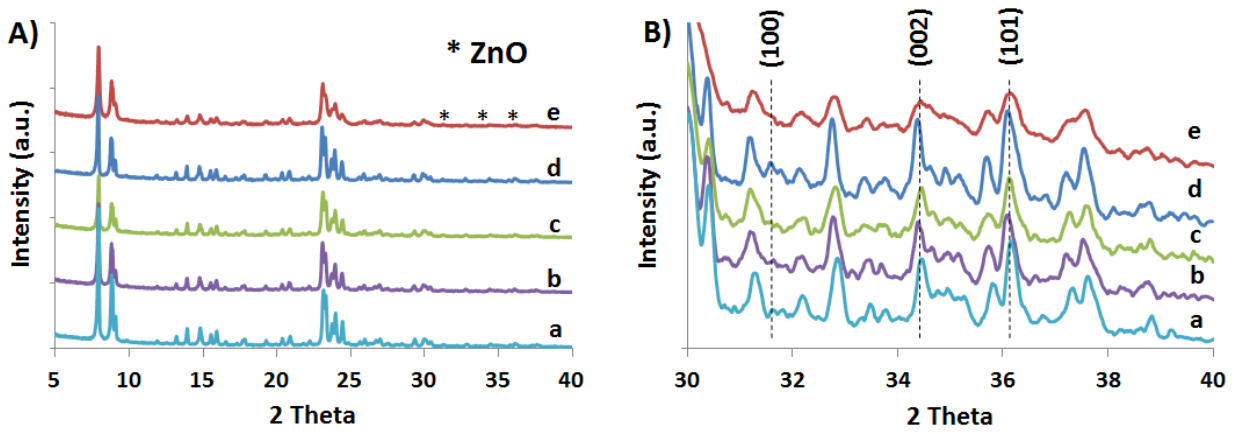

Figure 18. XRD patterns at 2 theta of 5- 40 A) and exploded view of 30- 40 B) of HZSM-5 and Zn-containing HZSM-5 prepared by different methods. a) HZSM-5, b) Zn/HZSM-5-1, c) Zn/ZSM5-24, d) ZnO/HZSM-5, and e) ZnO@HZSM-5. The dashed lines indicate the locations of the (100), (002), and (101) ZnO diffractions.

Pure HZSM-5 and Zn-containing HZSM-5 prepared by all three methods exhibit identical diffraction patterns in XRD, indicating the MFI zeolite structure of all catalysts (figure 18A). The peak intensity (crystallinity) differs, however, with that of ZnO@HZSM-5 noticeably lower than that of others. This is not surprising, since the presence of ZnO NPs with diameters larger than the zeolite micropores must disrupt the crystal pattern of the zeolite and hence affect the ZSM-5 crystallization behavior during the hydrothermal synthesis. ZnO reflections are only distinguishable in ZnO/HZSM-5 prepared by impregnation (against strong reflections from ZSM-5, figure 18B), suggesting that larger ZnO particles exists in this catalyst. Thus, XRD results suggest that only the zinc species introduced by ion exchange methods are well dispersed in the HZSM-5 zeolite.

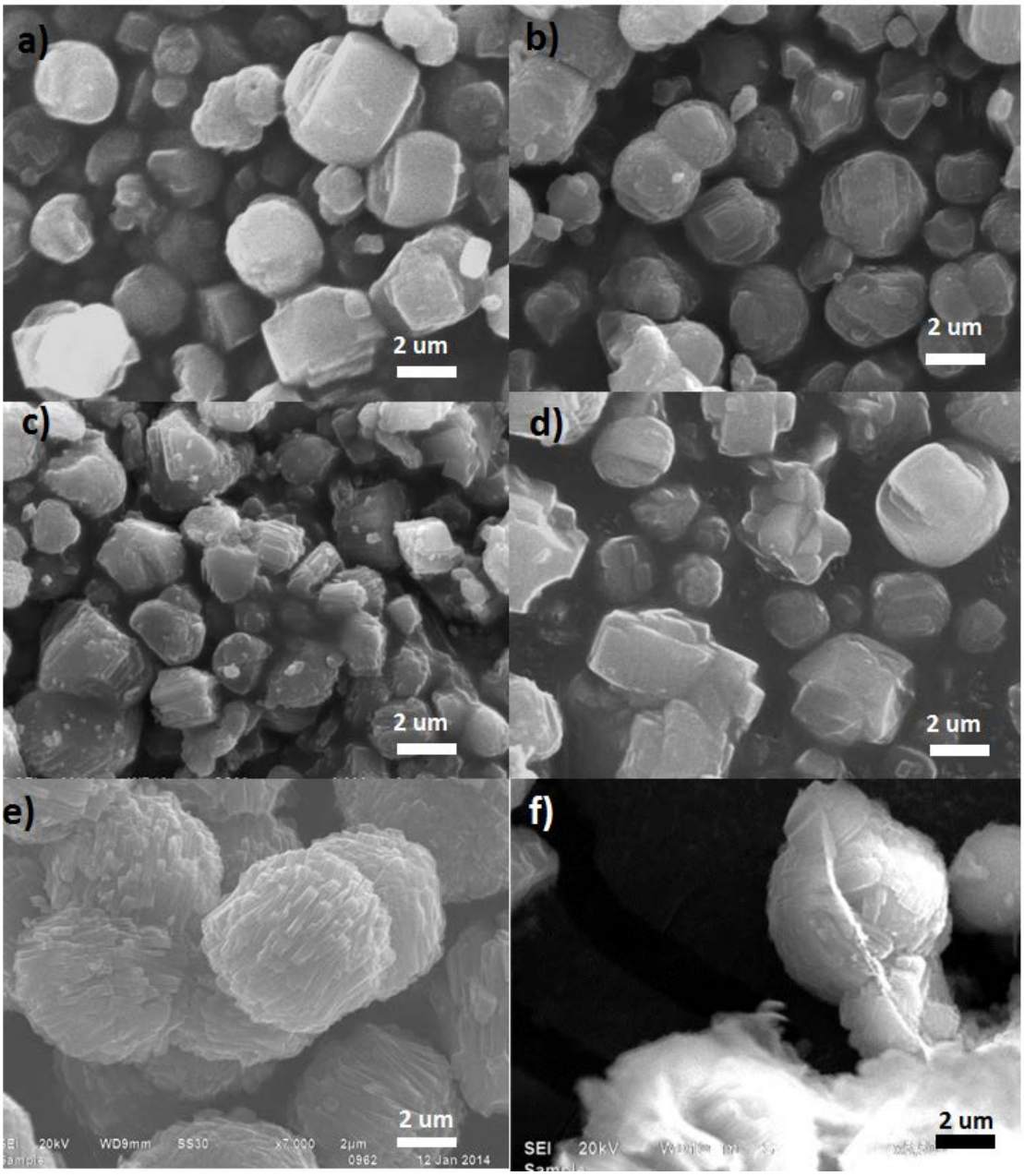

Figure 19. SEM images of HZSM-5 and Zn-containing HZSM-5 prepared by different methods: a) HZSM-5-1, b) Zn/HZSM-5-1, c) Zn/ZSM-5-24, d) ZnO/HZSM-5, e) ZnO@HZSM-5 and f) grounded ZnO@HZSM-5.

SEM imaging of HZSM-5 and Zn-containing HZSM-5 zeolites (figure 19) indicates that the introduction of zinc species by post-treatment (impregnation and ion exchange) has no influence on the crystal size and the morphology of the parent HZSM-5 which forms particles with the conventional coffin/cube shape of ZSM-5 (figure 19a). In contrast, the morphology of the ZnO@HZSM-5 is changed dramatically, forming microspheres composed of a multitude of aggregated nanorods (figure 19e,f). Consistent with XRD result, this confirms that that presence of ZnO NPs during the synthesis strongly influences nucleation and growth of the ZSM-5, as also recently reported by ourselves and others[112, 143].

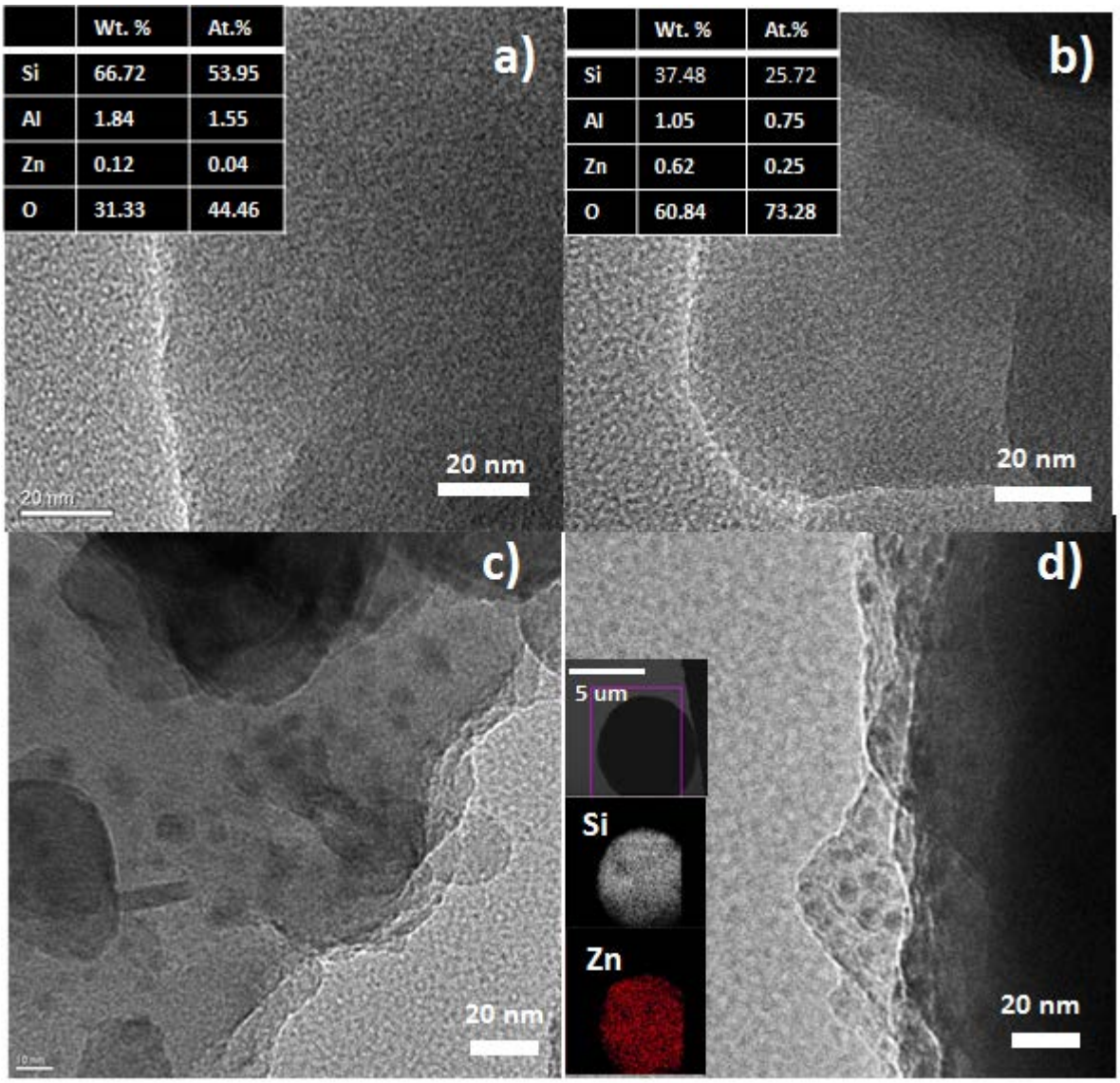

Figure 20. HRTEM micrographic of the Zn-containing HZSM-5 catalysts investigated in this study: a) Zn/HZSM-5-1, b) Zn/ZSM-5-24, c) ZnO/HZSM-5, and d) ZnO@HZSM-5. The inset of a) and b) shows the chemical compositions (by EDX) for the area of HRTEM image taken for Zn/HZSM-5-1 and Zn/ZSM-5-24, respectively. The inset of d) shows an EDX mapping for a microsphere from ZnO@HZSM-5.

The ZnO NPs dispersed in HZSM-5 prepared by different methods were further investigated by HRTEM (figure 20). For the ion exchange catalysts, no visible NPs could be observed (figure 20a,b), although EDX confirms successful incorporation of Zn in the imaged

area (see inset of figure 20a,b). This again suggests that only very small zinc species, located inside the micropores, are formed by this preparation method[134, 142, 144], consistent with the XRD findings that suggested the presence of only well dispersed zinc species in the ion exchange catalysts (and hence absence of Zn diffractions and an unperturbed ZSM-5 diffraction pattern).

ZnO NPs exist both in/on ZnO/HZSM-5 and ZnO@HZSM-5 (figure 20c,d). However, location and particle size of the ZnO NPs are very different between these two materials. For ZnO/HZSM-5, ZnO NPs show a very wide size distribution from ~2 nm nanoclusters to > 20 nm NPs. Furthermore, while not obvious from the TEM images, these observed ZnO NPs can only be located on the external surface of ZSM-5 due to the fact that Zn is introduced via post-synthetic impregnation and the micropores of ZSM-5 are too small to accommodate NPs >1 nm. In contrast, for ZnO@HZSM-5, EDX mapping (figure 20d, inset) shows that ZnO is well-dispersed throughout the ZnO@HZSM-5 particles, suggesting successful encapsulation of ZnO NPs in HZSM-5 via the core-shell approach. Moreover, as expected from the synthesis procedure, this catalyst contains a narrow and very homogeneous size distribution of ZnO NPs with an average diameter of ~6 nm.

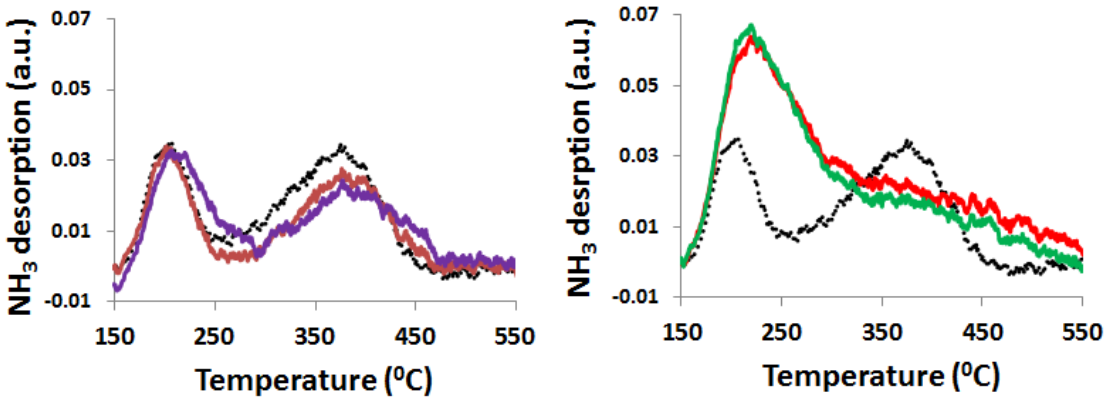

Figure 21. NH_3-TPD profiles of HZSM-5 and Zn-containing HZSM-5 prepared by different methods: Left graph: parent HZSM-5 (dotted-black), and ion-exchanged catalysts (1hr exchanged Zn/HZSM-5-1, brown; and 24 hr exchanged Zn/ZSM-5-24, purple). Right graph: parent HZSM-5 (dotted-black), wet impregnated ZnO/HZSM-5 (green), and core-shell ZnO@HZSM-5 (red).

Beyond structure and morphology, the presence of acid sites in zeolite catalysts is crucial for their catalytic functionality. NH_3-TPD was hence utilized to determine the concentration of acid sites in both the parent HZSM-5 and Zn-containing HZSM-5. The NH_3-TPD profile of HZSM-5 (figure 21, dotted-black lines in both graphs) shows the typical two desorption peaks, i.e. the high temperature peak at about 400 ^{0}C, typically ascribed to Bronsted acid sites (BAS), and a low-temperature peak at ~200 ^{0}C, assigned to weak acid site (mostly Lewis acid sites)[95, 108]. For ion-exchanged catalysts (fig. 21, left graph), the peak at ~400 ^{0}C decreases as a result of the ion exchange for the 1h exchanged catalyst, indicating that protons were successfully exchanged by Zn. However, only a minimal further decrease of BAS is observed for the extended 24h ion-exchange. Instead, the low-temperature peak at ~200 ^{0}C shifts to slightly higher temperatures and a shoulder appears at ~450 ^{0}C. This shoulder was previously attributed to strong Lewis acid site of Zn^{+2}.[108, 135] Similarly, the shift of the ~200 ^{0}C peak was also previously attributed to stronger Lewis acid sites created by metal oxides[89], suggesting that a

prolonged ion-exchange predominantly results in zinc oxide formation. In combination with the results from XRD and TEM (figure 18B, 20b), which suggested the presence of highly dispersed Zn species in Zn/HZSM-5-24, we interpret these results to indicate the formation of small ZnO nanoclusters inside the zeolite micropores. Thus, while shorter (1h) ion-exchange, which results in very low weight loading (0.31 wt% Zn), only results in the deposition of Zn^{+2} at the cationic exchange site of the zeolite, a longer ion-exchange (24h), which yields higher weight loadings (0.75 wt% Zn), results in the formation of ZnO nanoclusters in addition to Zn^{2+} species, similar to recent reports by Penzien et al. for Zn-HBEA prepared by ion exchange[144].

ZnO/HZSM-5 and ZnO@HZSM-5 show similar NH_3-TPD spectra, which differ distinctly from the parent zeolite (fig. 21, right graph). The spectra are dominated by a prominent peak at ~200 ^{0}C with two weak shoulders at ~400 ^{0}C and ~450 ^{0}C. In agreement with the discussion above, we attribute the prominent peak at ~200 ^{0}C and the shoulder at ~450 ^{0}C to the presence of a significant number of ZnO particles in both the impregnation and core-shell catalysts. However, while both catalysts show a similar loss of BAS (as apparent in the reduction of the peak at ~400 ^{0}C), the cause of this loss is different between these two catalysts. For ZnO/HZSM-5, the TEM and XRD results suggested that ZnO NPs are present on the external surface. Generally, such species should hence not influence the number of BAS[95]. Due to the post-synthetic preparation method (impregnation) of this catalyst, some protons are exchanged with Zn^{+2} at the cationic exchange sites in the zeolite micropores and hence result in a decrease in the number of BAS, as commonly observed for Zn-zeolite catalysts prepared by this synthetic method[137-138].

Similarly, the embedded ZnO NPs in ZnO@HZSM-5, which are much too large to be located inside the micropores, should have very limited influence on BAS. However, since in-

situ incorporation of ZnO during the synthesis of the zeolite for ZnO@HZSM-5 results in a lower crystallinity of this material (figure 18A), this loss of crystal order may account for the lower BAS[145] Additionally, this catalyst has a slightly higher Si/Al which will cause lower acidity, and the ~22% reduction of Al concentration in this catalyst compared to the parent zeolite is rather close to the ~28% reduction in BAS (estimated from the reduction in the peak area at~400 ^{0}C).

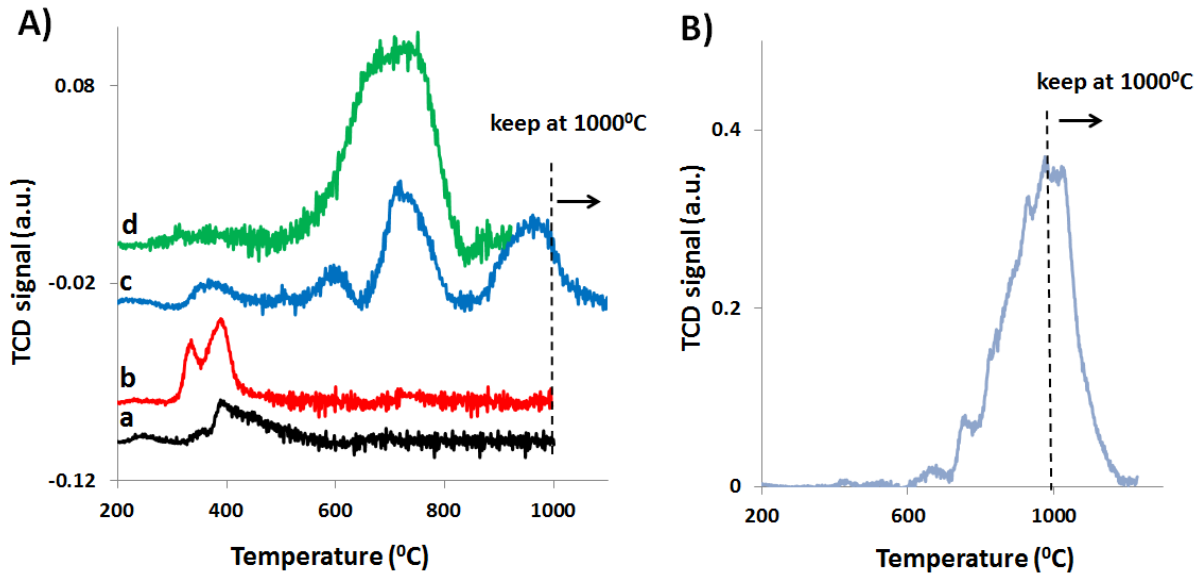

Figure 22. A) H_2-TPR spectra of the four Zn-HZSM-5 catalysts: a) Zn/HZSM-5-1, b) Zn/ZSM-5-24, c) ZnO/HZSM-5, and d) ZnO@HZSM-5. B) H_2-TPR spectrum of bulk ZnO for comparison.

Finally, H_2-TPR was used to further investigate the distribution of Zn species in the four Zn-HZSM-5 catalysts (figure 22A). For the 1h ion exchange catalyst (Zn/HZSM-5-1), only small H_2-consumption peaks at ~300-400 ^{0}C are observed. Zn^{+2} at the zeolitic exchange sites are known to be non-reducible due to the charge compensation in zeolite[134]. Hence, this result is

consistent with the above results indicating that this catalyst only contains Zn^{2+} at exchange sites. The observation of the very small, broad peak could be due to the presence of a minor population of (reducible) ZnO nanoclusters, as a comparison with the 24h ion exchanged catalyst suggests: The latter shows H_2-consumption peaks in the same temperature range, although the peaks appear more distinct. Since the discussion above had suggested the presence of a significant number of ZnO nanoclusters in this catalyst, these peaks likely result from reduction of these nanoclusters.

The results hence lead to the overall conclusion that the H_2-consumption in the ~300 ^{0}C to 400 ^{0}C range is associated with small ZnO clusters in the zeolite micropores.

The H_2-TPR spectrum of the ZnO@HZSM-5 catalyst looks fundamentally different from those of the ion-exchanged catalysts (fig. 22A, curve d): No H_2-consumption is observed between ~300 ^{0}C to 400 ^{0}C, in agreement with the absence of ZnO nanoclusters in the micropores of this catalyst. Instead, a broad peak between 600-700 ^{0}C is observed. The ratio of H_2 consumption to Zn content in the catalyst is calculated to be ~0.93, i.e. close to the stoichiometrically expected ration of 1 for reduction via $ZnO + H_2 = Zn + H_2O$, confirming that (virtually) all Zn is present in the form of reducible ZnO NPs in this catalyst. Furthermore, since the catalyst contains highly monodisperse 6 nm ZnO NPs (by virtue of the synthesis approach) the peak between 600-700 ^{0}C can hence be assigned to the reduction of ZnO NPs in this size range.

Finally, the catalyst prepared via impregnation shows the most complex spectrum characterized by multiple reduction peaks (fig. 22A, curve c). A small H_2-consumption peak at ~300-400 ^{0}C suggests the presence of small ZnO nanoclusters in zeolite micropores, while peaks at 600-700 ^{0}C indicate ZnO NPs. As expected from the synthesis procedure, this catalyst contains

a broad distribution of ZnO nanoclusters and NPs throughout the material. Beyond those, large ZnO aggregates (i.e. >20 nm) also exist in this catalyst, as seen in TEM, and confirmed by the high temperature peak at ~950 ^{0}C. The attribution of this peak is supported by H_2-TPR of bulk ZnO (figure 22B). A calculated H_2/Zn ratio of 0.88 further suggests that most zinc species in this catalyst are reducible, although a small non-reducible fraction might exist as well.

H_2-TPR thus yields a fairly sensitive probe for particle size distribution of ZnO NPs (i.e. the larger the NP, the higher the required reduction temperature), and, as expected, the catalysts prepared via impregnation result in the largest degree of heterogeneity of metal species in the zeolite[133, 138, 146].

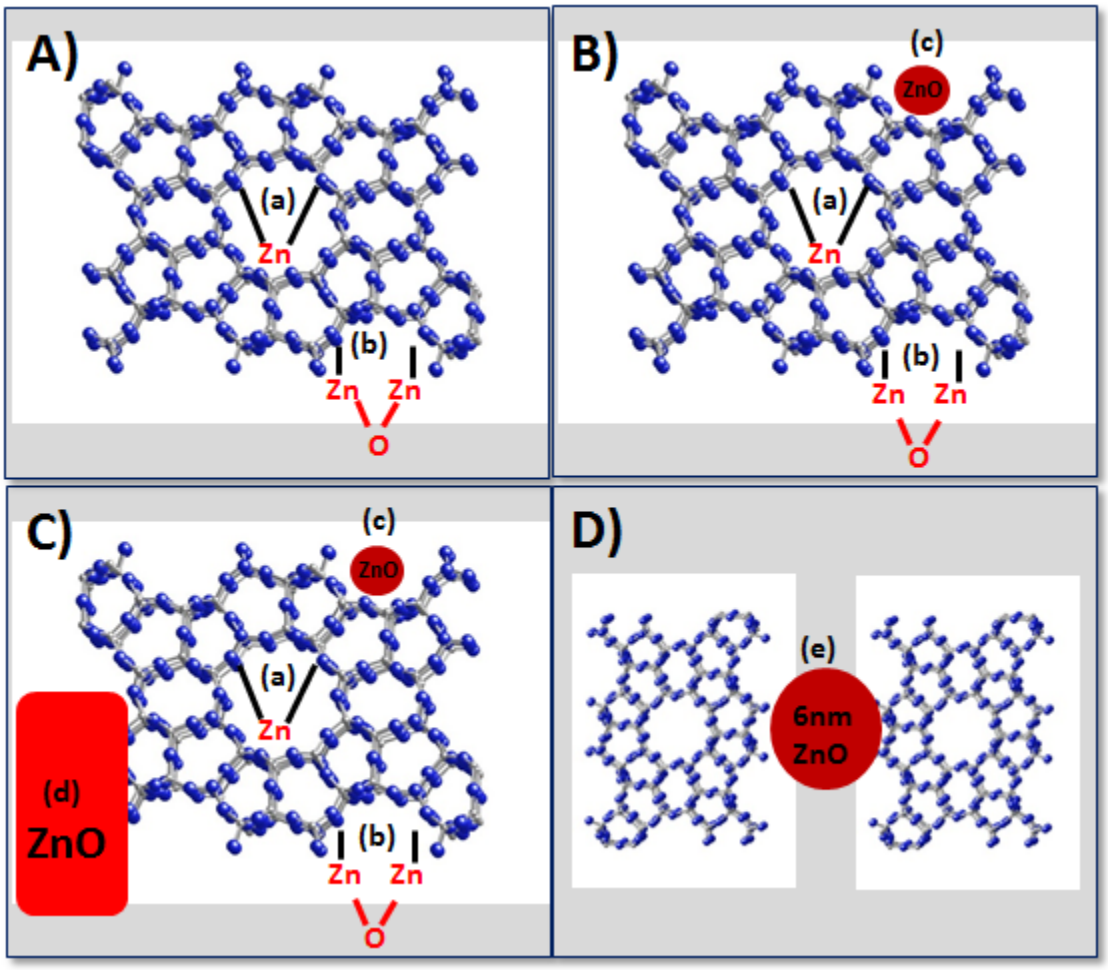

Figure 23. Schematic representation of zinc species in Zn-HZSM-5 prepared by different methods: A) Zn/HZSM-5-1, B) Zn/ZSM-5-24, C) ZnO/HZSM-5, and D) ZnO@HZSM-5. Different zinc species are mononuclear Zn at cationic exchange sites (a), binuclear zinc at cationic exchange sites (b), ZnO nanoclusters in micropores (c), ZnO NPs on external surface (d), and ZnO NPs encapsulated within ZSM-5 crystals (e).

Overall, the different characterization techniques (XRD, HRTEM, NH_3-TPD, and H_2-TPR) to assess the type of Zn species in the catalysts yield very good agreement, and the result clearly show that the distribution of zinc species (Zn^{+2} at cationic exchange sites, ZnO nanoclusters, and ZnO NPs) is strongly determined by the sample preparation, summarized schematically in figure 23.

4.2.2 Catalytic performance in DHA

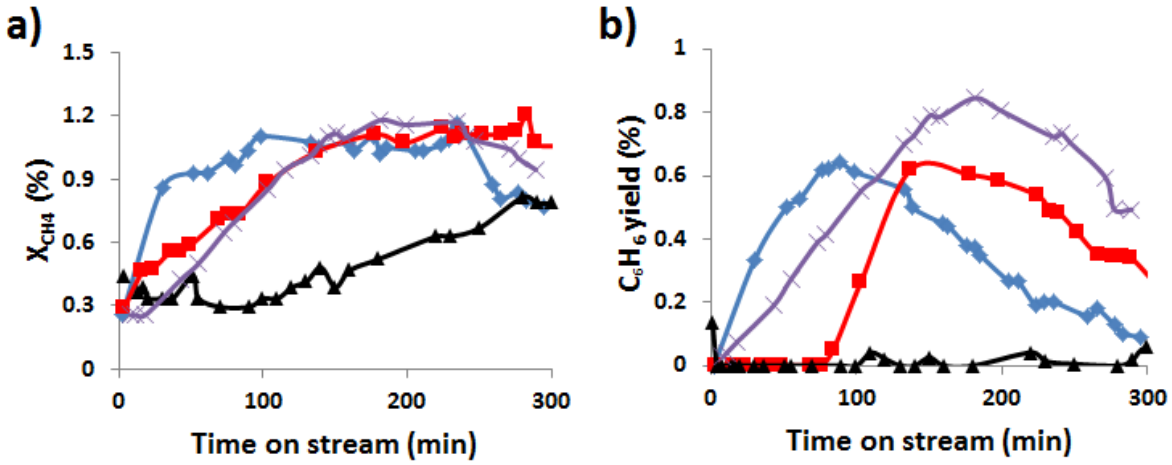

Figure 24. a) Methane conversion and b) benzene yield vs time on stream for Zn-containing HZSM-5: Zn/HZSM-5-1 (black triangle), Zn/ZSM-5-24 (purple asterisk), ZnO/HZSM-5 (blue diamond), and ZnO@HZSM-5 (red squares). Reaction conditions: T=700 ^{0}C, GHSV: 3750 cc/g/h (50% CH_4 and 50% He).

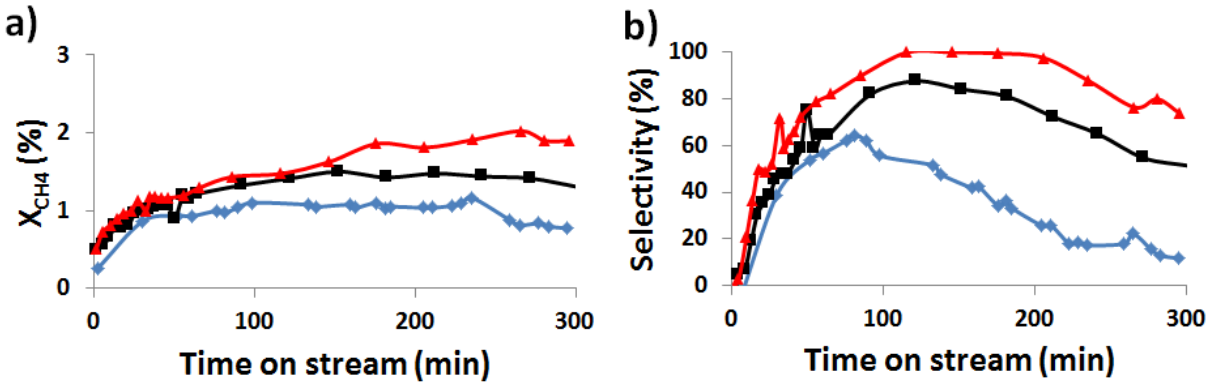

Figure 25. a) Methane conversion and b) selectivity to benzene over ZnO@HZSM-5 at different GHSV(50% CH_4 and 50% He): 1250 cc/g/h (red triangles), 1825 cc/g/h (black squares), 3750 cc/g/h (blue diamonds). Reaction temperature: 700^{0}C.

Following the characterization of the catalysts and identification of the Zn species, the catalytic performance of the four catalysts in methane dehydroaromatization was evaluated next in order to assess activity/selectivity correlations with the respective Zn species. Figure 24 shows key results in terms of methane conversion and benzene yield vs time-on-stream at an (isothermal) temperature of 700 ^{o}C. Methane conversions for all catalysts are low, with a similar maximum for Zn/HZSM-5-24, ZnO/HZSM-5 and ZnO@HZSM-5 (~1.2 %), while the one for Zn/HZSM-5-1 is significantly lower (~0.8%) and occurs with a time delay. Benzene yield roughly follows this trend, although Zn/HZSM-5-24 exceeds the other catalysts slightly. Barely any benzene yield was found for Zn/HZSM-5-1, i.e. this catalyst not only shows low reactivity but also low selectivity to benzene. Decreasing the GHSV results in increased methane conversion as well as higher benzene selectivity (figure 25). However, since the aim of the present study was on identification of active and stable species in the catalyst, rather than optimization of performance, no further effort was expended on identification of conditions for maximum benzene yield.

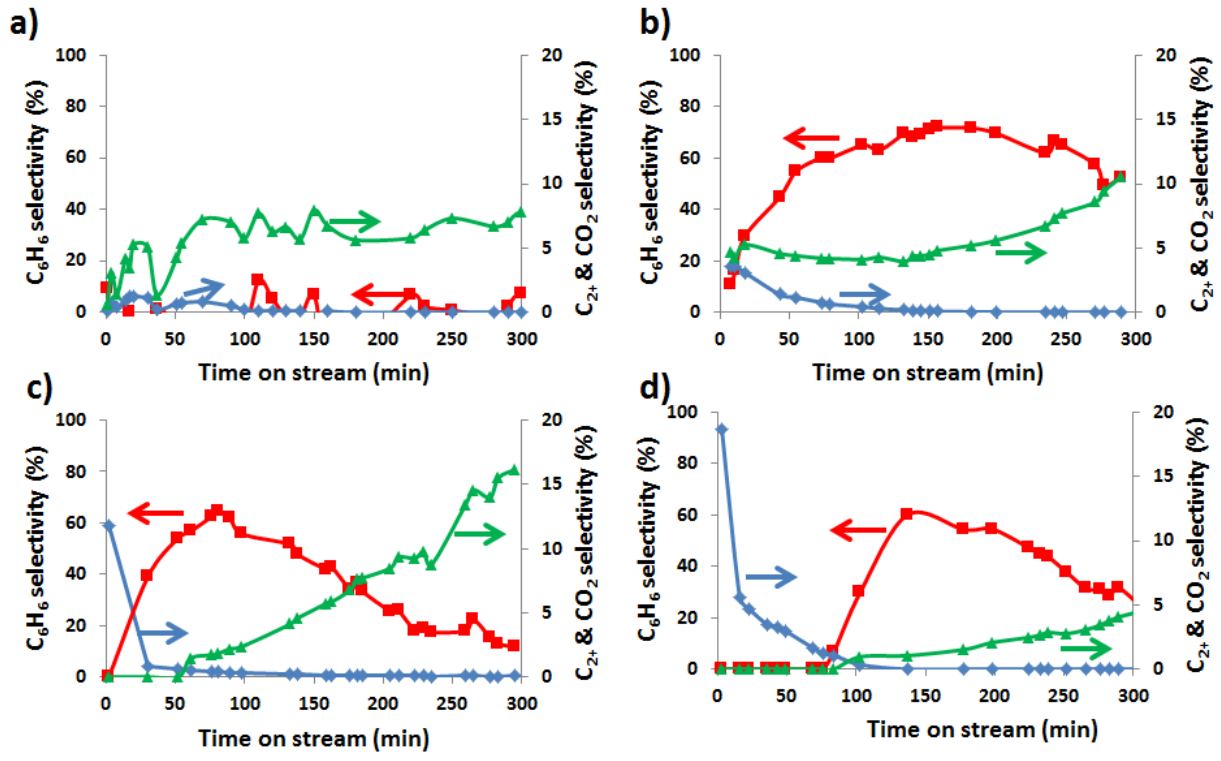

Figure 26. Product selectivity of DHA with the time on stream over Zn-HZSM-5 prepared by different methods: (a) Zn/HZSM-5-1, (b) Zn/ZSM-5-24, (c) ZnO/HZSM-5, and (d) ZnO@HZSM-5. Shown are benzene selectivity (red square), CO_2 selectivity (blue diamond), and C2+ selectivity (green triangle). Reaction conditions: T=700 ^{0}C, GHSV: 3750 cc/g/h (50% CH_4 and 50% He).

The break-down of product selectivities in methane DHA over the four catalysts is shown in figure 26. The maximum benzene selectivity of Zn/HZSM-5-1, Zn/HZSM-5-24, ZnO/HZSM-5 and ZnO@HZSM-5 is ~0%, 72%, 61%, and 64%, respectively. Due to the absence of any significant activity or selectivity, the 1h ion-exchanged catalyst will be excluded from further discussion. All three active catalysts show qualitatively similar behavior, which is most clearly apparent in the impregnation catalyst (fig. 26c). The reaction goes through three stages: After a brief initial total oxidation phase, where predominantly CO_2 is formed, the reaction shows a phase with good selectivity for aromatization, before the selectivity switches to increasing formation of C2 products.

Since CO_2 formation in DHA reaction over ZnO-HZSM-5 can only result from reduction of ZnO, as also consistent with its occurrence in the initial stage of the reaction, where the catalyst is fully oxidized, this suggests that—in contradiction to the claim in the literature[2, 91], ZnO is not the active phase for aromatization. This conclusion is also different from observations for DHA of higher alkanes[70, 136-138]. As a result, an extended induction time (~1 h) is observed for all catalysts before observing significant aromatization activity.

The drop in benzene selectivity accompanied by increased C_2 selectivity can be explained based on the widely accepted aromatization mechanism in which C_2 is a key intermediate in methane DHA and zeolite BAS catalyze aromatization (i.e. ring closing) from these intermediates[15, 139]. The results hence suggest that the BAS become deactivated in the course of the reaction, likely by coking as also widely observed for Mo/HZSM-5 catalysts[13, 15].

Table 3. Coking data for zinc-containing HZSM-5 prepared by different methods.

Catalyst	Coke amount (mg)[a]	Coke selectivity (%)[b]	Benzene selectivity (%)[c]	Coke(mg)/benzene formed (mg)
Zn/HZSM-5-24	3.86	36.3	53.8	0.621
ZnO/HZSM-5	3.09	32.9	50.2	0.716
ZnO@HZSM-5	2.93	30.4	40.3	0.698
Zn/HZSM-5-1	0.03	0.4	0.60	0.680

a.Coke amount was determined by CO and CO_2 generated during regeneration after 5h reaction over 100mg catalysts.
b & c. Selectivity was determined over 5h-period reaction.

Interestingly, quantifying the amount of coke formed over each catalyst via carbon burn-off after the reaction (table 3), we find that benzene selectivity and carbon (coke) selectivity show parallel behavior, with their ratio quite consistent between 0.62-0.72, even for the almost entirely inactive Zn/HZSM-5-1 catalyst. Increasing coke formation with increasing benzene production suggests that coke is likely formed via secondary reactions of benzene on the BAS of zeolite[77].

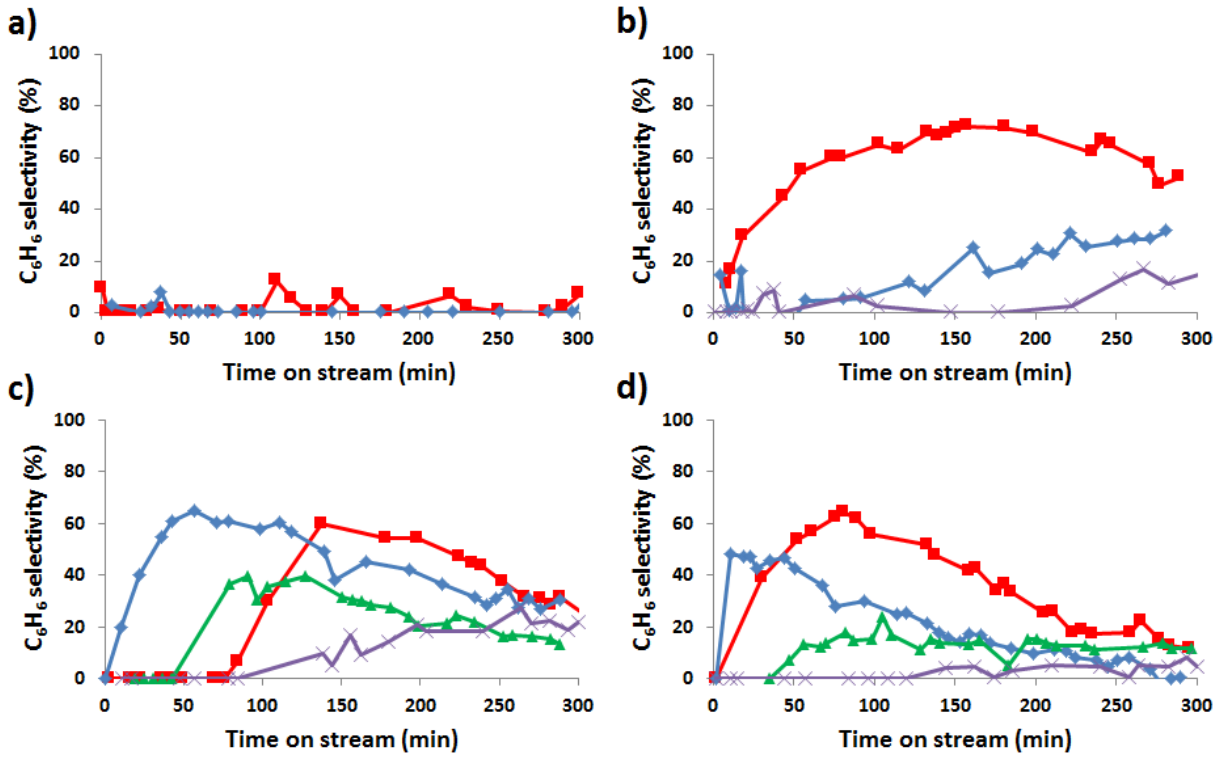

Figure 27. Selectivity to benzene during subsequent reaction-regeneration cycles in DHA vs time on stream over the four catalysts: (a) Zn/HZSM-5-1, (b) Zn/ZSM-5-24, (c) ZnO/HZSM-5, and (d) ZnO@HZSM-5. 1st cycle: (red square), 2nd cycle: (blue diamond), 3rd cycle: (green triangle), and 4th cycle: (purple asterisk). Reaction condition: T=700 ^{0}C, GHSV: 3750 cc/g/h.

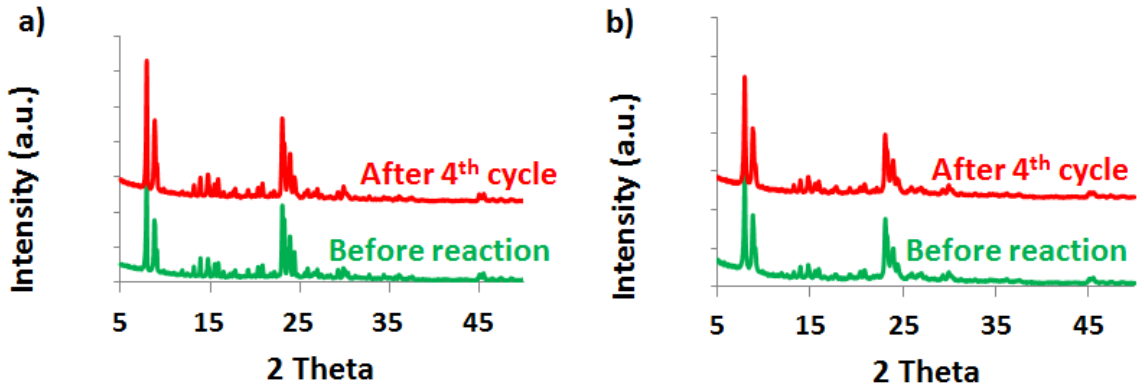

Figure 28. XRD patterns for fresh and spent catalysts: (a) ZnO/HZSM-5 and (b) ZnO@HZSM-5.

Due to the strong coke formation during reaction, the catalysts were also evaluated in repeated reaction-regeneration cycles, where regeneration took place by periodically burning off the carbon using an air feed at 600 ^{0}C. Figure 27 shows the benzene selectivity vs time-on-stream for four subsequent cycles. Strong and irreversible deactivation is observed for all catalysts over the four cycles with very little to no benzene selectivity remaining at the 4th cycle. This deactivation can be quite easily understood, considering the reduction of ZnO to Zn by methane (discussed above) in conjunction with the very high vapor pressure of metallic Zn at the reaction conditions[134, 138]. Zn is hence expected to be lost from the catalyst via evaporation during the reaction cycle as confirmed via measurement of Zn content in the spent catalysts (see table 2) and further evidenced by the formation of a Zn "mirror" in the cold zone of the quartz reactor tube downstream of the catalyst. Interestingly, the final Zn concentration for all spent catalysts is similar (0.32- 0.52 wt%) and close to the initial concentration in the Zn/HZSM-5-1 catalyst which is the only catalyst that shows a stable Zn concentration. While loss of benzene selectivity could also result from zeolite structure degradation at the severe reaction conditions, no change in ZSM-5 crystallinity was observed (figure 28). The results hence strongly point towards loss of Zn from the catalysts as the cause for the loss of catalytic activity.

4.2.3 Discussion: Active Zn species in Zn-HZSM-5

The above results show that the three different synthesis strategies—post-synthetic insertion via wet ion exchange or wet impregnation, and core-shell embedding of ZnO NPs into ZSM-5 during zeolite crystallization/growth—result in distinctly different materials with different distribution of Zn species and different reactivity. This allows formation of correlations between the zinc species in HZSM-5 and their catalytic performance in methane aromatization via DHA.

Zn/HZSM-5-1. For the 1h ion-exchanged catalyst, Zn/HZSM-5-1, HRTEM and NH_3-TPD show that this catalyst contains only Zn^{+2} at the cationic exchange site. Due to the charge balance within the zeolite system, Zn^{+2} species located at the exchange site of this catalysts are non-reducible[134], resulting in the absence of CO_2 formation during reaction as well as good thermal stability. However, this catalyst showed no aromatization activity and hence suggests that metallic Zn, rather than Zn^{2+}, is the active species required for aromatization.

Zn/HZSM-5-24. Extended ion exchange in the Zn/HZSM-5-24 results in the formation of small ZnO nanoclusters in the zeolite micropores in addition to Zn^{+2} as confirmed via TEM, NH_3-TPD, and H_2-TPR. These additional ZnO nanoclusters are reducible, as seen via H_2-TPR and in the CO_2 formation during the reactive studies. However, the reduced Zn nanoclusters are volatile and evaporate, resulting in a significant Zn loss during reactions. The increase in benzene selectivity upon initial reduction of the ZnO along with the irreversible loss of aromatization activity upon Zn loss strongly point towards metallic Zn as the active species for aromatization. Furthermore, the fact that Zn/HZSM-5-24 shows the highest benzene selectivity among all catalysts studied indicates that the location of the metallic Zn nanocluster inside the HZSM-5 micropores, i.e. the close proximity with the BAS of the zeolite and potentially contributions from shape effects of the MFI pores, results in highest benzene selectivity.

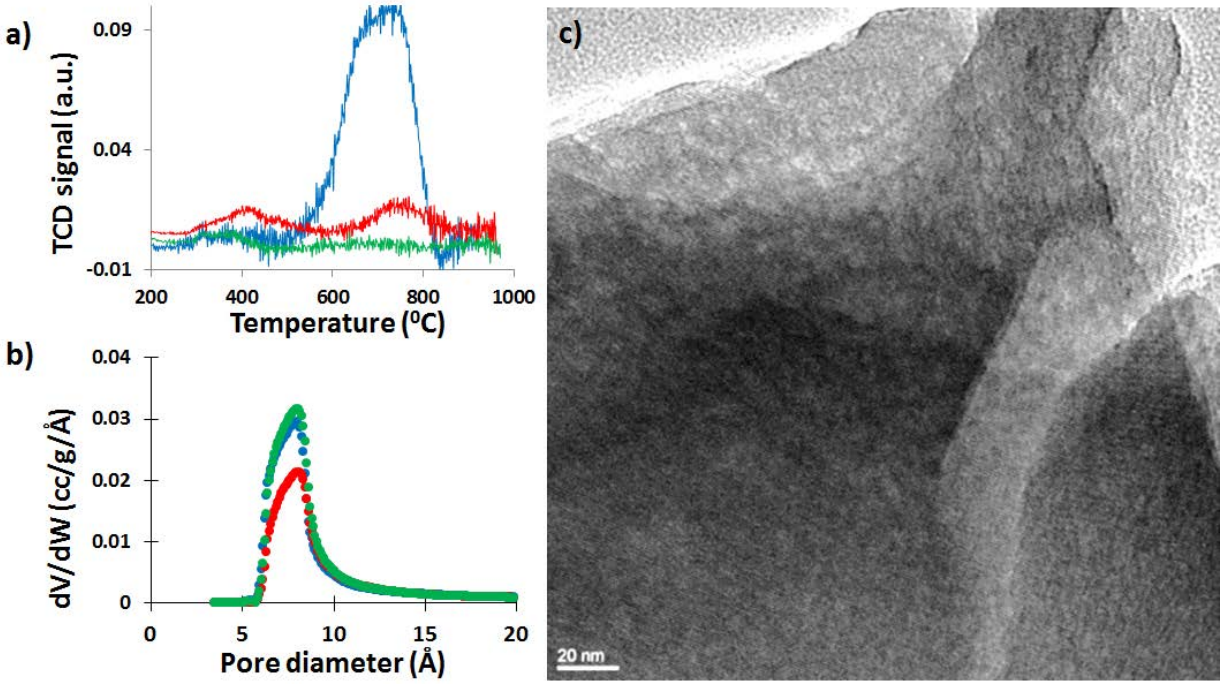

Figure 29. Ex-situ characterization of ZnO@HZSM-5: a) H2-TPR, b) micropore size distribution, and c) HRTEM image after 4th reaction cycle. Before reaction (blue), after 1st reaction cycle (red), and after 4th reaction cycle (green).

ZnO@HZSM-5. As expected from the synthesis path, and confirmed via HRTEM, NH_3-TPD, and H_2-TPR, the core-shell catalyst prepared by direct embedding of ZnO NPs in HZSM-5 contains only monodisperse 6 nm ZnO NPs which are too large to fit into the zeolite micropores and hence get embedded into newly formed mesopores in the zeolite[142]. The ZnO NPs are reducible and hence not stable at the reaction condition. Nevertheless, this catalyst shows a surprisingly high benzene selectivity, close to that of Zn/HZSM-5-24 (max: 64% vs 72%), despite the absence of small ZnO nanoclusters in the zeolite micropores.

This somewhat unexpected behavior was further investigated via characterization of the catalyst before reaction and after various reaction/regeneration cycles (figure 29). H_2-TPR (fig. 29a) show that the fresh ZnO@HZSM-5 sample contains reducible ZnO NPs as indicated by the

broad peak between 600-700 ^{0}C (blue curve). The amount of reducible ZnO decreases strongly after the first reaction/regeneration cycle and is almost entirely gone after the fourth cycle, as expected due to evaporation of reduced Zn during the reaction cycles. The loss of ZnO NPs from this sample is clearly seen in TEM (fig. 29c), where a "Swiss cheese" like zeolite morphology is clearly visible, characterized by a dense distribution of hole with ~6nm diameter, clearly left behind by the reduced and evaporated ZnO NPs.

However, in parallel to the loss of the high-temperature peak, a new peak appears after the first reaction/regeneration cycle at about 400 ^{0}C. This peak was previously shown to be associated with Zn species in the zeolite micropores (cp. figure 22A). Hence, this suggests that some Zn, rather than evaporating out of the zeolite, might (temporarily) deposit in the zeolite micropores during the elution from the zeolite structure. After 4 cycles, however, this peak disappears. This is in fact confirmed via a micropore analysis of the catalyst (fig. 29b): The as synthesized catalyst shows the presence of micropores with a size centered at ~8A, corresponding to the ZSM-5 micropores. After the 1st reaction cycle, the pore volume of these micropores decreases significantly, suggesting pore blocking by newly formed intra-pore Zn clusters. After the 4th reaction/regeneration cycle, however, the original pore size distribution is recovered, indicating essentially complete loss of these clusters from the pores.

ZnO/HZSM-5. Finally, the wet impregnation catalyst shows evidence of a very broad distribution of Zn species, as expected from wet impregnation which is one of the most common and simplest approaches to disperse metal in zeolites (and other catalysts), but typically results in comparatively poorly defined materials. This catalyst shows a combination of the features observed with the other three catalysts. However, one could expect that a more careful investigation of optimal conditions for wet impregnation could allow a more controlled

distribution of Zn species in this catalyst. However, as the main conclusion of the present investigation is the unstable nature of the active metallic Zn species, the present reaction system does not warrant such a more in-depth study.

4.3 SUMMARY AND CONCLUSION

The present study aimed to investigate the nature of the active species in Zn-containing HZSM-5 catalysts by preparing Zn-HZSM-5 via three different synthetic approaches: wet ion exchange, wet impregnation, and core-shell synthesis. By investigating the impact of the preparation methods on the distribution of Zn species, and studying the catalytic performance of the resulting materials in DHA—including their deactivation behavior—clear structure-activity correlations could be derived.

Our results show that ion exchange initially results in the formation of Zn^{+2} at the exchange sites and, at longer exchange times, in the formation of ZnO nanoclusters inside the zeolite micropores. In contrast, a core-shell synthesis approach allowed direct encapsulation of size-controlled, pre-made ZnO NPs throughout HZSM-5. Finally, wet impregnation results in a highly heterogeneous distribution of Zn species, ranging from Zn species inside the micropores to large ZnO particles on the external zeolite surface.

All catalysts show a transition in reactivity with time, starting with strong initial CO_2 formation, followed by selective benzene formation, and finally production of C2 species. The initial CO_2 formation indicates reduction of ZnO and hence also the fact that it is metallic Zn that is the active species for the subsequent benzene formation. This initial reduction results in a significant induction period before the catalyst shows aromatization activity. Comparison

between the two ion exchange catalysts leads to the identification of the most active and the most stable zinc species: Reduced Zn^0 nanoclusters inside the zeolite micropore constitute the most active species. However, like all reduced Zn species, they get irreversible lost from the catalyst via evaporation at the high-temperature conditions of DHA. In contrast, Zn^{2+} anchored at the exchange sites of zeolite are the most stable species, but provide little to no aromatization activity. Interestingly, by correlating the activity data with ex-situ characterization, we observed that the core-shell catalyst forms in-situ active Zn nanoclusters within the zeolite micropores during the evaporation of the Zn. As a result, this catalyst which originally contains only 6nm ZnO NPs shows transiently high aromatization activity.

Overall, our study hence gave significant insights into the active species in Zn-HZSM-5 catalysts, but the ultimate conclusion is that it appears inherently impossible to synthesize a stable Zn-based zeolite catalyst for DHA due to the reducing reaction conditions and the very high vapor pressure of Zn. However, alloying of metals is well-known to improve their physical and chemical stability[147] and could possibly offer a route for stabilization of Zn, although the impact of such alloying on catalytic activity would require further investigation.

5.0 FE-HZSM5 CATALYSTS FOR METHANE DEHYDROAROMATIZATION

Benzene is one of the most important organic intermediates in the petrochemical industry, and is currently produced almost exclusively from crude oil processing. Increased availability of shale gas has resulted in significantly lower price for natural gas than oil[148]. As a result, there is renewed interest in the development of a process that directly converts methane to benzene. Non-oxidative methane dehydroaromatization (DHA) can achieve this with reported methane conversions of up to ~10% X_{CH4} and benzene selectivity of up to ~80% over bi-functional Mo/HZSM-5 (catalysts) at a typical reaction temperature of 700 °C [2]. Over this catalyst, methane is activated on Mo sites (in their active form as oxicarbide clusters) and the generated methyl radicals oligomerize on Bronsted acid sites (BAS) of HZSM-5 to form benzene. High benzene selectivity is attributed to the shape selectivity of ZSM5 micropores [15-16].

However, the utility of Mo/HZSM-5 catalyst for DHA is severely limited due to coking, which deactivates the catalyst. Regeneration is typically conducted via coke burn-off in an oxidative environment[15]. However, this burn-off also results in oxidation of the Mo species, which hence requires re-activation (typically ~0.5-1 hours) to convert it back into the active oxycarbide form[131]. Mo-HZSM-5 catalysts typically require regeneration every ~5 hours (somewhat depending on reaction conditions[13]). Both the frequent required regeneration and the repeated re-activation periods pose significant barriers to economic viability of the DHA process. While the existing literature for DHA predominantly focuses on Mo/HZSM5 catalysts, the above issues[31, 149] motivate the search for alternative metals that are stable and can also efficiently activate methane for oligomerization to benzene[94, 129, 150].

Iron has in recent years attracted increasing attention as an attractive catalyst due to its earth abundance, low cost, and low toxicity[151-152]. Recent work by Bao *et al.*[153] confirmed the well-established potential of Fe as a C-C coupling catalyst; however, they also demonstrated the propensity of Fe to result in extensive coke formation. Intriguingly, they demonstrated that atomically dispersed Fe (on silica) results in the formation of methyl radicals without coke formation, which then undergoes C-C coupling in the gas phase at the high temperatures of their reaction conditions.

Based on these reports, we hypothesized in the present work that atomically dispersed Fe in HZSM-5 micropores will result in: (i) a selective Fe-HZSM5 catalyst for DHA by taking advantage of the catalytic activity of Fe and the shape selectivity of the zeolite, and (ii) much reduced coke formation compared to catalysts with larger Fe nanoparticles in HZSM-5. Although there have been previous reports on Fe-HZSM-5 catalysts[3, 93] as well as Fe-doped Mo/HZSM-5[89, 95], no systematic investigation and detailed discussion of the active Fe species in these catalysts has been reported to-date.

Different forms of iron have been identified in Fe-HZSM-5 (figure 30)[142, 154]. These include isolated ions either (a) in framework positions or (b) at the exchange sites of zeolite, (c) bi- and oligonuclear iron complexes in extraframework positions, (d) iron oxide Fe_xO_y nanoclusters of size ≤ 0.55 nm, and large iron oxide nanoparticles (Fe_2O_3) either (e) located at the surface of the zeolite crystal or (f) embedded between the zeolite crystallites. In the present study, we investigated the effects of different forms of Fe species on the catalytic performance of Fe-HZSM-5 in DHA. The catalysts were prepared via three different approaches to create different Fe species in HZSM-5.These carriers were then characterized by XRD, HRTEM, H_2-TPR, and UV/vis spectroscopy to determine the nature and distribution of Fe species in the obtained catalysts. This approach allows us to demonstrate that both benzene selectivity and coke selectivity are directly related to the Fe dispersion.

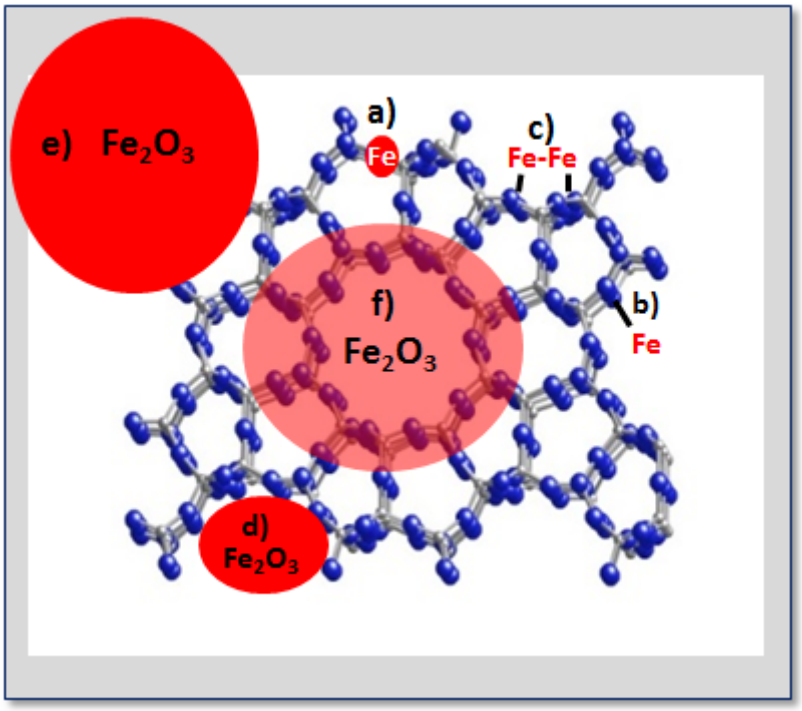

Figure 30. Schematic representation of the different Fe species identified in Fe-HZSM-5.

5.1 EXPERIMENTAL

5.1.1 Materials and methods

H-(Fe)ZSM-5 (Isomorphous substitution). H-(Fe)ZSM-5 was synthesized by an isomorphous substitution route[154]. Typically, a mixture of $Fe(NO_3)_3$ (99.99%, Sigma Aldrich) and $Al(NO_3)_3$ (>98%, Sigma Aldrich) was first prepared. Tetraethoxysilane (TEOS) was added dropwise to the above mixture and stirred for 1 h. A premade mixture of structure directing agent (SDA) Tetrapropylammonium Hydroxide (TPAOH, 20 wt % in aqueous solution) and NaOH was then added dropwise and formed a transparent gel with molar ratios between the components as

H_2O/Si=45, TPAOH/Si=0.1, NaOH/Si=0.2, Si/Al=38, and Si/Fe=152. The gel was then sealed in a Teflon-lined stainless steel autoclave and underwent hydrothermal treatment at 175 ^{0}C for 5 days. The product (Na-(Fe)ZSM-5) was washed with deionized (DI) water and dried at 100 ^{0}C, followed by calcination at 550 ^{0}C in air for 5 h. Next, Na-(Fe)ZSM-5 was converted to H-(Fe)ZSM-5 by ion exchange with aqueous NH_4NO_3 solution (1M) at 80 ^{0}C for 12 h. Finally, the material was dried at 100 ^{0}C in vacuum and calcined at 500 ^{0}C in air for 5 h.

Fe/HZSM-5 (Wet ion exchange). The parent ZSM-5 zeolite was first synthesized by a hydrothermal synthesis. The molar composition used for the synthesis is: Al_2O_3 : 80SiO_2 : 36TPAOH : 5Na_2O : 4280H_2O, from the mixture of sodium hydroxide (NaOH), silica nanoparticles (100-300 nm), sodium alumina ($NaAlO_2$), and tetrapropylammonium hydroxide (TPAOH, 20 wt % in aqueous solution). Crystallization was conducted at 180 ^{0}C for 48 h in a Teflon-lined stainless steel autoclave. The solid product was recovered by centrifugation and washing with DI water (4 times), followed by drying at 100 ^{0}C overnight and calcination at 550 ^{0}C for 6 h in air. As-synthesized NaZSM-5 was converted to HZSM-5 by ion exchange with aqueous NH_4NO_3 solution (1M) at 80 ^{0}C for 12 h and subsequent drying at 100 ^{0}C and calcination at 500 ^{0}C for 5 h. Iron was then introduced to the HZSM-5 via wet-chemical ion exchange (HZSM-5 in $Fe(NO_3)_3$ aqueous solution at 80 ^{0}C for 6 h). The product was then washed with DI water and dried at 100 ^{0}C overnight, followed by calcination at 500 ^{0}C for 20 h.

Fe_2O_3@HZSM-5 (Core shell synthesis). Fe@ZSM-5 was prepared by a bottom-up synthesis route[142]: (i) synthesis of Fe@silica; (ii) conversion of amorphous silica in Fe@silica to ZSM-5 crystal via hydrothermal treatment . Fe@silica material was directly synthesized in a reverse-microemulsion mediated sol-gel process [117]. Typically, a mixture of 20 g Brij58 (> 99 %, Sigma-Aldrich) and 60 mL cyclohexane was heated to 50 ^{0}C in oil bath under stirring. The iron

nitrate aqueous solution was added dropwise. Under stirring, ammonium hydroxide solution (28 wt%) was added dropwise to the previous solution. Next, 5 g TEOS was added dropwise to the microemulsion. Hydrolysis and condensation of the silica precursors proceeded for 2 h at 50 °C. The product was washed and dried at room temperature and then calcined at 500 ^{0}C to remove any remaining surfactant. The conversion of Fe@silica into Fe@ZSM-5 was conducted at the same hydrothermal conditions used for above NaZSM-5 protocol. Finally, converting the synthesized Fe@ZSM-5 to H-form ZSM-5 was achieved by ion exchange with aqueous NH_4NO_3 solution (1 M) at 80 ^{0}C for 12h and subsequent drying at 100 ^{0}C and calcination at 500 ^{0}C for 5 h.

5.1.2 Catalyst characterization

X-ray diffraction (XRD). Powder X-ray diffraction (XRD) measurements were performed with a high-resolution powder X-ray diffractometer (Bruker D8 Discover) using a monochromatic Cu radiation at the wavelength of 1.54 Å. The beam voltage was 40 kV at a current of 40 mA. The diffraction patterns were recorded with a step of 0.02 ^{0} (2θ), 0.5 sec/step.

Electron microscopy and X-ray microanalysis. JEOL JSM-6510LV field emission scanning electron microscope (SEM) was used to determine material morphology at beam voltage of 20 kV. Samples were sputter coated with a thin palladium film prior to characterization. Nanoscale morphology was determined by a high-resolution transmission electron microscopy (HRTEM, JEOL-2100). Samples were dispersed on a copper type-B support grid (Ted Pella Inc.). The chemical composition of Zn-HZSM-5 catalysts was determined by energy dispersive analysis of X-ray (EDX) equipped on SEM (JEOL JSM6510LV), with a collection time of 240-300 s.

Temperature programmed reduction (H_2-TPR). H_2-TPR was operated with a Micromeritics Chemisorb 2750 system equipped with a thermal conductivity detector. During the TPR analysis, the samples were first oxidized in 5% O_2/He at 500 °C for 1 h, and then TPR was performed by heating the sample (100 mg) at 10 °C/min to 1000 °C in a 10% H_2/Ar flow (20 ml/min). A cold trap filled with acetone-dry ice mixture was placed between reactor and TCD to remove water vapor.

UV/vis Diffuse Reflectance Spectroscopy (DRS). UV/vis-DRS measurements were performed with Craic QDI 2010 UV-Visible-NIR Microspectrophotometer equipped with a diffuse reflectance accessory. To reduce light absorption, samples were diluted with barium at a ratio of 1:3. The background peak from the instrument was removed by subtracting a spectrum with a blank-run spectrum.

5.1.3 Reactivity evaluation

Methane dehydroaromatization was carried out in a fixed-bed reactor at 700 ^{0}C and atmospheric pressure. Typically, catalysts were charged into a 5.0 mm i.d. quartz tubular reactor. The reactor tube was heated from room temperature up to 500 ^{0}C for catalyst pretreatment in air, and then heated to reaction temperature (700 ^{0}C) under helium flow. After temperature equilibration, methane was flowed over the catalyst. The gas hourly space velocity (GHSV) was 3750 (cc/g/hr) for catalytic performance comparison. The effluent gas products were analyzed by both mass spectrometry (MS; Pfeiffer Omnistar QMS 200) and gas chromatography (Agilent 3000A Micro GC equipped with thermal conductivity detectors). 50% He was added to the methane feed as an internal standard. Methane conversion and product selectivity were evaluated based on the carbon mass balance. Total coke formation was determined based on CO and CO_2 signal detected in MS during oxidative regeneration of the spent catalysts.

5.2 RESULTS AND DISCUSSION

5.2.1 Material characterization

In order to allow structure-reactivity correlations and thus evaluate the reactivity and selectivity of different Fe species in the iron/zeolite catalysts synthesized via the three synthesis routes described above, a careful characterization is necessary to identify the species present in these samples. Table 4 shows the chemical compositions of Fe-HZSM-5 catalysts prepared by the three synthesis routes described above. EDX measurements indicate that all three synthesis

routes produced a similar ratio of Si to Al (= 30-33). However, the Fe weight loadings vary strongly due to the different preparation routes from 0.73 wt% of iron in H-(Fe)ZSM-5, over 0.95 wt% of iron in Fe/HZSM-5, to 6.0 wt% of iron in Fe@HZSM-5.

Table 4. Chemical composition of the catalysts used in this study, as determined by EDX.

Catalyst	Prep. method	Si/Al	Fe (wt%)
H-(Fe)ZSM5	Isomorphous substitution	33	0.73
Fe/HZSM5	Wet ion exchange	30	0.95
Fe@HZSM5	Core-shell synthesis	32	6.0
HZSM5	--	31	- -

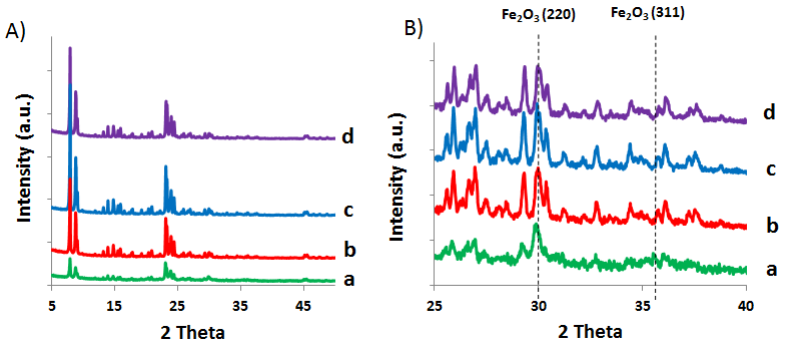

Figure 31. A) XRD pattern for a) Fe@HZSM-5, b) Fe/HZSM-5, c) H-(Fe)ZSM-5, and d) parent HZSM-5; B) Expanded view of A for 2 theta 25- 40 ^{0}.

Fe-containing HZSM-5 prepared by all three methods exhibit qualitatively identical XRD diffraction patterns (figure 31A), indicating successful formation of the MFI zeolite structure in all catalysts. The dominant diffraction peaks of Fe_2O_3 are $Fe_2O_3(220)$ and $Fe_2O_3(311)$. However, the peaks of ZSM-5 around $Fe_2O_3(311)$ are very complex and hence they make $Fe_2O_3(311)$ very

difficult to analyze. Moreover, we found that the XRD diffraction pattern of ZSM-5 has a peak that overlaps with the peak indicative of Fe_2O_3(220). We therefore identified Fe_2O_3 in the catalysts by comparing the intensity of Fe_2O_3(220) peak (~30 ^{0}) with that of the neighboring peak (~29 ^{0}) of HZSM-5. Figure 31B shows that only Fe@HZSM-5 (curve a) shows a distinct Fe_2O_3(220) peak. This suggests that a significant amount of Fe_2O_3 particles with sizes that are large enough to be picked up by XRD (>2 nm) only exists in Fe@HZSM-5, while in the other two catalysts Fe species are well dispersed in the HZSM-5.

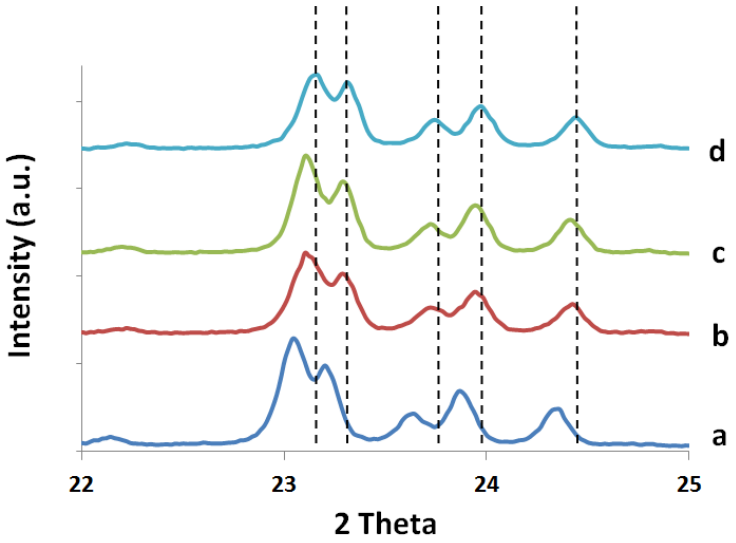

Figure 32. XRD pattern of the (Fe)ZSM-5 catalyst and HZSM-5: a) As synthesized Na-(Fe)ZSM-5, b) Na-(Fe)ZSM-5 after calcination at 550 ^{0}C to remove SAD, c) H-(Fe)ZSM-5, and d) HZSM-5. The dashed lines indicate the diffractions of the reference HZSM-5.

For the H-(Fe)ZSM-5—prepared via isomorphous substitution during which Fe atoms occupy some T-sites (i.e. Si or Al sites) of the ZSM-5—XRD can be used to trace the locations of the dopant iron throughout the three stages of catalyst preparation, i.e. as-synthesized Na-

(Fe)ZSM-5, after calcination to remove the structure-directing agent (TPAOH), and after ion-exchange from Na-(Fe)ZSM-5 to H-(Fe)ZSM-5). Using HZSM-5 with similar Si/Al as a reference, figure 32 shows that the Na-(Fe)ZSM-5 diffraction peaks (curve a) are significantly right-shifted after the first calcination (curve b), moving closer those of pure HZSM-5 (curve d). This shift of the diffraction peaks can be attributed to the removal of Fe atoms from the ZSM-5 framework (as Fe has a larger atomic radius than Si). This is hence likely a result of some iron bleeding out of the ZSM-5 framework during calcination, as previously reported for heat treatment of isomorphous substituted (Fe)ZSM-5[155-156]. The subsequent ion exchange results in no further significant shift in peak locations between the heat treated Na-(Fe)ZSM-5 (curve b) and the H-(Fe)ZSM-5 (curve c), suggesting no or very little iron bleed-out during ion-exchange. Finally, comparing H-(Fe)ZSM-5 (curve c) with the reference H-ZSM-5 (curve d), the shifted peak positions indicate that a significant fraction of atomically dispersed Fe remains in the zeolite framework, i.e. that in this catalyst Fe co-exists both within the zeolite framework and as (bled-out) extra-framework species.

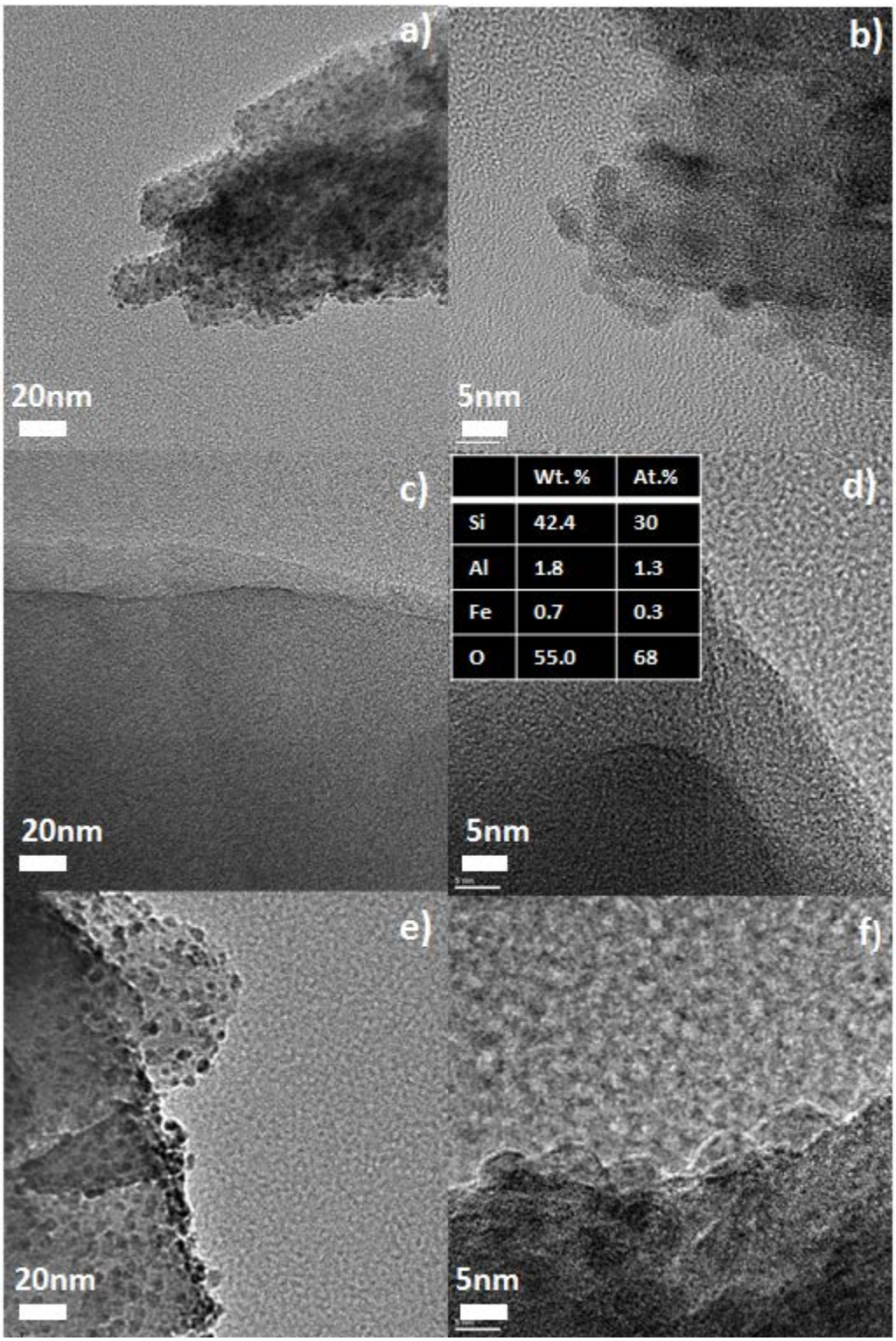

	Wt. %	At.%
Si	42.4	30
Al	1.8	1.3
Fe	0.7	0.3
O	55.0	68

Figure 33. TEM images for the three Fe-HZSM5 catalysts prepared by different methods: (a,b) Fe@HZSM5, (c,d) H-(Fe)ZSM5, and (e,f) Fe/HZSM5. The inset table in d) represents the chemical composition of the corresponding TEM image.

The presence of Fe_2O_3 NPs in the zeolite catalysts prepared via the three different methods was investigated by HRTEM (figure 33). No visible nanoparticles (NPs) can be seen in the TEM of the H-(Fe)ZSM-5 catalyst, although a corresponding EDX confirms an Fe content matching the expected Fe loading (see figure 33c, d). In contrast, visible Fe_2O_3 NPs are present both in Fe@HZSM5 (figure 33a, b) and Fe/HZSM5 catalysts (figure 33e, f). The visible color of each catalyst supports this observations: samples with NPs are orange (a darker coloring of Fe@HZSM-5 suggests more particles in this catalysts than in Fe/HZSM-5) while the H-(Fe)ZSM-5 catalyst is white (figure 34). Thus, combining TEM analysis with the above XRD analysis, we conclude that the H-(Fe)ZSM-5 catalyst contains only highly dispersed Fe while Fe@HZSM-5 contains a significant amount of Fe_2O_3 NPs. Since there are no detectable Fe_2O_3 reflections in the XRD pattern of the Fe/HZSM-5 catalyst, the Fe_2O_3 NPs observed in the TEM images are likely only a minor group of its Fe species.

Figure 34. A picture for the three catalysts: Fe@HZSM-5 (left), Fe/HZSM-5 (middle), and H-(Fe)ZSM-5 (right).

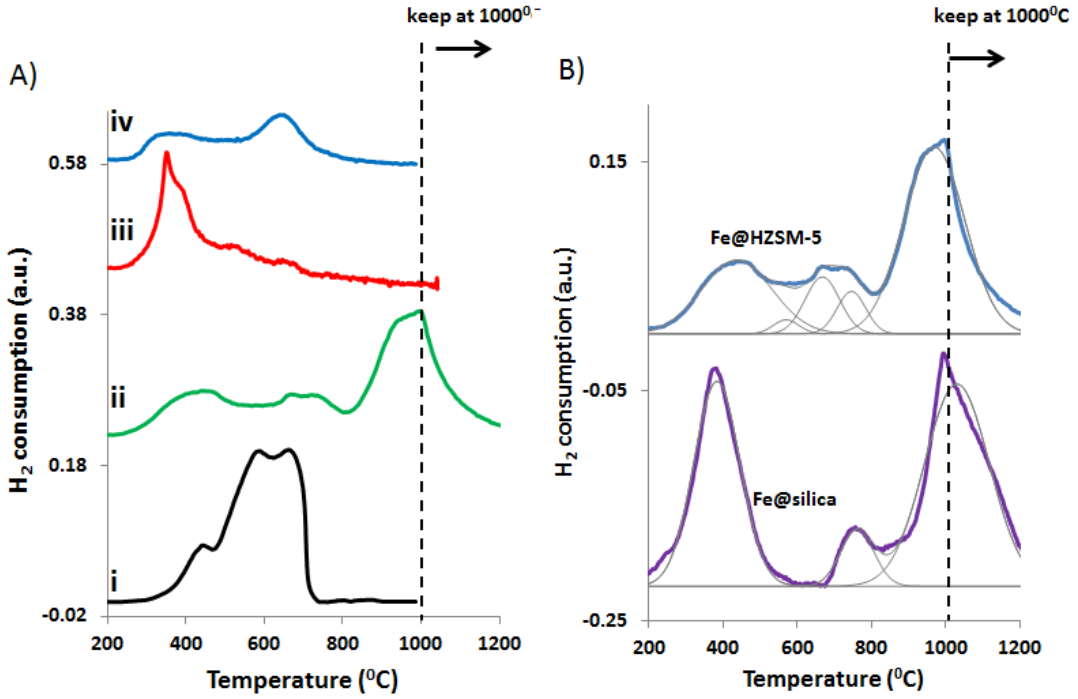

Figure 35. A) H_2-TPR spectra for i) Fe_2O_3 NPs, ii) Fe@HZSM-5, iii) Fe/HZSM5 and iv) H-(Fe)ZSM-5; B) H_2-TPR comparison between Fe@HZSM-5 and its precursor "Fe@silica". Heating rate: 10 K/min in 5% H_2 (balanced with He).

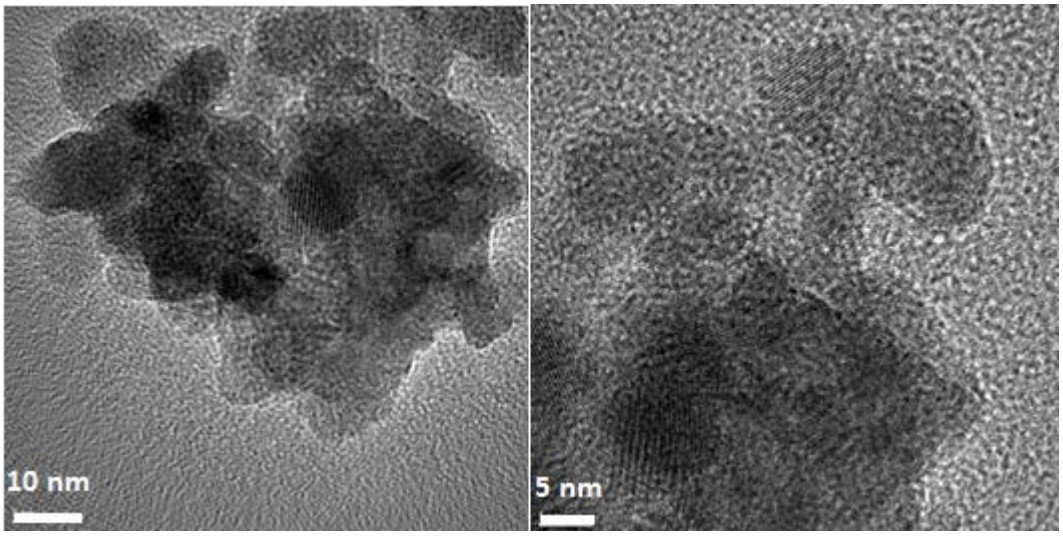

Figure 36. TEM for commercial Fe_2O_3 NPs.

Table 5. H_2/Fe consumption derived from TPR spectra. CuO was used for calibration. Theoretically, H_2/Fe=0.5 indicates reduction of Fe^{+3} to Fe^{+2}, while H_2/Fe=1.5 indicates reduction of Fe^{+3} to Fe^0

Catalyst	H_2/Fe (mol/mol)
H-(Fe)ZSM5	0.54
Fe/HZSM5	0.66
Fe@HZSM5	1.60
Fe_2O_3	1.36

To further distinguish different Fe species, H_2-TPR was conducted for all three catalysts. Figure 35A shows H_2-TPR profiles of the three Fe-containing HZSM-5 catalysts in comparison to that of commercial Fe_2O_3 NPs (with particle size ≈ 10 nm, figure 36). Table 5 summarizes the molar H_2/Fe ratios in these experiments, i.e. the amount of H_2 consumed during reduction of the fully oxidized sample per Fe content of the sample. The commercial Fe_2O_3 TPR profile shows multiple maxima, centered at 430 ^{0}C, 580 ^{0}C, and 680 ^{0}C, resepectively (Figure 35A). The three peaks can be correlated with the reduction of the samples between the different oxidation states of iron, i.e. the low-temperature peak (430 ^{0}C) is ascribed to the reduction of Fe_2O_3 to Fe_3O_4, the middle-temperature (580 ^{0}C) reflects the reduction of Fe_3O_4 to FeO, and the high temperature peak (700 ^{0}C) corresponds to the reductions of FeO to metallic Fe[157]. A H_2/Fe ratio of 1.36, close to the stoichimetrically required ratio of 1.5 for the complete reduction via ½ Fe_2O_3 + 1.5 H_2 = Fe + 1.5 H_2O, confirms the total reduction of Fe_2O_3 to Fe^0 during the TPR experiment. (The fact that the value is slightly below the expected 1.5 might indicate difficulties of completely reducing the iron oxide particles, possibly due to their relatively large particle size and corresponding diffusion limitations in reducing the particle core.)

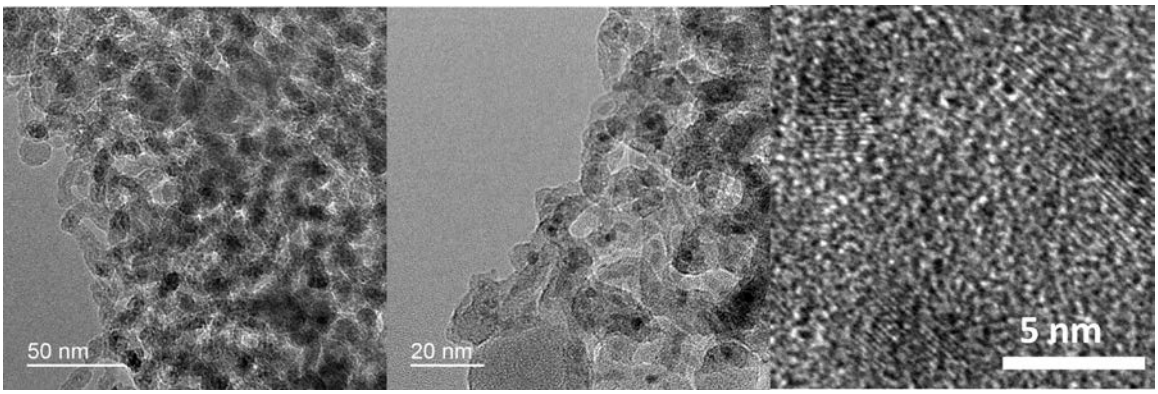

Figure 37. TEM images with different magnifications for the precursor of Fe@HZSM-5 catalyst "Fe@silica". While the structure of the silica matrix is fundamentally different from that of the HZSM-5 zeolite, the embedded Fe NPs are identical to those after conversion.

The Fe@HZSM5 TPR profile has reduction peaks at the same temperatures as that of the commercial Fe_2O_3, for temperatures <700 ^{0}C. This might suggest that Fe_2O_3 NPs on the external surface (observed with TEM, see figure 33), which are expected to have weak interaction with zeolite and behave similarly to bare Fe_2O_3 particles, contribute to the low-temperature reduction peaks. New peaks appear, however, at temperatures >700^{0}C. In order to further elucidate the origin of these peaks, H_2-TPR was also conducted for the Fe@silica precursor material from which the Fe@HZSM-5 is obtained via hydrothermal conversion. TEM of the Fe@silica precursor (figure 37) confirms that this materials contains 3-5 nm Fe_2O_3 NPs embedded in silica, as expected from the synthetic approach, i.e. that the Fe species are not affected by the hydrothermal conversion process. However, unlike Fe@HZSM-5, all Fe NPs are fully encapsulated in the Fe@SiO_2 samples, i.e. there are no exposed NPs on the external surface of the sample.

Figure 35B compares the TPR spectrum this precursor (i.e. Fe@silica) with that of Fe@HZSM-5. The main features in the spectra agree except for the strong reduction of the peak

intensities for the precursor sample in the ~500-700^{0}C temperature range. Since comparison with the bare Fe_2O_3 sample suggests that these peaks originate from unencapsulated Fe_2O_3, this suggests that there are very few Fe_2O_3 particles on the external silica surface, in agreement with TEM (fig. 37). More importantly, it suggests that the high temperature reduction peaks (T>700 ^{0}C), which are absent from the TPR spectrum of bare Fe_2O_3 NPs, is indeed from the encapsulated Fe_2O_3 NPs. The high temperature of these reduction peaks can be traced back to strong interactions of encapsulated Fe_2O_3 particles with the support[158]. This hence confirms that a significant fraction of Fe_2O_3 NPs is successfully encapsulated within the zeolite during the transformation of Fe@silica to Fe@ZSM-5; since these particles are too large to fit into the zeolite micropores, they result in the formation of mesoporosity[142]. In addition, the H_2/Fe ratio of 1.6 (table 5) indicates that all Fe species are fully reducible to metallic Fe. In contrast, Fe located at the cationic exchange sites or framework of the zeolite, Fe^{+3} can only be partially reduced to Fe^{+2} [158-159]. The H_2/Fe ratio hence excludes the presence of such partially reducible species and allows us to conclude that Fe_2O_3 NPs, both on the external surface and within the zeolite structure, are the only Fe species in this catalyst.

The TPR spectrum for Fe/HZSM5 has a main peak at 350 ^{0}C with a shoulder at 400 ^{0}C and two very weak peaks in the 400-700 ^{0}C temperature range (figure 35A, curve ii). The main peak at 350 ^{0}C is attributed to the partially reducible Fe species from Fe^{+3}->Fe^{+2} at the exchange site, as previously reported[160]. The position of the shoulders and the weaker peaks again agree with those of the bare Fe_2O_3, indicating the existence of Fe_2O_3 particles on the catalysts external surface, in agreement with the TEM results (figure 33e,f). The small left-shift (i.e. towards lower temperatures) of all reduction peaks compared to those of commercial Fe_2O_3 could be due to differences in particle size. Furthermore, the H_2/Fe ratio is ~0.66 (table 5), i.e. close to the

stoichiometrically required ratio of 0.5 for the reduction of Fe^{3+} to Fe^{2+} ($Fe_2O_3 + H_2 = 2\ FeO + H_2O$). From the "excess" consumption of H_2, we can estimate that fully reducible Fe_2O_3 NPs (on the external surface) account only for 10-20% of the total Fe species. Overall, the TPR results hence not only confirm that Fe_2O_3 NPs are a minor species in this catalyst, but also indicates that the majority of Fe species are located at the exchange site of zeolite.

Different from the other two iron/zeolite catalysts, the H_2-TPR profile of H-(Fe)ZSM5 shows only two broad maxima, centered at 350 ^{0}C and 680 ^{0}C, respectively (figure 35A, curve iv). The lower temperature peak again reflects the reduction of Fe at the cationic exchange site from Fe^{+3} species to Fe^{+2}, as discussed above. Perez-Ramirez et al. previously identified the high temperature peak as originating not from Fe_2O_3 NPs but due to reduction of framework Fe^{+3} to Fe^{+2}.[154] This interpretation is further supported here by the H_2/Fe ratio of ~0.54 (table 5) which agrees with virtually all Fe species only being reducible to Fe^{+2}. Thus, the H_2-TPR suggests that catalysts synthesized via isomorphous substitution contain only highly dispersed Fe species, both at the cationic exchange site and as framework Fe^{+3}.

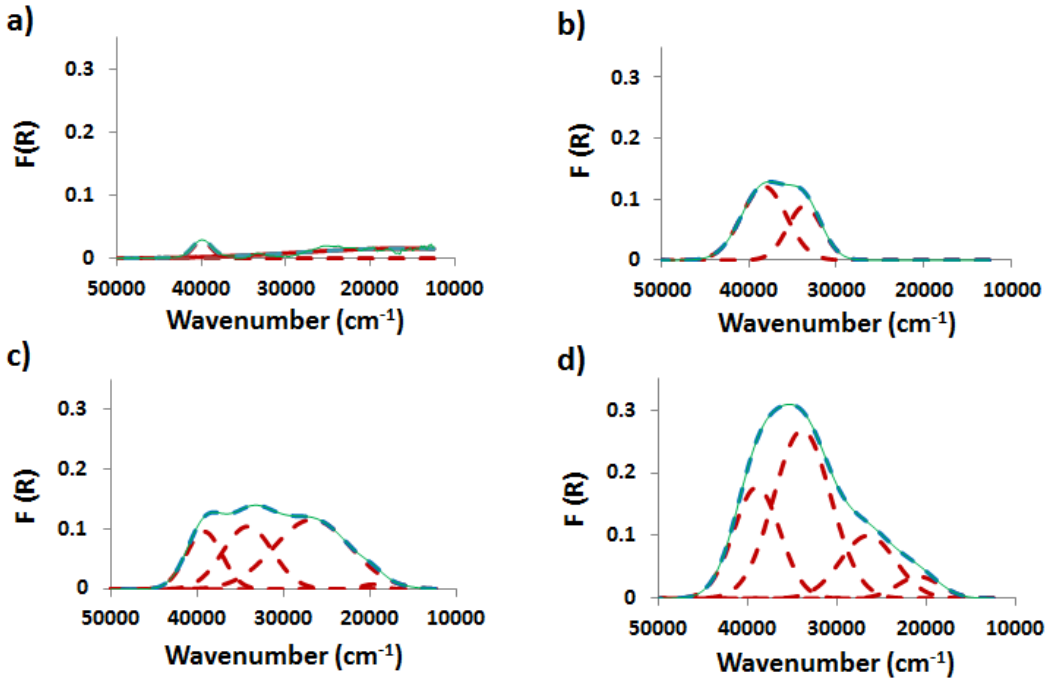

Figure 38. UV/vis spectra for parent HZSM-5 and the three Fe-HZSM-5 catalysts: a) HZSM-5, b) H-(Fe)HZSM-5, c) Fe/HZSM-5, and d) Fe@HZSM-5. (Green line): original curve, (dashed-blue line): fitted curve, and (dashed-brown line): deconvoluted bands.

Finally, UV/vis spectra can yield insights into the nature of Fe species in Fe-zeolite catalysts[161-164], and we thus adopt this technique to further confirm the above conclusions **(**figure 38**)**. Typically, a band below 27,000 cm^{-1} is attributed to Fe_2O_3 particles (~20,000 cm^{-1} for bulk Fe_2O_3 and ~27,000 cm^{-1} for Fe_2O_3 nanoparticles), a band at ~34,000 cm^{-1} is attributed to isolated Fe in octahedral coordination, and a band at ~40,000 cm^{-1} is attributed to isolated Fe in tetrahedral coordination[161-163]. Isolated Fe in an octahedral coordination corresponds to Fe at the exchange site, while Fe in tetrahedral coordination can be Fe at the exchange site or framework Fe.

Spectrum of HZSM-5 shows barely bands (figure 38a), as expected for no Fe in this material. For H-(Fe)ZSM-5, the UV/vis spectrum shows only bands between 30,000-40,000 cm^{-1}

(figure 38b), indicating the existence of isolated Fe. Consistent with the above discussed XRD and H_2-TPR results (cp figure 31 and 35), the isolated Fe species exist both as Fe in the ZSM-5 framework and at the exchange sites. However, the absence of bands from 20,000-30,000 cm^{-1} indicates absence of Fe_2O_3 NPs. This is again consistent with the TEM results (see figure 33c,d). Therefore, the catalyst prepared by isomorphous substitution route results in only atomically dispersed Fe species located within the zeolite (figure 39A).

The catalyst prepared via wet ion exchange, Fe/HZSM-5, shows multiple bands ranging from 20,000-40,000 cm^{-1} (figure 38c). The two bands from 20,000-30,000 cm^{-1} confirm the presence of Fe_2O_3 particles. The majority of the particles are in the nanosize regime indicated by the presence of a much stronger peak at 27,000 cm^{-1} than the peak at 20,000 cm^{-1}, again in agreement with TEM observations (see figure 33e,f). The bands from 30,000-40,000 cm^{-1} are assigned to isolated Fe species. Due to the post-synthetic incorporation of iron (i.e. ion exchange of iron into the parent HZSM-5), these bands can only be from Fe at the exchange sites rather than Fe in the framework of ZSM-5. Thus, UV/vis confirms that the catalyst prepared by wet ion exchange contains some iron oxide NPs on the external surface in addition to atomically dispersed Fe at the exchange sites (figure 39B).

Finally, Fe@HZSM5 shows a plateau from 30,000-40,000 cm^{-1} with a broad shoulder from 20,000-30,000 cm^{-1} (figure 38d). The two bands (within the shoulder) from 20,000-30,000 cm^{-1} are assigned to Fe_2O_3 particles, with most of those again in the nanosize regime as indicated by the much stronger band at 27,000 cm^{-1} than at 20,000 cm^{-1}. This indicates the presence of external NPs in agreement with TEM and TPR observations (figure 33a,b and figure 35). The H_2/Fe ratio in H_2-TPR indicated that all iron species are fully reducible NPs (table 5). Therefore, the plateau from 30,000-40,000 cm^{-1} is again unlikely to stem from partially reducible isolated

Fe species. Instead, the encapsulation of Fe_2O_3 particles within the support may result in a blue shift of Fe_2O_3 bands from 20,000-30,000 cm^{-1} to 30,000-40,000 cm^{-1}. Indeed, Fe_2O_3 NPs confined in mesoporous silica have previously been reported to give rise to bands in UV/vis between 30,000 to 40,000 cm^{-1} [165]. This assignment also agrees with the very high temperature reduction peak (T > 900 ^{0}C) in H_2-TPR profile of our Fe@HZSM-5 sample, resulting from the reduction of Fe_2O_3 NPs encapsulated within ZSM-5. Therefore, these results confirm that Fe@HZSM-5 contains only Fe_2O_3 NPs, both on and within the HZSM-5 structure (figure 39C).

Overall, the different characterization methods (XRD, TEM, H_2-TPR, and UV/vis spectra) yield good agreement in assessing the Fe species in the three catalysts and hence allow assignment of Fe species with good confidence. The results furthermore confirm that the three catalyst preparation methods do indeed result in catalysts with distinctly different distribution of Fe species which hence form the basis for assessing the catalytic activity and selectivity if these species in DHA.

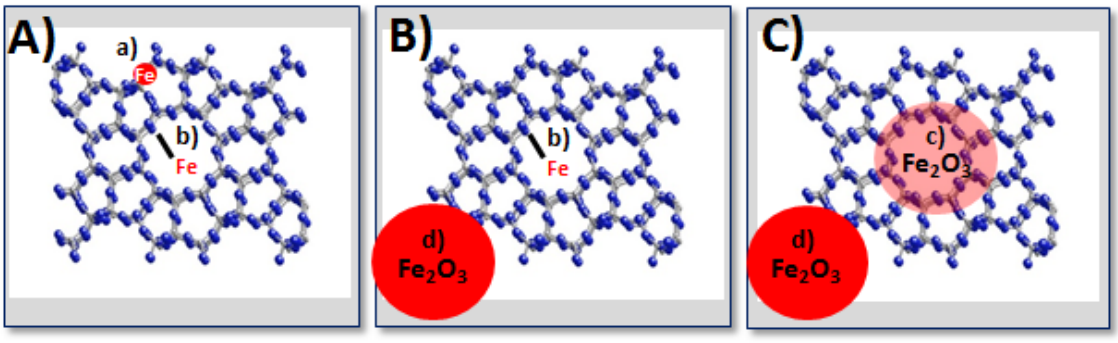

Figure 39. Schematic representation of Fe species in Fe-HZSM-5 prepared by different methods: A) H-(Fe)ZSM-5, B) Fe/HZSM-5, C) Fe@HZSM-5. Different Fe species are Fe in HZSM-5 framework a), Fe at cationic exchange sites b), Fe_2O_3 NPs encapsulated within HZSM-5 c), and Fe_2O_3 NPs on external surface **d).**

5.2.2 Catalytic performance

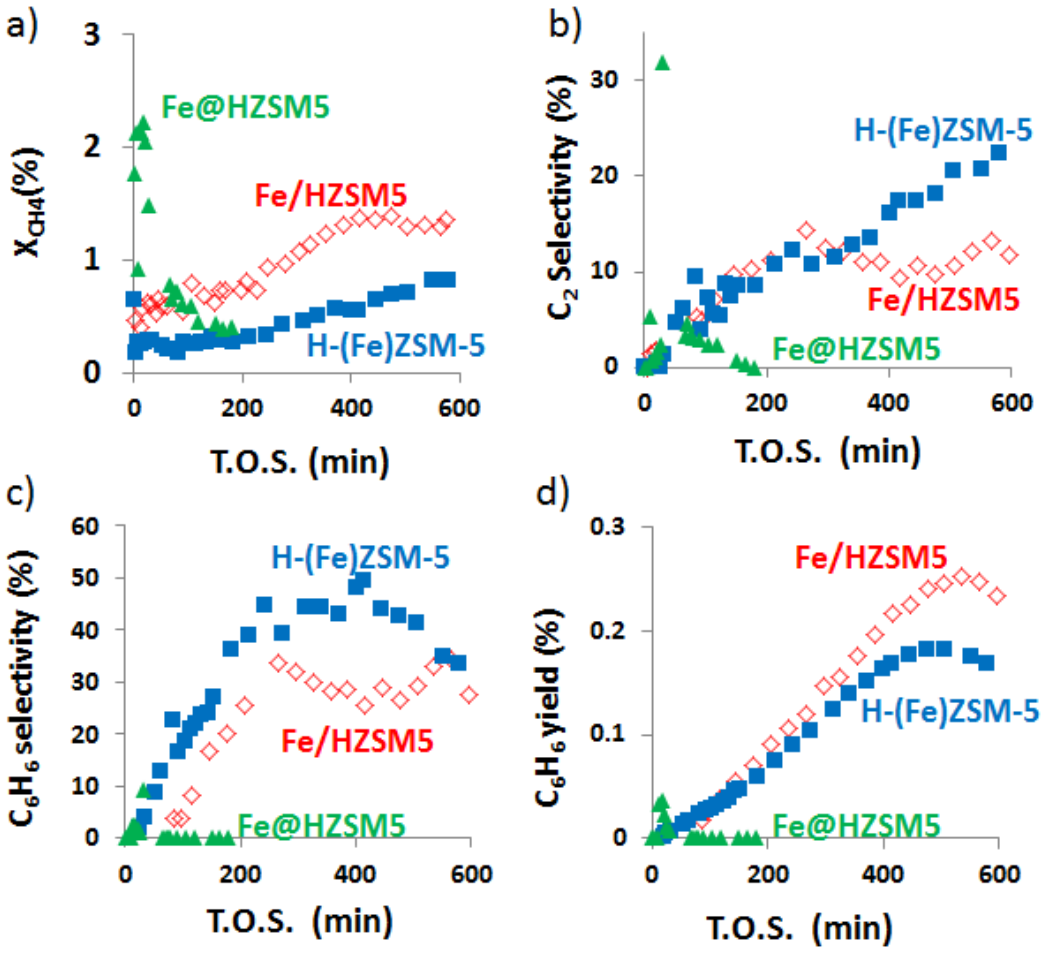

Figure 40. Reactivity data for the three Fe-HZSM5 catalysts at 700 °C: Methane conversion a), C2 selectivity b), benzene selectivity c), and benzene yield d). GHSV: 3750 cc/g/h (50% CH_4 and 50% He).

Following the characterization of the catalysts and identification of the Fe species, the catalytic performance of the three catalysts in DHA is evaluated in order to assess activity/selectivity correlations with the respective Fe species. Figure 40 shows results in terms of methane conversion and product selectivity/yield vs time-on-stream at an (isothermal) reaction

temperature of 700 ^{o}C. Note that no attempt was made at optimizing the respective catalyst performances for DHA, but the study focused instead on a comparative evaluation of the three catalysts at identical conditions, typical for DHA.

Fe@HZSM5 shows a very strong maximum in initial reactivity, well in excess of the other two catalysts, but rapid deactivation and almost no benzene selectivity (with predominantly C_2 products). In contrast, Fe/HZSM5 and H-(Fe)ZSM5 show lower, but sustained activity and improved benzene selectivity. H-(Fe)ZSM-5 benzene selectivity is slightly higher between the latter two catalysts, although benzene yields are lower due to lower activity (i.e. methane conversion).

In the previous section, we demonstrated that (i) H-(Fe)ZSM-5 contains only atomically dispersed Fe, (ii) Fe/HZSM-5 includes predominantly atomically dispersed Fe with a small amount of Fe_2O_3 NPs on the external surface, and (iii) Fe@HZSM-5 contains only Fe_2O_3 NPs embedded within zeolite and on the external surface (figure 39). Comparing catalytic performance with these Fe distributions hence strongly suggests that higher Fe dispersion results in better benzene selectivity (H-(Fe)ZSM-5 > Fe/HZSM5 > Fe@HZSM-5). This corroborates our hypothesis that atomically dispersed Fe within HZSM5 micropores results in a selective Fe-HZSM5 catalyst for DHA, owing to the synergistic effect between the active Fe site, the neighboring BAS, and the zeolite shape selectivity[15-16].

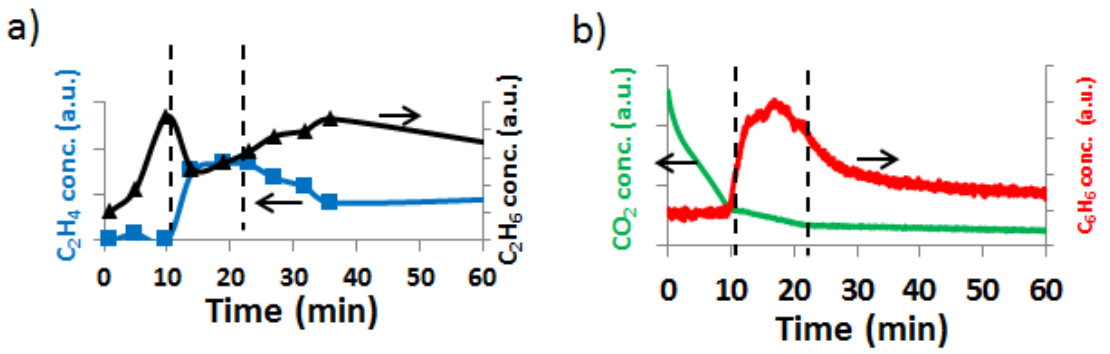

Figure 41. Activity data for the Fe@HZSM5 catalyst at 700 °C (GHSV: 3750 cc/g/h with 50% CH_4 and 50% He): C2 product from GC a) and CO_2 and benzene signal from mass spectrometry. Dashed lines indicate the timing of ex-situ XRD study.

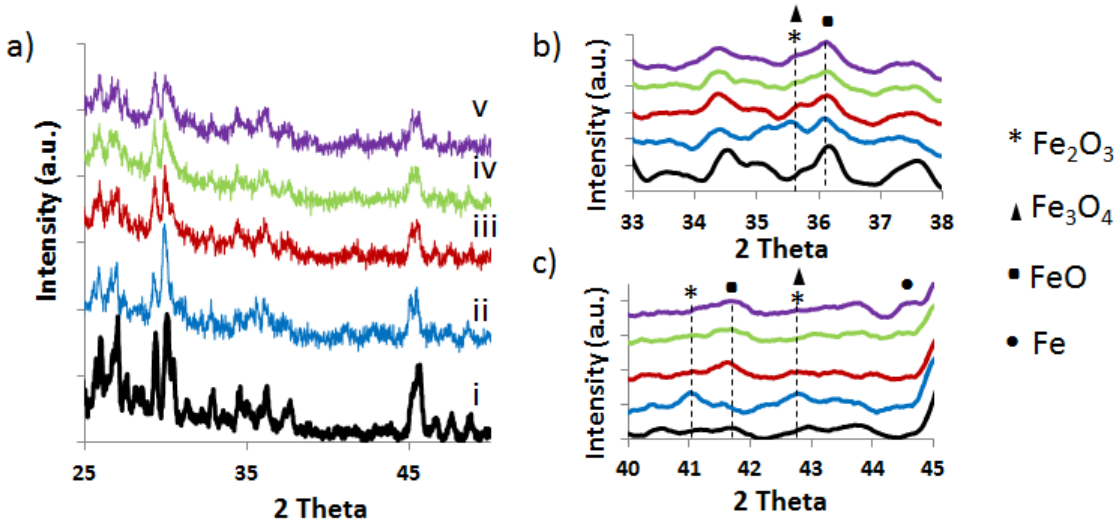

Figure 42. a) Ex-situ XRD for Fe@HZSM5 after different time of reactions. The catalyst before reaction (ii), after 11-min reaction (iii), 23-min reaction (iv), and 180-min reaction (v). HZSM5 (i) here is used as reference; b) and c) are expanded view for 2 theta 33^0-38^0 and 40^0- 45^0, respectively.

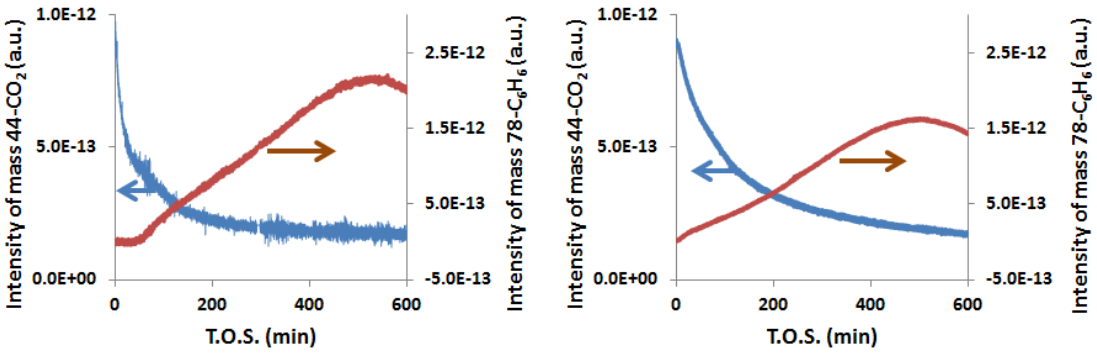

Figure 43. Mass spectroscopy data for the Fe/HZSM5 catalyst (left) and H-(Fe)ZSM-5 catalyst (right) at 700 °C (GHSV: 3750 cc/g/h with 50% CH_4 and 50% He). Since oxygen can only be extracted from the Fe species in the reaction system, CO_2 observed over these two catalysts must result from reduction of Fe species.

The reactivity data shows that Fe@HZSM5 is active only for a very short period. Further examination of the product distribution, shown in figure 41, indicates the formation of different products at different reaction stages: Strong CO_2 formation at the onset of the reaction, followed the formation of C_2H_6 for t < 11 min., transition to production of both C_2H_4 and C_6H_6 predominately between 11- 23 min, and finally again predominantly C_2H_6 formation for t >23 min. H_2-TPR had shown that the Fe_2O_3 in this catalyst can be completely reduced to the metallic state (see table 5), via Fe_2O_3 -> Fe_3O_4 -> FeO -> Fe. One should expect that these different oxidation states of Fe result in different product selectivity, explaining these changes in selectivity. To corroborate this, figure 42 shows ex-situ XRD results for the fresh catalyst and the spent catalyst after 11, 23, and 120 min time-on-stream. Before reaction, the fresh Fe@HZSM-5 shows a distinct intensity of Fe_2O_3(220) (at ~30^0) to that of neighboring peak of ZSM-5 (at ~29^0) as discussed in the characterization section. Furthermore, a small shoulder of Fe_2O_3(311) can be seen at ~35.8^0. Both indicate the presence of Fe_2O_3; no other oxidation phase of Fe is observed. After 11 min of reaction, the intensity of Fe_2O_3(220) decreases strongly. Due to the similar

position (~35.8^0) of Fe_2O_3(311) and Fe_3O_4(311), the almost unchanged peak intensity at this position is very likely from the replacement of Fe_2O_3(311) with Fe_3O_4(311). Meanwhile, a diffraction of FeO(200) at ~41.7^0 shows up. These changes suggest Fe_2O_3 was consumed (reduced) and FeO (Fe_3O_4) became the dominant oxidation states during this period. After 23 min, the Fe_3O_4 (311) diffraction peak disappears and the FeO(200) diffraction peak is reduced in intensity, indicating the disappearance of these two oxidation states. Finally, after 120 min, only a reflection of metallic Fe(110) is seen (in addition to the background peaks of ZSM-5).

Correlating these oxidation states with the corresponding reactivity data suggests that Fe_2O_3, which is present during the first 11 min time-on-stream, is inactive for conversion of methane to benzene and instead predominantly results in the formation of CO_2, i.e. in methane total oxidation. The reaction period between 11-23 min is dominated by Fe_3O_4 and FeO species and corresponds to maximum benzene selectivity, indicating that these two oxidation states are the most active ones for benzene production. Although some benzene selectivity can still be seen after 23 min of reaction, the dominant iron oxidation state is Fe^0, thus indicating that metallic Fe has low DHA activity.

The identification of Fe_3O_4 and FeO as the most active phases for methane aromatization also agrees well with the activity data of the other two catalysts (H-(Fe)HZSM5 and Fe/HZSM5). The maximum benzene selectivity appears after an extensive activation time (figure 40c and figure 43) presumably due to the required reduction of the Fe species to their active state for benzene production. Furthermore, the majority of the Fe species in these two catalysts can be reduced only to Fe^{+2} (as suggested by TPR, see table 5), explaining the sustained good benzene selectivity for these two catalysts.

Table 6. Coking data for the three Fe-HZSM5 catalysts over reaction at 700 ^{0}C. Coke amount was evaluated by regeneration of spent catalysts in 20% O_2 (balanced by Ar). Coke selectivity was then calculated by dividing the coke amount by methane converted over the reaction period. Benzene formation was determined during the entire reaction period. Data is shown for 10-hr time-on-stream with values in parenthesis for 23-min TOS.

Catalyst	Method	Coke (mg/100mg catalyst/wt% Fe)	Coke selectivity (%)	Benzene formation amount (mg)
Fe@HZSM5	Core-shell synthesis	1.31 (0.028)	94.8 (16.2)	0.013 (0.013)
H-(Fe)ZSM5	Isomorphous substitution	1.95	32.8	1.14
Fe/HZSM5	Wet ion exchange	2.42	42.0	2.83

Coke is known to deactivate metal/HZSM-5 catalysts in DHA [20]. Recently, Bao et al.[153] demonstrated that atomically dispersed Fe in silica results in the formation of methyl radicals, which then undergo C-C coupling in the gas phase, without coke formation. In order to test if atomically dispersed iron in HZSM-5 can also effectively suppress coke formation, the amount of coke formed on the three catalysts was determined after each reaction (10 hrs time-on-stream) and is shown in table 6. Since all Fe in Fe@HZSM-5 can be fully reduced to metallic state, we also evaluate the coking data for Fe@HZSM-5 before its Fe content is fully reduced to Fe^0, i.e. after the first 23 min time-on-stream, as suggested by figure 42). Note that for this catalyst coke selectivity increases dramatically from 16.2% at 23 min to 94.8% at 10 hrs time-on-stream, indicating that metallic Fe^0 NPs result in extensive coke formation. This is consistent with the report by Bao et al. who also identify Fe^0 particles as the coke-producing Fe species[153]. In contrast to Fe@HZSM-5, Fe/HZSM-5 contains only a minor fraction of Fe NPs, while H-(Fe)ZSM5 has no such species. Thus, the coke selectivity, which decreases in the order of Fe@HZSM-5 > Fe/HZSM-5 > H-(Fe)ZSM-5, correlates well with the Fe dispersion in these three catalysts, i.e. increasing Fe dispersion results in reduced coke formation.

However, the total coke formation normalized to the Fe content does not follow this order. It is well established that coke is formed over bi-functional zeolite catalysts in DHA in two ways[139]: (a) from dehydrogenation of methane (‘‘CH_X’’) in parallel with the desired C–C bond formation step, and (b) from the secondary reactions of the desired aromatic products on the BAS of the zeolite. Table 6 hence also shows the amount of benzene formation over the duration of these experiments, and one can see that the coke amount indeed increases systematically with the amount of benzene produced, similar to previous observations with Zn-HZSM-5 catalysts[129]. This hence confirms that coke formation over Fe-HZSM-5 is also caused

by secondary reactions of benzene on BAS. Moreover, this type of coke is more dominant than coke on Fe^0 sites at our reaction condition, as reflected in the total amount of coke observed. Thus, even though our observations confirm that atomically dispersed Fe results in no or very little coke formation, coke formation cannot be eliminated from Fe-HZSM-5 in DHA due to secondary reactions of the products on the zeolitic BAS.

5.3 CONCLUSION

The abundance of natural gas resources has strongly increased interest in catalytic dehydroraomatization of methane to benzene. Fe-based zeolite catalysts are potentially highly promising candidates for this reaction due to earth-abundance and low cost of Fe. However, the reactivity of different Fe species in these catalysts is poorly understood to-date, making rational catalyst design a difficult if not elusive task. In the present study, we aimed to fill this gap by elucidating the role of a range of different Fe species in Fe/HZSM-5 catalysts for DHA.

We successfully synthesized different Fe species within HZSM-5, including Fe in the HZSM-5 framework, Fe at cationic exchange sites, and Fe_2O_3 NPs. This allowed for the development of structure-performance relationships via careful material characterization and catalytic reaction testing. Our results show that benzene selectivity of the Fe-HZSM-5 catalyst is strongly correlated with the presence of highly dispersed Fe (as Fe_3O_4 or FeO) in HZSM-5 micropores. Such Fe species presumably allow the formation of methyl radicals, which then oligomerize on the BAS to take advantage of shape selectivity of ZSM-5. We furthermore show that high (atomic) dispersion can effectively suppress coke formation on the Fe species. However, strong coke formation still occurs for these catalysts via secondary reaction of aromatic products

over BAS in the micropores. This coking issue could be overcome, however, via deactivation of the BAS site, for example through silanation on the zeolite[77, 166]. Thus, the present results yield insights into Fe/HZSM-5 catalysts that can give direct guidance for further catalyst design and may allow combination of the good benzene selectivity of atomically dispersed iron in MFI zeolites with low or no coking, opening a path towards commercially viable methane dehydroaromatization at comparatively mild conditions.

6.0 MO/HIERARCHICAL ZSM-5 FOR METHANE DEHYDROAROMATIZATION

Benzene is one of the most important organic intermediates in the petrochemical industry, and currently, it is mainly produced from crude oil processing. However, the increasing price difference between oil and natural gas[148] due to the availability of abundant shale gas has renewed interest in the development of a process for the direct conversion of methane to benzene. This can be achieved via methane dehydroaromatization (DHA). The most promising catalyst reported to date is bi-functional Mo/HZSM-5 (catalysts)[2], where methane conversions of ~10% X_{CH4} with 80% benzene selectivity at a typical reaction temperature of 700 °C was achieved. Remarkably, such reactivity is very close to the thermodynamic limit of this reaction [19]. However, the main issue of this catalyst is its low stability at the reaction condition. Typically, a Mo/HZSM-5 catalyst can deactivate as quickly as 5h (or less, depending on the reaction conditions[13]) due to coke formation from the secondary reaction of product hydrocarbons on Bronsted acid site (BAS)[167-168]. Moreover, such coke is predominantly produced within micropore of ZSM-5 due to the large network of ZSM-5 microporous structure whose small pore size enhances the chance of hydrocarbons to contact with BAS. The formed coke then covers active sites and deactivates the catalyst.

To address mass transfer issue of zeolites, many efforts have been made to create extra mesopores (i.e. hierarchical structure) to enhance mass transfer efficiency in order to suppress coke formation. One of the most common approaches is demetallization, such as desilication and

dealumination[53-57]. This approach can easily create significant amount of mesopores. However, demetallation alters the Si:Al ratio (SAR) in the zeolite and SAR is critical for catalytic performance of zeolite materials, as it determines the availability of BAS. Thus, it is difficult to compare the catalytic performance of Mo loaded hierarchical ZSM-5 catalysts prepared through this approach. Another approach is based on the use of templates during zeolite crystallization and can be further categorized depending on the type of template used, i.e. use of soft templates (such as co-surfactants or dual-templating surfactant[105-107] or hard templates (such as carbon black (CB) or carbon nanofibers[63-65]). The templating strategies generally result in more ordered mesopores. For example, Y. Wu et al.[62] used diquaternary ammonium surfactant to create lamellar ZSM-5 catalysts with ordered mesoporosity and were studied in DHA reaction. They reported that such hierarchical zeolite catalyst enable efficient catalytic reactivity in the initial stage of reaction, while their performance were no different to conventional zeolite catalysts in the long term run. Moreover, the coke formation from Mo loaded hierarchical zeolites is even higher than conventional Mo/HZSM-5 catalysts. Mo loaded hierarchical ZSM-5 created by CB is also often reported for DHA[66-67]. In contrast to the conclusion from Y. Wu et al., the authors conclude that hierarchical structure of ZSM-5 can strongly reduce coke formation and hence to extend the lifetime of catalyst. To date, however, rare systematical study of hierarchical ZSM-5 was done for DHA. Usually, the catalytic performance was compared between one conventional Mo/HZSM-5 with one Mo/hierarchical HZSM-5 and then a conclusion was made. The trend of changing porosity on DHA could be neglected. As a result, there is an apparent controversy for mesoporisity in suppression coke formation and extending catalyst lifetime as discussed above.

In this chapter, we create hierarchical structures of ZSM-5 systematically with different amount of CB template. The created hierarchical ZSM-5 materials and the subsequent

Mo/hierarchical HZSM-5 catalysts were characterized by XRD, BET, SEM, TEM and TGA/TPD external surface acidity characterization technique. The structure of catalysts was correlated with the correspondence catalytic performance conducted in a fixed-bed reactor. We show that a minimum amount of coke with high benzene selectivity can be achieved by an optimized porosity of ZSM-5.

6.1 EXPERIMENTAL

6.1.1 Materials and methods

6.1.1.1 Hierarchical NaZSM-5

Hierarchical Na-ZSM-5 materials are synthesized by using 0.55g H_2O, 3.16g ethanol, 3.7g 40 wt% tetrapropyl ammonium hydroxide (TPAOH), and 0.082g sodium aluminate and sonicate for 2hr. Carbon black (BP2000)- 0g, 0.5g, 1g, 1.5g, or 2.5g- was combined with above solution. The mixed solution then was allowed to evaporate ethanol. After 20 hours, 4.17 g of tetraorthosilicate (TEOS) solution was added to make a molar synthesis feed of TPAOH: 20 H_2O: 2.4 TEOS and kept for 3 hours. The solution was then transferred into hydrothermal reactor and was heated to 180 ˚C at 0.5 ˚C/min in an oven. The hydrothermal reaction was kept at this temperature for 66h. After being removed from the oven and cooled to room temperature, samples were washed with deionized water and centrifuged. This process was repeated for four times. The samples were then dried at 100 ^{0}C overnight. Finally, the samples were calcined at 600 ˚C for 8h.

6.1.1.2 Mo/HZSM-5

The hierarchical Na-form ZSM-5 created by using different amount of CB was ion exchanged with aqueous NH_4NO_3 solution, washed, dried and calcined at 500 °C, to obtain H-ZSM-5. Mo/HZSM-5 was prepared via impregnation of HZSM-5 with $(NH_4)_6Mo_7O_{24}\cdot 4H_2O$ in aqueous solution at room temperature. The obtained catalysts were dried and calcined at 500 ^{0}C for 6h.

6.1.2 Catalyst characterization

6.1.2.1 X-ray diffraction (XRD)

Powder X-ray diffraction (XRD) measurements were performed with a high-resolution powder X-ray diffractometer (Bruker D8 Discover) using a monochromatic Cu radiation at the wavelength of 1.54 Å. The beam voltage was 40 kV at a current of 40mA. The diffraction patterns were recorded with a step of 0.02^0 (2θ), 0.5 sec/step.

6.1.2.2 Surface area and porosity Analysis

Surface area and porosity are determined nitrogen sorption in a Micromeritics ASAP 2020. Samples were degassed for 24 hours at 300 °C under high vacuum prior to each analysis. Both nitrogen adsorption/desorption measurements were performed at liquid nitrogen temperature (77 K). The typical test involved a 6-point Brunauer- Emmett-Teller (BET) analysis for total surface area measurement in the relative pressure range $0.1<P/P0<0.35$. Mesopore size, volume, and surface area determination were calculated by the Barret-Joyner-Halenda (BJH) method. Micropore surface area was obtained via subtracting BET surface area are with mesopore surface area. All reported pore properties were acquired by analyzing the adsorption isotherm data.

6.1.2.3 Electron microscopy and X-ray microanalysis

JEOL JSM-6510LV field emission scanning electron microscope (SEM) was used to determine material morphology at beam voltage of 20 kV. A thin palladium film was sputter coating on the sample before measurement. Nanoscale morphology was determined by a high resolution transmission electron microscopy (HRTEM, JEOL-2100). Samples were dispersed on a copper type-B support grid (Ted Pella Inc.). The actual chemical composition of Mo/HZSM5 catalysts was determined by energy dispersive analysis of X-ray (EDX) equipped on SEM (JEOL JSM6510LV), with a collection time of 240- 300 s.

6.1.2.4 External surface acidity

To measure the surface acidity, tetrapropyl ammonium (TPA) ion was adsorbed onto Mo loaded H-ZSM-5 via reacting 0.1g of Mo/HZSM-5 with 20mL of 1.0M tetrapropyl ammonium bromide (TPABr) overnight[169]. The catalysts were washed copiously with water and dried at 120 ^{0}C. Thermogravity Analysis/Temperature Programmed Desorption (TGA/TPD) [170] analyses were then obtained using the assumption that 1 mol of TPA would titrate as 1 mol of NH_3 desorbed after the thermally induced Hoffmann elimination reaction of tetrapropylammonium to propene and ammonia. The TGA/TPD experiment was conducted by SDTQ600, TA instruments. Typically, alumina pans containing ~10 mg of TPA+ adsorbed sample powders were loaded on to the instrument. The temperature was ramped up to 550 ^{0}C at 5 ^{0}C/min in N_2 and the change of sample weight was recorded.

6.1.2.5 Reactivity evaluation

The reaction was carried out in a fixed-bed reactor at 700 ^{0}C and atmospheric pressure. Typically, catalysts were charged into a 5.0 mm i.d. quartz tubular reactor. The reactor tube was

heated from room temperature up to 500 ^{0}C for catalyst pretreatment in air, and then heated to desired reaction temperature (700 ^{0}C) under helium flow. After temperature equilibration, methane (5.3 sccm) was introduced onto the catalyst. The typically used gas hourly space velocity (GHSV) was 1875 (cc/g/hr) for catalytic performance comparison between different catalysts. The effluent gas products were analyzed by both Balzers Quadstar GSD 300 mass spectrometer (MS) and Agilent 3000A Micro GC equipped with thermal conductivity detectors (TCD). An amount of 50% He was added to the methane feed as an internal standard. The methane conversion, selectivity of products was evaluated according to the carbon mass balance. Total coke formation was determined based on CO and CO_2 signal detected in MS during temperature-programmed-oxidation (TPO) (in 20% O_2) of the spent catalysts.

6.2 RESULTS AND DISCUSSION

6.2.1 Material characterization

6.2.1.1 NaZSM-5

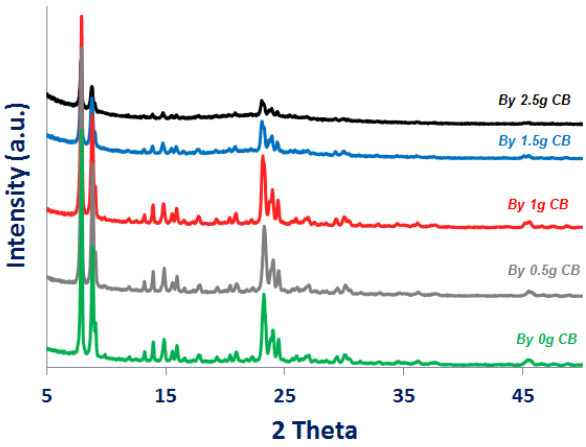

Figure 44. XRD pattern for NaZSM-5 synthesized with different amount of CB.

NaZSM-5 prepared with different amounts of CB exhibit qualitatively identical XRD diffraction patterns (figure 44), indicating the MFI zeolite structure of all catalysts. For CB less than 1g, the peak intensity shows almost constant. However, the peak intensity starts to decrease with amount of CB used as CB >1g, suggesting either decreased crystallinity or decreased primary particle size.

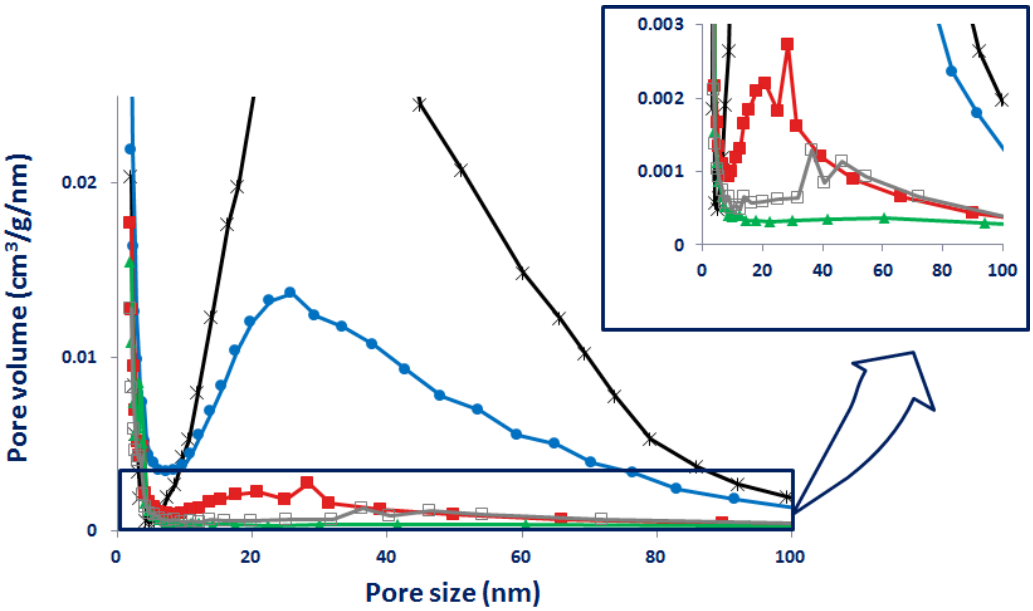

Figure 45. BJH adsorption pore size distribution of a) NaZSM-5 and b) Mo/HZSM-5 synthesized with different amount of CB. (Solid triangle): by 0g CB; (open square): by 0.5g CB; (solid square): by 1g CB; (solid circle): by 1.5g CB; (solid asterisk): by 2.5g CB.

Table 7 shows textural properties of NaZSM-5 support. BET surface area remains almost constant for all prepared NaZSM-5. NaZSM-5 synthesized without CB shows barely mesoporosity (low mesopore volume and surface area). Mesopore volume/surface area increases with increasing CB amount, indicating mesopore is successfully formed via using CB as the template. The formed mesopore size is shown in figure 45. Typically, the mesopore size is ~20-40 nm. However, micropore surface area decreases accordingly. This porosity change is similar to many reports in the literature[171]: creating mesoporosity within zeolites is commonly accompanied with decreasing microporosity. Overall, one can see that both micropore surface area and mesopore surface area do not apparently change when low amount of CB used, while both change significantly when CB used > 1g. This result indicates effect of CB on NaZSM-5 becomes very strong as CB used >1g.

Table 7. Texture properties of NaZSM-5 and Mo/HZSM-5 synthesized with different amount of CB.

Sample	Amount of CB used for ZSM-5 synthesis(g)	S_{BET} (m^2/g)	S_{meso} (m^2/g), 4-100mm	S_{micro} (m^2/g)	V_{meso} (cm^3/g), 4-100 nm
NaZSM-5	0	314	8	284	0.027
	0.5	328	9	301	0.039
	1	309	15	263	0.077
	1.5	305	57	180	0.33
	2.5	303	100	116	0.81
Mo/HZSM-5	0	321	12.7	258	0.044
	0.5	329	10.3	263	0.05
	1	328	15	246	0.09
	1.5	284	77	146	0.44
	2.5	250	135	71	0.77

1. All porosity calculated from adsorption isotherm
2. Smicro is estimated by Smicro= SBET – Smeso+macro

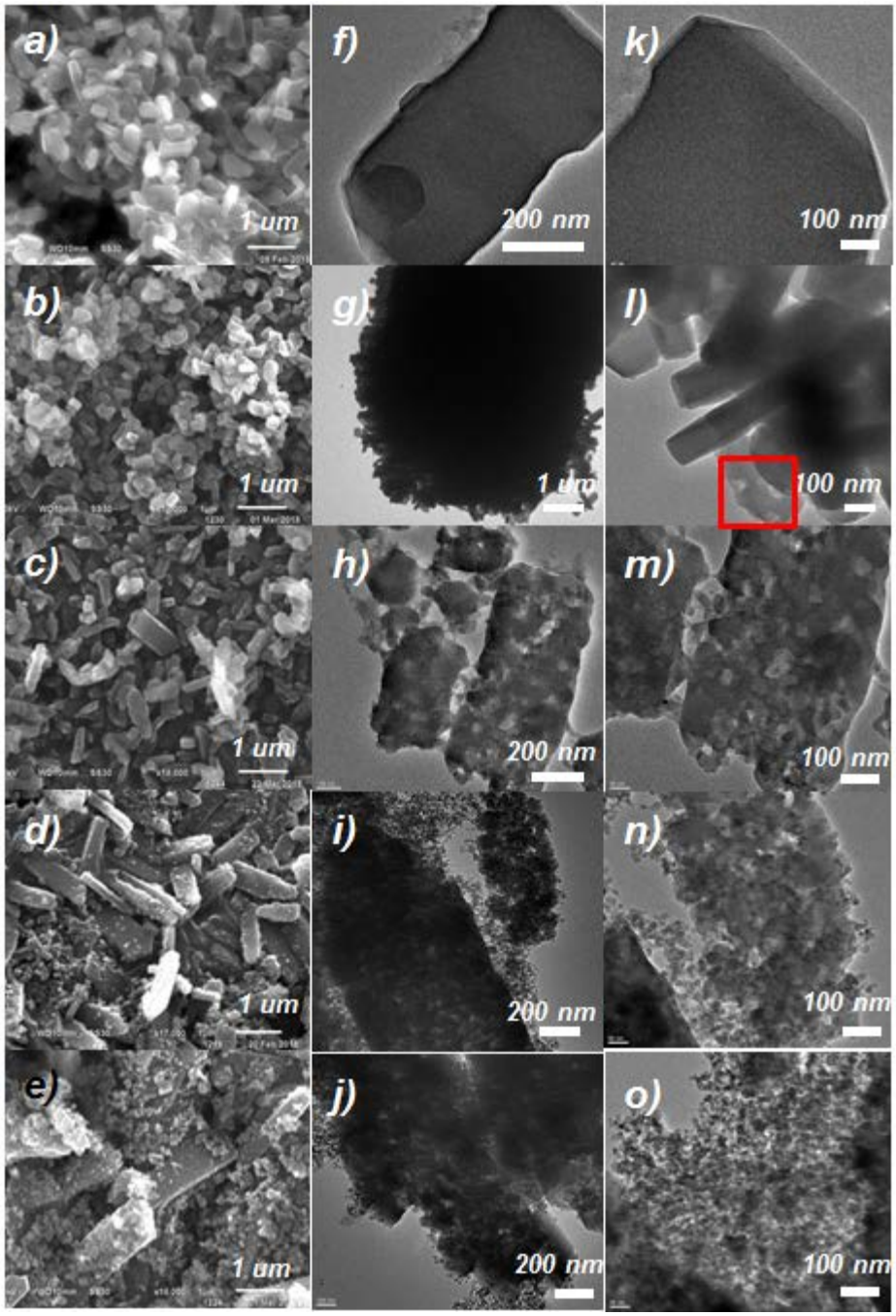

Figure 46. (a to e) SEM and (f to o) TEM images of NaZSM-5 synthesized with different amount of CB. a), f), and k) are synthesized with 0g CB; b), g), and l) are synthesized with 0.5g CB. c), h), and m) are synthesized with 1g CB. d), i), and n) are synthesized with 1.5g CB. e), j), and o) are synthesized with 2.5g CB.

TEM and SEM images (figure 46) show the morphology of ZSM-5 prepared with and without CB in the hydrothermal environment. SEM shows NaZSM-5 synthesized without (by 0g) CB possesses rod-like crystals in micron size. TEM shows these crystal surfaces are smooth and no mesopores can be observed. When 0.5g CB is used, SEM shows similar rod-like crystals. However, TEM indicates that mesopores start to be seen on the edge of these crystals. When CB used is increased to 1g, mesoporous structure becomes throughout the rod-like crystals. Interestingly, when CB used is further increased to 1.5g, not only the rod-like crystals become even more mesoporous, but also small particles are formed. These small particles agglomerate together to form porous structures. Both amounts of small particles and mesoporous structures within rod-like structure further increase as 2.5g CB is used. Overall, SEM and TEM images show that mesopores increase with increasing CB amount, and the pore size observed is predominantly around 20-40 nm. This observation of morphology change is consistent with the porosity analysis in table 7 and figure 45. Formation of mesopores within rod-like crystals (<1g) results in slight increase of mesoporosity and it does not significantly affect microporosity of ZSM-5. However, high amount of CB (>1g) in ZSM-5 synthesis results in formation of aggregated small-particles which contribute significantly to mesoporosity. These small ZSM-5 particles, however, have much smaller microporosity compared to micron-size ZSM-5 crystals. Microporosity of zeolites is directly reflected on the XRD patterns (figure 44). Highly crystalline ZSM-5 typically possess high amount of microporosity. One can see that the porous rod-crystal which has high microporosity does not affect the XRD crystallinity (<1g CB) while formation of small ZSM-5 particle (>1 g CB) which has low microporosity shows a much lower crystallinity.

Based on above characterization, we conclude that increasing CB successfully increases mesoporosity in NaZSM-5. Low amount (<1g) of CB results in ZSM-5 crystallites which grow

around CB during the hydrothermal treatment. After burning off CB, mesopores are created within ZSM-5 crystals. Mesoporosity does not increase significantly in this CB amount range. However, as CB used is greater than 1g, CB becomes dominant in the synthesis system, where ZSM-5 forms small particles between primary CB particles and mesoporosity increase drastically. This big increase in mesoporisity, however, also reduces microporosity of NaZSM-5 material. Change of hierarchical NaZSM-5 formation mechanism is summarized in scheme 2.

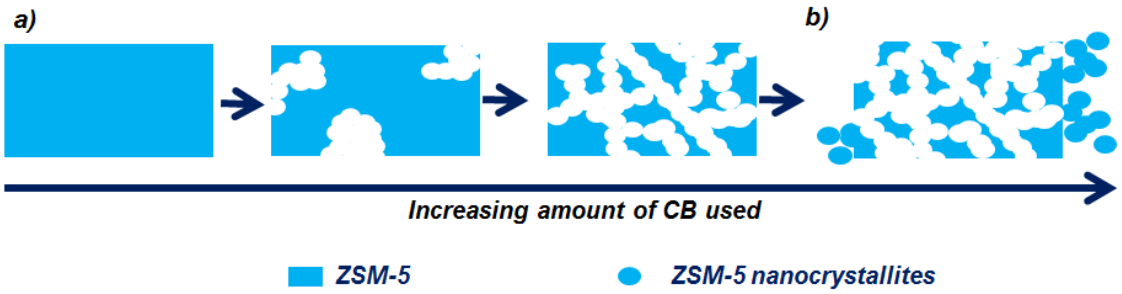

Scheme 2. Schematic morphology of NaZSM-5 synthesized by different amount of CB. a) CB in hydrothermal synthesis < 1g. b) CB in hydrothermal synthesis > 1g.

6.2.1.2 Mo/HZSM-5

In order to make a DHA catalyst, the prepared NaZSM-5 with different porosity was ion-exchanged with ammonium nitrate to obtain H-form ZSM-5 and then impregnated with Mo. 3 wt% Mo is prepared in order to achieve comparable reactivity to the literature[13, 17, 52, 139]. Chemical compositions of the catalysts are determined by EDX (table 8). The results show that Mo loading and Si/Al are close to nominal compositions and are similar among all catalysts. Thus, the effect of porosity on catalytic performance can be studied without interference from other parameters.

Table 8. Chemical composition of Mo/HZSM-5 catalysts used in this study, as determined by EDX.

Sample	Amount of CB (g) used in ZSM-5 synthesis	Si/Al	Mo (wt%)
Mo/HZSM-5-0g	0	26	2.76
Mo/HZSM-5-0.5g	0.5	24.6	3.25
Mo/HZSM-5-1g	1	26	3.00
Mo/HZSM-5-1.5g	1.5	25.9	3.28
Mo/HZSM-5-2.5g	2.5	28	2.9

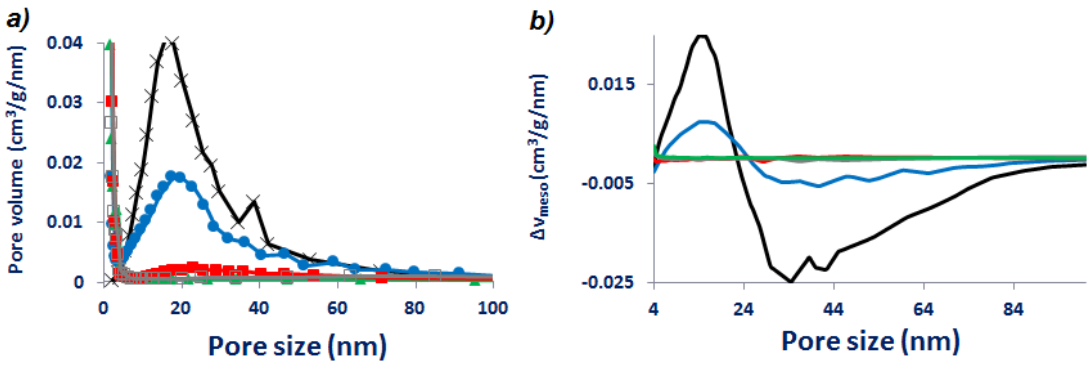

Figure 47. Change of mesoporosity before and after Mo impregnation. (Solid triangle): by 0g CB; (open square): by 0.5g CB; (solid square): by 1g CB; (solid circle): by 1.5g CB; (solid asterisk): by 2.5g CB.

Table 8 shows textural properties of Mo/HZSM-5. Micropore surface area decreases after impregnation of Mo (compare to NaZSM-5), indicating diffusion of Mo into micropores during impregnation process (i.e. heat treatments) and forms small Mo species[68]. As for mesoporosity, mesopore surface area increase as CB used is greater than 1g but mesopore volume all remain almost unchanged. To investigate what causes this discrepancy, figure 47a shows mesopore size distribution of these catalysts. The mesopore size of all zeolite-supported Mo catalysts all show ~20 nm. Compared to NaZSM-5 without Mo (figure 45), the mesopore size decreases significantly as high amount of CB used (>1g). The change of mesopore size is further indicated by figure 47b. Based on this change, it's very likely that some Mo forms MoO_3 particles on mesopores of ZSM-5 and occupies the mesoporous space. Furthermore, MoO_3 particles formed in the mesopores should have particle size about 4-50 nm since mesopore size decreases from 24-70 nm to ~20 nm after Mo impregnation.

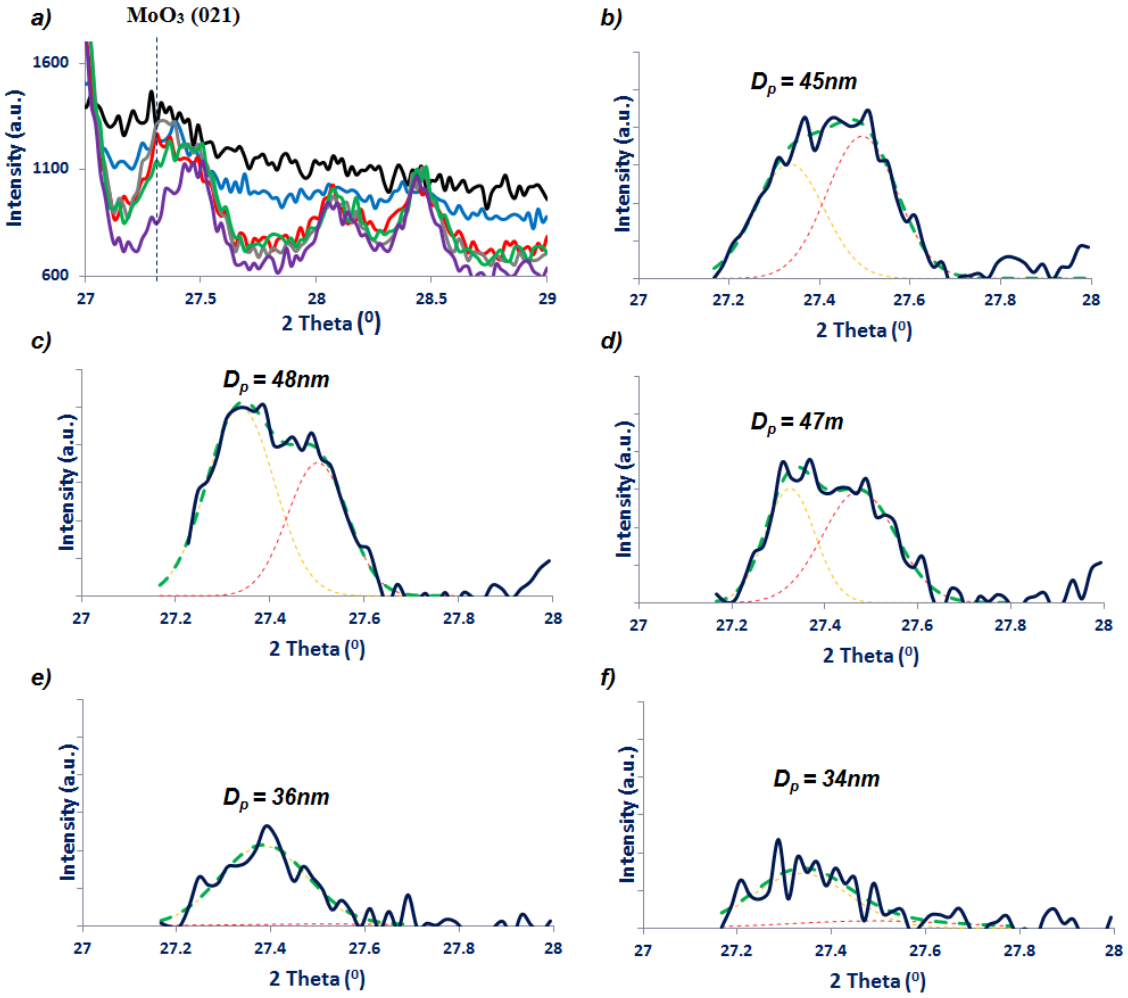

Figure 48. a) XRD patterns for HZSM-5 and Mo/HZSM-5 with different msoporosity. (Purple): HZSM-5, (green): Mo/HZSM-5-0g, (gray): Mo/HZSM-5-0.5g, (red): Mo/HZSM-5-1g, (blue): Mo/HZSM-5-1.5g, and (black): Mo/HZSM-5-2.5g. Deconvolution of XRD peak (27-280) for b) Mo/HZSM-5-0g, c) Mo/HZSM-5-0.5g, d) Mo/HZSM-5-1g, e) Mo/HZSM-5-1.5g, and f) Mo/HZSM-5-2.5g.

To confirm this hypothesis, MoO_3 particle size is confirmed by XRD (with Scherrer equation). For Mo/HZSM-5, most reflections from MoO_3 overlap with strong reflections of HZSM-5. However, a MoO_3 (021) reflection at 2 theta ~27.3^0, although it is still very close to a HZSM-5 reflection (figure 48a) (and hence is often neglected in the literature), is observed to be distinct enough for analysis. To quantify the particle size by Scherrer equation, we did a

deconvolution for this peak and it is shown in figure 48b-f. For Mo/HZSM-5 with different mesoporosity, MoO_3 particle sizes are all estimated to be ~30-50 nm (figure 48b-f). This result indicates the MoO_3 size is not dependent on the porosity of the HZSM-5 support. The particle size estimated thus agrees well with the size hypothesized from mesopore size change. In addition, the estimated MoO_3 particle size for Mo/HZSM-5 synthesized with CB < 1g (whose mesopore size remains ~20 nm before and after impregnation) is apparently too big to form within their mesopores and thus no change of mesopore size change is observed.

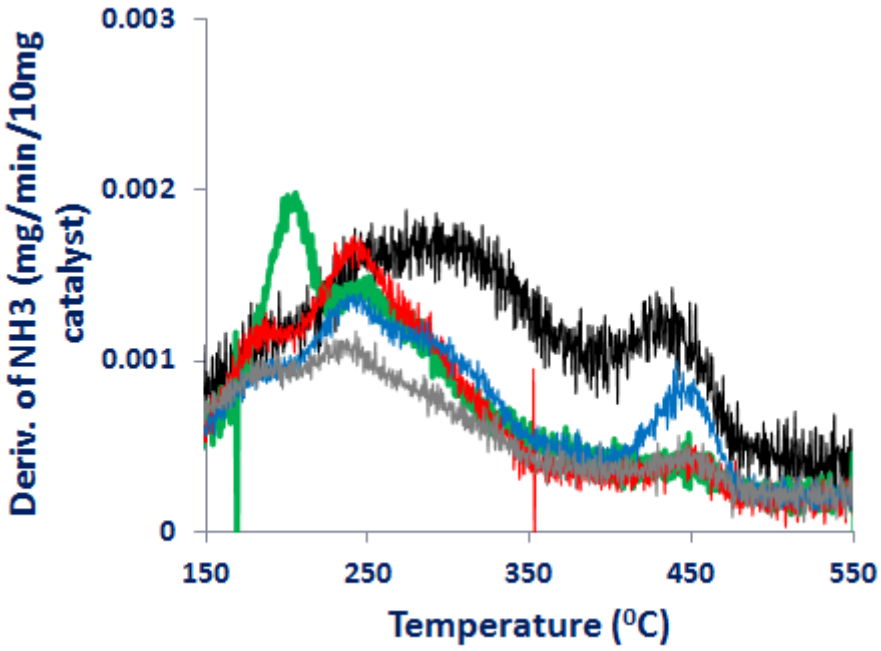

Figure 49. External surface acidity characterized by TPA^+ ion adsorbed on Mo/HZSM-5 followed by TGA/TPD. (green): by 0g CB; (gray): by 0.5g CB; (red): by 1g CB; (blue): by 1.5g CB; (black): by 2.5g CB.

According to DHA reaction mechanism over Mo/HZSM-5 catalysts, methane is activated on Mo site and the generated C-C coupling intermediates then oligomerize on the neighboring BAS to form benzene[13, 16-17, 74] . The high benzene selectivity is attributed to shape selectivity of

ZSM-5 micropore. Thus, it's generally accepted that free BAS on external surface could result in higher hydrocarbon and coke formation. In order to investigate the effect of hierarchical ZSM-5 structure on the distribution of BAS and their consequences on the catalytic performance, the external surface acidity of Mo loaded hierarchical HZSM-5 is determined by a method reported by Chang[169]. This method was conducted by TPA^+ ion adsorbed on Mo/HZSM-5 followed by TGA/TPD. TGA/TPD analyses were then obtained using the assumption that 1 mol of TPA^+ would titrate as 1 mol of NH_3 desorbed after the thermally induced Hoffmann elimination reaction of TPA^+ to propene and ammonia. The experimental theory thus is similar to conventional NH_3-TPD for zeolite acidity characterization except the adsorbed ammonium groups are different (NH_4^+ vs TPA^+). Due to the large molecular size (~1 nm) of TPA^+, which is not allowed to enter micropores of HZSM-5, this approach determines only acidic sites on the HZSM-5 external surface (including mesopore surface in this research). Figure 49 shows profiles of TGA/TPD for the five Mo/HZSM-5 catalysts with different porosity. Each spectrum contains four desorption peaks at ~200 ^{0}C, ~230 ^{0}C, ~300 ^{0}C, and ~430 ^{0}C. These peak positions as expectedly are qualitatively similar to the NH_3-TPD profile reported for Mo/HZSM-5.

According to the reported NH_3-TPD profile reported[95, 108, 135] , the desorption peak at ~230 ^{0}C is attributed to weak acid site (Lewis acid sites of HZSM-5) and the peak at ~430 ^{0}C results from BAS of HZSM-5. A shoulder at ~300 ^{0}C was previously attributed to stronger Lewis acid sites created by metal oxides[89]. A low temperature desorption peak at ~200 ^{0}C is simply from physisorbed ammonium group and hence is not an indication for any acidic sites. It's noted that no evidence so far shows Lewis acid sites of HZSM-5 has any impact on the DHA reaction. Based on these assignments, Mo/HZSM-5-0g, Mo/HZSM-5-0.5g, and Mo/HZSM-5-1g which are consisted of (microporous/mesoporous) micron-size ZSM-5 crystals contain minimal amount

of BAS on the external surface. However, as CB used is greater than 1g, amount of BAS increases pronouncedly. Previously, it has been demonstrated that ZSM-5 nanoparticles start to appear as CB used >1g. From the result of external surface acidity, apparently, BAS is preferably distributed on external surface of ZSM-5 nanoparticles but not on the external surface of miron-size crystals. This presumably results from much larger external surface area of nanoparticles than that of mesoporous crystals (table 7). High amounts of BAS on external surface of ZSM-5 nanoparticles is consistent with the conclusion made by Bao's group[43]. In addition, Mo/HZSM-5-1.5g and especially Mo/HZSM-5-2.5g seem to contain more metal oxide (MoO_3) Lewis acid sites (at ~300 ^{0}C), say, more MoO_3 particles on the external surface compared to other catalysts. This is not surprising. Due to relatively large mesoporosity to microporosity ratios of these two catalysts, more Mo species are distributed onto the external surface. Overall, large external surface area due to ZSM-5 nanoparticle formation results in more BAS and Mo distributed on the external surface.

6.2.2 Catalytic performance

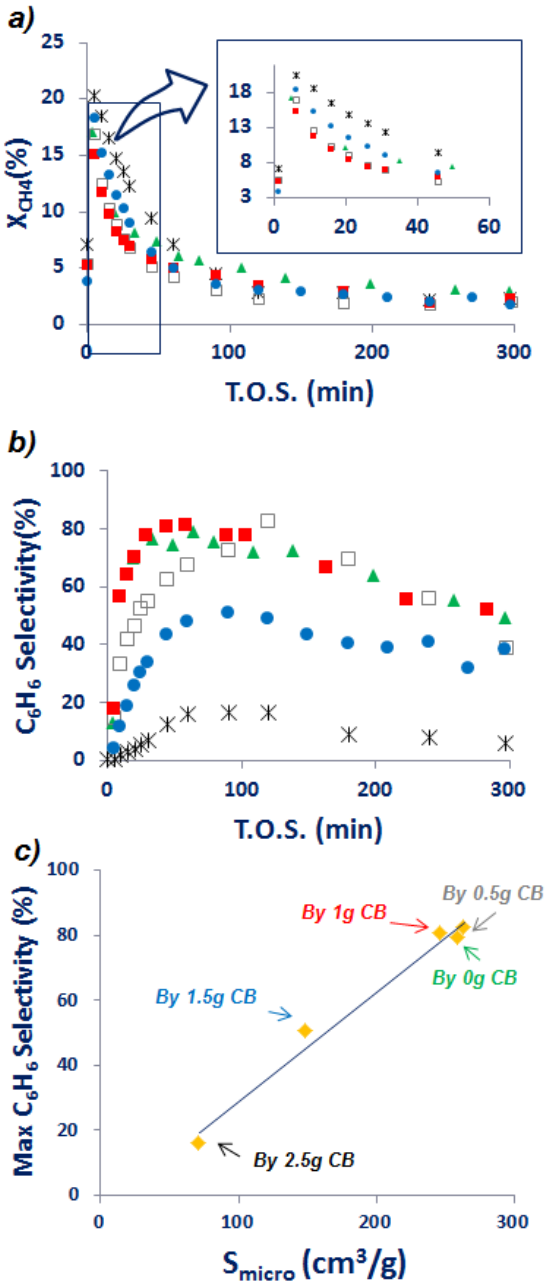

Figure 50. DHA Reactivity data over Mo/HZSM-5 catalysts synthesized with different amount of CB: a) methane conversion and b) benzene selectivity. (Solid triangle): by 0g CB; (open square): by 0.5g CB; (solid square): by 1g CB; (solid circle): by 1.5g CB; (solid asterisk): by 2.5g CB. c) Micropore surface area vs. max benzene selectivity. The reaction was carried out at 700 ^{0}C, GHSV: 1875 cc/g/hr.

The catalytic performance of Mo/HZSM-5 catalysts with different porosity is shown in Figure 50. Methane conversion is very similar for all catalysts except that Mo/HZSM-5-2.5g shows a higher reactivity in the first 60 mins reaction. Coincident with induction period at the beginning of DHA reaction (reducing MoO_3 to MoO_xC_y)[31, 72, 149] and high amount of Mo dispersed on the external surface (see the discussion for figure 49), a possibility to cause this higher methane conversion could be more coke formed on the external Mo site to form MoO_xC_y due to an unrestricted space for carbon growth. This hypothesis will be confirmed later in the section of coke characterization. For a long period of reaction (>60 min), however, all catalysts show similar methane conversion. This indicates catalytic stability of all catalysts is very similar and agrees with the catalytic stability of Mo/hierarchical zeolite recently reported by Y. Wu et al.[62].

On the other hand, figure 50b shows that C_6H_6 selectivity of Mo/HZSM-5-0g, Mo/HZSM-5-0.5g, and Mo/HZSM-5-1g reaches ~80% after the induction period, while the max selectivity is significantly lower for the other two Mo/HZSM-5 catalysts synthesized with 1.5g and 2.5g CB (C_6H_6 selectivity: Mo/HZSM-5-1.5g > Mo/HZSM-5-2.5g). It is well known that DHA over Mo/HZSM-5 catalysts requires the shape selectivity of ZSM-5 micropore to achieve high benzene selectivity[29]. From prior sections, we have shown that increasing significant amount of mesoporosity (mainly due to ZSM-5 nanoparticle formation) simultaneously results in dramatic decrease of microporosity. To further illustrate the correlation between benzene selectivity and microporosity, a plot of micropore surface area versus maximum C_6H_6 selectivity is shown in figure 50c. Clearly, a linear correlation is obtained and it actually follows this trend: less micropore surface results in less benzene selectivity. Thus, the decreased benzene selectivity is concluded to be a trade-off for micropores to steric un-restricted mesopores.

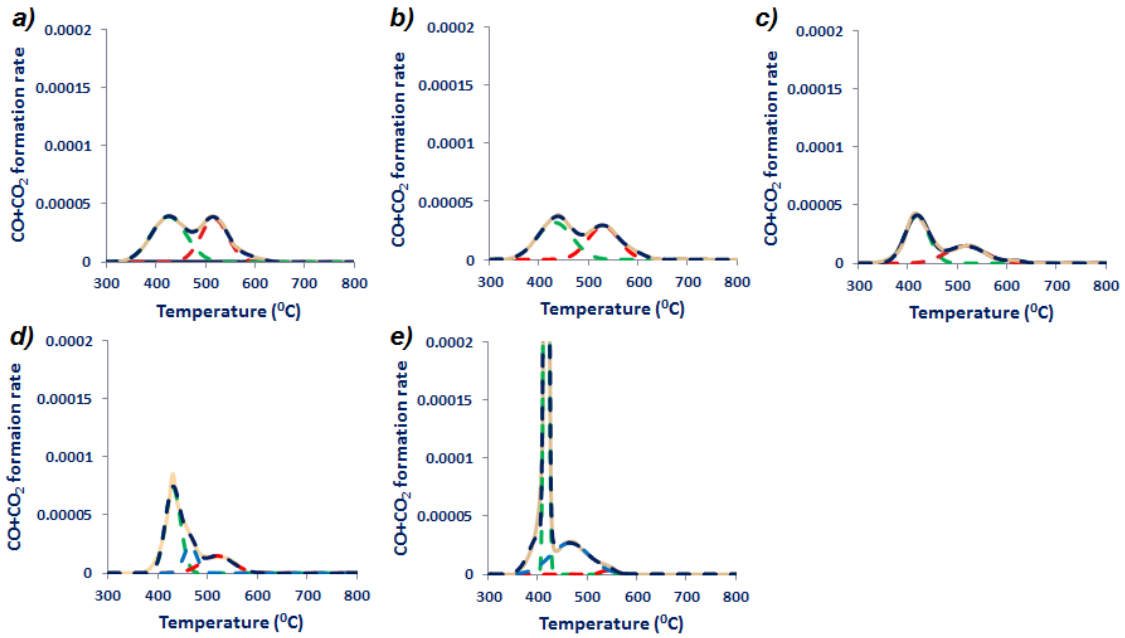

Figure 51. TPO data for spent Mo/HZSM-5 catalysts (after 5h reaction at 700 ^{0}C) with different mesoporosity: a) by 0g CB; b) by 0.5g CB; c) by 1g CB; d) by 1.5g CB; e) by 2.5g CB. Unit of formation rate of ($CO+CO_2$): mol/min/100mg catalyst.

The purpose of preparing hierarchical structure for DHA is to reduce coke formation and hence to extend the catalyst lifetime. However, high catalytic stability as a result of hierarchical structure of ZSM-5 is not observed in this study (figure 50a). It is well known that coke sources resulting from Mo/HZSM-5 are 1) coke associated with Mo and 2) secondary reaction of product hydrocarbons on BAS[8]. To investigate how coking affects catalytic stability, the coking information (coke type and coke amount) for all catalysts is characterized by burning off coke in the spent catalysts by a TPO process (figure 51). A typical TPO profile is observed for all catalysts: a low-temperature peak at ~420 ^{0}C and a high-temperature peak at ~530 ^{0}C. For catalysts prepared by >1g CB, a middle-temperature peak at ~470 ^{0}C is also observable.

According to a TPO characterization for coke species reported by Bao et al.[20, 79], the low-temperature peak results from coking associated with Mo species while the other two hi-temperature peaks are associated with coke on the BAS of HZSM-5. The difference between the latter two peaks was not further discussed in their report. To further correlate each type of coke with Mo/HZSM-5 with different mesoporosity, amount of each type of coke is quantified from the TPO profiles (figure 52).

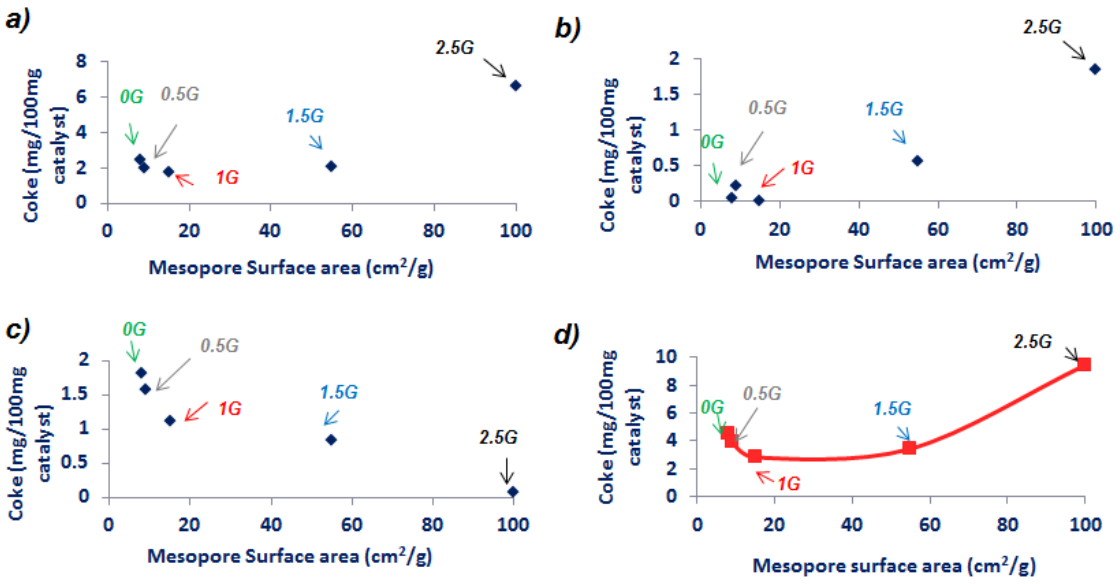

Figure 52. a) Amount of low-temperature coke, b) amount of middle-temperature coke, c) amount of high-temperature coke, and d) Amount of overall coke versus Mo/HZSM-5 catalysts with different mesopore surface area.

Figure 52a shows low temperature coke which is associated with Mo does not change as CB used is less than 1.5g. However, a drastic increase of this type of coke occurs in Mo/HZSM-5-2.5g. This trend, interestingly, correlates very well with the methane conversion, confirming

the first 60-min higher methane conversion of Mo/HZSM-5-2.5g results from more coke on Mo. This connection is reasonable because Mo/HZSM-5 catalysts in DHA reaction require an activation time to reduce MoO_3 to active MoO_xC_y at the beginning of the reaction, and this time period agrees with the higher methane conversion of Mo/HZSM-5-2.5g at the first 60 mins. Moreover, more Mo distributed on external surface of this catalyst is already indicated by external MoO_3 Lewis acid sites (figure 49). As a result, coke associated with these Mo has more room to grow and hence more coke associated with Mo is observed on this catalyst. Nonetheless, this type of coke is normally active in DHA and generating C-C coupling intermediates. No deactivation of catalysts was reported by this type of coke[168].

Figure 52b,c shows middle- and high-temperature coke which are associated with BAS. However, these two type of coke shows opposite trends: the middle-temperature coke does not change as CB used <1g but it increases dramatically as CB used >1g, while the high-temperature coke decreases continually with increasing CB used. Interestingly, changes of the two type of coke correlate very well with the free BAS on the external surface and changes of porosity. On one hand, free BAS on external surface is known to result in higher hydrocarbon and coke formation due to no shape selectivity. From prior section, figure 49 has shown that free BAS on external surface barely appear on Mo/HZSM-5-0g, Mo/HZSM-5-0.5g, and Mo/HZSM-5-1g. However, this site increases as CB used is >1g due to increase of large-external-surface-area HZSM-5 nanoparticle formation. More coke on external BAS then is expected to increase as CB used is >1g. This agrees very well with the trend of middle-temperature coke. Apparently, the middle-temperature coke is associated with BAS on the external surface. On the other hand, due to higher amount of mesopores (meanwhile, less amount of micropores) created by more CB, which increases from 0 to 2.5g, product benzene can easily diffuse out of the micropores and

hence less coke is formed on BAS within micropores. This change is consistent with the change of high-temperature coke, which becomes less as mesoporosity gradually increases. Thus, the high-temperature coke is attributed to coke formed on microporous BAS. Nonetheless, the change of coke formation on BAS, which is normally regarded as the coking source to deactivate Mo/HZSM-5 catalyst, doesn't seem to improve the catalytic stability (see figure 50c).

In combination of changes of the three types of coke, we observe that the overall coke amount decrease (as CB<1g) and then increase (as CB >1g) with increasing mesoporosity (Figure 52d): the decrease of overall coke is attributed to increased mesoporosity which results in better product benzene diffusion (reduction of high-temperature coke), while the increased overall coke results from the increasing coke formed on external surface (both on external Mo and BAS) outweighing the decreased coke formed within micropores. Overall, increasing mesoporosity in HZSM-5 does not always reduce coke formation. Amount of mesoporosity has to be optimized in order to achieve minimum coke formation in DHA reaction.

6.3 CONCLUSION

In this chapter, hierarchical ZSM-5 is created via embedding CB within/between ZSM-5 crystals followed by burning of CB. Changing amount of CB used for the synthesis successfully results in a different extent of porosity: mesoporosity is formed within ZSM-5 crystals while microporosity is not significantly lost as few CB is used; aggregated ZSM-5 nanoparticles which contains significant amount of mesoporosity and much less microporosity is formed as large amount of CB is used.

Increasing mesoporosity results in less coke formed within HZSM-5 micropores. However, ZSM-5 with too large amount of steric-unrestricted mesopore surface results in great amount of coke formed on the external surface. Amount of mesoporosity has to be optimized in order to achieve minimum coke formation. Nonetheless, no better catalytic stability was observed. Moreover, reduced amount of microporosity as a result of large mesoporosity minimizes the benzene selectivity. Overall, one obtains minimization of coke formation while maintaining high benzene selectivity by introducing a controlled (small) amount of mesoporosity into HZSM-5.

7.0 OUTLOOK

7.1 METAL SITES IN DHA

7.1.1 Zn-based catalysts

In chapter 4, we have given significant insights into the active species in Zn-HZSM-5 catalysts, but the ultimate conclusion is that it appears inherently impossible to synthesize a stable metallic Zn-based zeolite catalyst for DHA due to the reducing reaction conditions and the very high vapor pressure of metallic Zn. However, metallic Zn catalyst is very promising due to its selectivity to benzene, which can achieve almost 100% as suggested in figure 25. Therefore, developing an approach to stabilize metallic zinc clusters within micropores of HZSM-5 will be the next step for this catalyst. This could possibly achieved by alloying approach. Alloying of metals is well-known to improve their physical and chemical stability[147] and could possibly offer a route for stabilization of Zn. However, the impact of such alloying on catalytic activity is unknown. A further investigation will be required.

7.1.2 Fe-based catalysts

Bao *et al*[153] demonstrated that atomically dispersed Fe (on silica) results in the formation of methyl radicals without coke formation, which then undergoes C-C coupling in the gas phase at their reaction conditions (>950 ^{0}C). However, the approach they report to prepare the atomically dispersed iron is very complicated.

In chapter 5, we showed that highly dispersed iron can be easily prepared on HZSM-5 and benzene selectivity of such Fe-HZSM-5 catalyst is much higher than HZSM-5-supported Fe_2O_3 NPs. Although a significant amount of coke is formed on excessive BAS, we demonstrated that highly dispersed Fe can effectively suppressed coke formation on itself and this confirms the conclusion from Bao *et al.*[153]. In other words, if we are able to remove coke formation on BAS, we would be able to completely eliminate coke formation from Fe-HZSM-5 catalysts, which is currently the primary issue of state-of-the-art Mo/HZSM-5 catalysts, and achieve high benzene selectivity. This will require removal of excess BAS in HZSM-5. The most straightforward way to reduce BAS is by adjusting the SAR (i.e. by adjusting amount of Si and Al precursors) for synthesis of ZSM-5, as SAR determines the number of exchange sites/BAS. However, single site Fe in ZSM-5 is mainly stabilized on the exchange sites as already demonstrated in chapter 5. Lowering number of exchange sites prior to introduction of Fe may result in insufficient exchange site to stabilize Fe. Decreasing BAS via decreasing SAR hence will require further investigation. To date, many approaches have been published to deactivate BAS after synthesis of ZSM-5. A very commonly reported method is to conduct silanation on the BAS to cover (deactivate) it[77, 166]. The silanation process can be conducted in the liquid phase or gas phase by TEOS or 3-aminopropyl-triethoxylsilane. However, these silica precursors (~1 nm)

are larger than micropore size of ZSM-5 and hence are only effective in removing surface BAS. A search for smaller size of silica precursor will be a possible solution. Fluorine group was also reported to selectively remove BAS (by dealumination). For example, Chang et al. show that SiF_6^{2-} anion can successfully remove BAS on the external surface of HZSM-5 under static reaction condition[169]. Due to small size of SiF_6^{2-}, this anion group should be able to enter micropores of ZSM-5 and deactivate BAS within micropores if the reaction is carried out in a stirring reactor.

In the future work, preparing atomically dispersed iron over silica is still a good option. Although benzene selectivity over such catalyst can be only ~20% (naphthalene selectivity: ~30%, ethylene selectivity: ~50%), a high methane conversion (>40%) can be achieved at sufficiently high reaction temperature as reported by Bao et al[153]. As discussed above, the catalyst preparation approach reported by their group is extremely difficult. Thus, an easy approach to prepare highly dispersed iron will still make this catalyst viable. Recently, Adam's group reported simple synthesis approaches for preparation of variety of single site metal on silica, including zinc, iron and cobalt[172-174]. The single site catalysts were prepared directly with grafting organometallic precursor or with electrostatic adsorption of metal precursors on silica. The formed metal NPs can be redispersed onto the support to become single site during a pretreatment in H_2. This redispersion process is somehow similar to the step reported by Bao whose iron was redispersed in CH_4. Therefore, it would be worthwhile to test Adam's synthesis approach and study the atomically dispersed iron catalyst prepared for methane upgrading.

7.1.3 Other metal sites

In addition to the reported metals (Mo, Zn, Fe) in this dissertation, other transition metals are also potential to be the metal site for DHA reaction. Furthermore, due to the well know methane activation ability, the focuses should be first put on Cu[175-176] and Ni[176-177].

However, as many inconsistencies reported for other metal loaded HZSM-5 catalysts, changing metal sites for DHA has to be carefully investigated. For example, some reported that Fe as the dopant for Mo/HZSM-5 enhances the catalytic activity but others did not[83, 89, 95]. This was attributed to different metal species obtained by different groups and thus a proper comparison could not be made. Clearly, only a systematic metal site tailoring can screen out the most active and stable species for DHA, as we did for zinc and iron in this dissertation. Especially as we have discussed above, the single site metal should be paid more attention to, as a number of single site metals are recently reported to be very active for variety of reactions[133, 173, 178-180].

7.2 HIERARCHICAL HZSM-5 CATALYSTS

In chapter 6, hierarchical HZSM-5 was systematically prepared by introducing different quantities of carbon black (BP2000) template. Studying the reactivity of tailored HZSM-5 supports, it was found that coke formation within micropores is suppressed if a controlled degree of mesoporosity is introduced into the catalysts, while too much mesoporosity again enhances coke formation, presumable due to “excess space” and BAS for hydrocarbon formation. Moreover, microporosity is decreased, which results in lower benzene selectivity, as a result of large amount of mesoporosity created.

Nonetheless, in this dissertation, the mesoporosity in ZSM-5 was created by one type of carbon black -BP2000- alone. As a result, the mesopore size is constant for all the hierarchical catalysts studied. Moreover, for the catalysts prepared by high amount of BP2000 (i.e. >1g), the mesoporosity is mainly contributed from aggregated ZSM-5 nanoparticles. These nanoparticles, however, have very high amount of BAS on the external surface as suggested by figure 49 and thus results in very high amount of coke formation and less selectivity to benzene. Therefore, in the future work, it would be worthwhile to prepare hierarchical ZSM-5 with different type of carbon black and compare. By using different type of carbon black, the mesopore size should be targeted to be smaller and very dense “within ZSM-5 crystals” to achieve high mesopore volume and avoid high amount of BAS on the external surface (as suggested from figure 46 and figure 49, mesoporosity created within ZSM-5 crystal has barely BAS on the external surface). The microporosity will also remain high and thus maintain high benzene selectivity. With that, further suppressing coke formation to extend the catalyst lifetime could be expected.

BIBLIOGRAPHY

(1) Han, S.; Martenak, D.; Palermo, R.; Pearson, J.; Walsh, D. The direct partial oxidation of methane to liquid hydrocarbons over HZSM-5 zeolite catalyst. *J. Catal.* **1992,** *136*, 578-583.

(2) Wang, L.; Tao, L.; Xie, M.; Xu, G.; Huang, J.; Xu, Y. Dehydrogenation and aromatization of methane under non-oxidizing conditions. *Catal. Lett.* **1993,** *21*, 35-41.

(3) Weckhuysen, B. M.; Wang, D.; Rosynek, M. P.; Lunsford, J. H. Conversion of methane to benzene over transition metal ion ZSM-5 zeolites: I. Catalytic characterization. *J. Catal.* **1998,** *175*, 338-346.

(4) Xu, Y.; Liu, S.; Guo, X.; Wang, L.; Xie, M. Methane activation without using oxidants over Mo/HZSM-5 zeolite catalysts. *Catalysis letters* **1994,** *30*, 135-149.

(5) First, E. L., Gounaris, C. E., Wei, J., and Floudas, C. A. Computational characterization of zeolite porous networks: an automated approach. *Physical Chemistry Chemical Physics* **2011,** *13*, 17339–17358.

(6) Cejka, J.; Van Bekkum, H.; Corma, A.; Schueth, F., *Introduction to Zeolite Molecular Sieves*. Elsevier: 2007; Vol. 168.

(7) Kim, Y.-H.; Borry III, R. W.; Iglesia, E. Genesis of methane activation sites in Mo-exchanged H–ZSM-5 catalysts. *Microporous Mesoporous Mater.* **2000,** *35*, 495-509.

(8) Ohnishi, R.; Liu, S.; Dong, Q.; Wang, L.; Ichikawa, M. Catalytic Dehydrocondensation of Methane with CO and CO< sub> 2</sub> toward Benzene and Naphthalene on Mo/HZSM-5 and Fe/Co-Modified Mo/HZSM-5. *J. Catal.* **1999,** *182*, 92-103.

(9) Gao, J.; Zheng, Y.; Jehng, J.-M.; Tang, Y.; Wachs, I. E.; Podkolzin, S. G. Identification of molybdenum oxide nanostructures on zeolites for natural gas conversion. *Science* **2015,** *348*, 686-690.

(10) Guisnet, M.; Gnep, N.; Alario, F. Aromatization of short chain alkanes on zeolite catalysts. *Appl. Catal., A* **1992,** *89*, 1-30.

(11) Li, B.; Li, S.; Li, N.; Chen, H.; Zhang, W.; Bao, X.; Lin, B. Structure and acidity of Mo/ZSM-5 synthesized by solid state reaction for methane dehydrogenation and aromatization. *Microporous Mesoporous Mater.* **2006,** *88*, 244-253.

(12) Shu, Y.; Xu, Y.; Wong, S.-T.; Wang, L.; Guo, X. Promotional effect of Ru on the dehydrogenation and aromatization of methane in the absence of oxygen over Mo/HZSM-5 catalysts. *J. Catal.* **1997,** *170*, 11-19.

(13) Chen, L.; Lin, L.; Xu, Z.; Li, X.; Zhang, T. Dehydro-oligomerization of methane to ethylene and aromatics over molybdenum/HZSM-5 catalyst. *J. Catal.* **1995,** *157*, 190-200.

(14) Ha, V. T.; Tiep, L. V.; Meriaudeau, P.; Naccache, C. Aromatization of methane over zeolite supported molybdenum: active sites and reaction mechanism. *Journal of molecular catalysis A: Chemical* **2002,** *181*, 283-290.

(15) Ismagilov, Z. R.; Matus, E. V.; Tsikoza, L. T. Direct conversion of methane on Mo/ZSM-5 catalysts to produce benzene and hydrogen: achievements and perspectives. *Energy Environ. Sci.* **2008,** *1*, 526-541.

(16) Wang, D.; Lunsford, J. H.; Rosynek, M. P. Catalytic conversion of methane to benzene over Mo/ZSM-5. *Top. Catal.* **1996,** *3*, 289-297.

(17) Xu, Y.; Shu, Y.; Liu, S.; Huang, J.; Guo, X. Interaction between ammonium heptamolybdate and NH4ZSM-5 zeolite: the location of Mo species and the acidity of Mo/HZSM-5. *Catalysis Letters* **1995,** *35*, 233-243.

(18) Liu, H.; Li, T.; Tian, B.; Xu, Y. Study of the carbonaceous deposits formed on a Mo/HZSM-5 catalyst in methane dehydro-aromatization by using TG and temperature-programmed techniques. *Appl. Catal., A* **2001,** *213*, 103-112.

(19) Spivey, J. J.; Hutchings, G. Catalytic aromatization of methane. *Chemical Society Reviews* **2014,** *43*, 792-803.

(20) Ma, D.; Wang, D.; Su, L.; Shu, Y.; Xu, Y.; Bao, X. Carbonaceous deposition on Mo/HMCM-22 catalysts for methane aromatization: A TP technique investigation. *J. Catal.* **2002,** *208*, 260-269.

(21) Behrsing, T.; Jaeger, H.; Sanders, J. Coke deposits on H-ZSM-5 zeolite. *Applied catalysis* **1989,** *54*, 289-302.

(22) Iliuta, M. C.; Larachi, F.; Grandjean, B. P.; Iliuta, I.; Sayari, A. Methane nonoxidative aromatization over Ru-Mo/HZSM-5 in a membrane catalytic reactor. *Industrial & engineering chemistry research* **2002,** *41*, 2371-2378.

(23) Iliuta, M. C.; Grandjean, B. P.; Larachi, F. Methane nonoxidative aromatization over Ru-Mo/HZSM-5 at temperatures up to 973 K in a palladium-silver/stainless steel membrane reactor. *Industrial & engineering chemistry research* **2003,** *42*, 323-330.

(24) Li, L.; Borry, R. W.; Iglesia, E. Design and optimization of catalysts and membrane reactors for the non-oxidative conversion of methane. *Chemical engineering science* **2002,** *57*, 4595-4604.

(25) Rival, O.; Grandjean, B. P.; Guy, C.; Sayari, A.; Larachi, F. Oxygen-free methane aromatization in a catalytic membrane reactor. *Industrial & engineering chemistry research* **2001,** *40*, 2212-2219.

(26) Wang, L.; Ohnishi, R.; Ichikawa, M. Selective Dehydroaromatization of Methane toward Benzene on Re/HZSM-5 Catalysts and Effects of CO/CO< sub> 2</sub> Addition. *J. Catal.* **2000,** *190*, 276-283.

(27) Liu, S.; Ohnishi, R.; Ichikawa, M. Promotional role of water added to methane feed on catalytic performance in the methane dehydroaromatization reaction on Mo/HZSM-5 catalyst. *J. Catal.* **2003,** *220*, 57-65.

(28) Yuan, S.; Li, J.; Hao, Z.; Feng, Z.; Xin, Q.; Ying, P.; Li, C. The effect of oxygen on the aromatization of methane over the Mo/HZSM‐5 catalyst. *Catalysis letters* **1999,** *63*, 73-77.

(29) Zhang, C.-L.; Li, S.; Yuan, Y.; Zhang, W.-X.; Wu, T.-H.; LIn, L.-W. Aromatization of methane in the absence of oxygen over Mo-based catalysts supported on different types of zeolites. *Catalysis letters* **1998,** *56*, 207-213.

(30) Wang, D.; Kan, Q.; Xu, N.; Wu, P.; Wu, T. Study on methane aromatization over MoO 3/HMCM-49 catalyst. *Catalysis today* **2004,** *93*, 75-80.

(31) Ma, D.; Shu, Y.; Cheng, M.; Xu, Y.; Bao, X. On the induction period of methane aromatization over Mo-based catalysts. *J. Catal.* **2000,** *194*, 105-114.

(32) Shu, Y.; Ohnishi, R.; Ichikawa, M. Improved methane dehydrocondensation reaction on HMCM-22 and HZSM-5 supported rhenium and molybdenum catalysts. *Appl. Catal., A* **2003,** *252*, 315-329.

(33) Xu, C.; Guan, J.; Wu, S.; Jia, M.; Wu, T.; Kan, Q. Catalytic performance of zeolite ITQ-13 with 9-and 10-member rings for methane dehydroaromation. *Reaction Kinetics, Mechanisms and Catalysis* **2010,** *99*, 193-199.

(34) Wong, S.-T.; Xu, Y.; Liu, W.; Wang, L.; Guo, X. Methane activation without using oxidants over supported Mo catalysts. *Appl. Catal., A* **1996,** *136*, 7-17.

(35) Sachtler, W. M. Metal clusters in zeolites: an intriguing class of catalysts. *Accounts of chemical research* **1993,** *26*, 383-387.

(36) Weckhuysen, B. M.; Wang, D.; Rosynek, M. P.; Lunsford, J. H. Conversion of methane to benzene over transition metal ion ZSM-5 zeolites: II. Catalyst characterization by X-ray photoelectron spectroscopy. *J. Catal.* **1998,** *175*, 347-351.

(37) Groen, J. C.; Zhu, W.; Brouwer, S.; Huynink, S. J.; Kapteijn, F.; Moulijn, J. A.; Pérez-Ramírez, J. Direct demonstration of enhanced diffusion in mesoporous ZSM-5 zeolite obtained via controlled desilication. *J. Am. Chem. Soc.* **2007,** *129*, 355-360.

(38) Chu, N.; Yang, J.; Li, C.; Cui, J.; Zhao, Q.; Yin, X.; Lu, J.; Wang, J. An unusual hierarchical ZSM-5 microsphere with good catalytic performance in methane dehydroaromatization. *Microporous Mesoporous Mater.* **2009,** *118*, 169-175.

(39) Kresge, C.; Leonowicz, M.; Roth, W.; Vartuli, J.; Beck, J. Ordered mesoporous molecular sieves synthesized by a liquid-crystal template mechanism. *nature* **1992,** *359*, 710-712.

(40) Davis, M. E. Ordered porous materials for emerging applications. *Nature* **2002,** *417*, 813-821.

(41) Van Grieken, R.; Sotelo, J.; Menendez, J.; Melero, J. Anomalous crystallization mechanism in the synthesis of nanocrystalline ZSM-5. *Microporous Mesoporous Mater.* **2000,** *39*, 135-147.

(42) Masami Yamamura, K. C., Toshiya Wakatsuki, and Hideo Okado Synthesis of ZSM-5 zeolite with small crystal size and its catalytic performance for ethylene oligomerization. *Zeolites* **1994,** *14*, 643-649.

(43) Zhang, W.; Ma, D.; Han, X.; Liu, X.; Bao, X.; Guo, X.; Wang, X. Methane dehydro-aromatization over Mo/HZSM-5 in the absence of oxygen: A multinuclear solid-state NMR study of the interaction between supported Mo species and HZSM-5 zeolite with different crystal sizes. *J. Catal.* **1999,** *188*, 393-402.

(44) Holm, M. S.; Taarning, E.; Egeblad, K.; Christensen, C. H. Catalysis with hierarchical zeolites. *Catalysis Today* **2011,** *168*, 3-16.

(45) Na, K.; Choi, M.; Ryoo, R. Recent advances in the synthesis of hierarchically nanoporous zeolites. *Microporous Mesoporous Mater.* **2013,** *166*, 3-19.

(46) Serrano, D.; Pizarro, P. Synthesis strategies in the search for hierarchical zeolites. *Chemical Society Reviews* **2013**.

(47) Groen, J. C.; Peffer, L. A. A.; Moulijn, J. A.; Pérez, R.; amp; x; rez, J. On the introduction of intracrystalline mesoporosity in zeolites upon desilication in alkaline medium. *Microporous Mesoporous Mater.* **2004,** *69*, 29-34.

(48) Groen, J. C.; Jansen, J. C.; Moulijn, J. A.; Pérez-Ramírez, J. Optimal aluminum-assisted mesoporosity development in MFI zeolites by desilication. *J. Phys. Chem. B* **2004,** *108*, 13062-13065.

(49) Verboekend, D.; Pérez-Ramírez, J. Design of hierarchical zeolite catalysts by desilication. *Catal. Sci. Technol.* **2011,** *1*, 879-890.

(50) Lu, Y.; Ma, D.; Xu, Z.; Tian, Z.; Bao, X.; Lin, L. A high coking-resistance catalyst for methane aromatization. *Chem. Commun.* **2001**, 2048-2049.

(51) Su, L.; Liu, L.; Zhuang, J.; Wang, H.; Li, Y.; Shen, W.; Xu, Y.; Bao, X. Creating mesopores in ZSM-5 zeolite by alkali treatment: a new way to enhance the catalytic performance of methane dehydroaromatization on Mo/HZSM-5 catalysts. *Catalysis letters* **2003,** *91*, 155-167.

(52) Liu, S.; Wang, L.; Ohnishi, R.; Ichikawa, M. Bifunctional catalysis of Mo/HZSM-5 in the dehydroaromatization of methane to benzene and naphthalene XAFS/TG/DTA/MASS/FTIR characterization and supporting effects. *J. Catal.* **1999,** *181*, 175-188.

(53) Groen, J. C.; Moulijn, J. A.; Pérez-Ramírez, J. Desilication: on the controlled generation of mesoporosity in MFI zeolites. *J. Mater. Chem.* **2006,** *16*, 2121-2131.

(54) Su, L.-L.; Li, Y.-G.; Shen, W.-J.; Xu, Y.-D.; Bao, X.-H. Methane dehydroaromatization over alkali-treated MCM-22 supported Mo catalysts: effects of porosity. *Studies in surface science and catalysis* **2004,** *147*, 595-600.

(55) Kucherov, A. Effect of the formation of secondary pores in zeolite ZSM-5 on the properties of molybdenum-zeolite catalysts for methane aromatization. *Russian Journal of Physical Chemistry A* **2014,** *88*, 386-392.

(56) Aboul-Gheit, A.; Awadallah, A. Non-oxidative Conversion of Natural Gas to Aromatics (GTA), Ethylene (GTE), and Hydrogen Using Mo Loaded on HZSM-5 and Hydro-fluorinated HZSM-5 Catalysts. *Energy Sources, Part A: Recovery, Utilization, and Environmental Effects* **2014,** *36*, 489-500.

(57) Song, Y.; Sun, C.; Shen, W.; Lin, L. Hydrothermal Post-synthesis of HZSM-5 Zeolite to Enhance the Coke-resistance of Mo/HZSM-5 Catalyst for Methane Dehydroaromatization. *Catalysis Letters* **2006,** *109*, 21-24.

(58) Choi, M.; Na, K.; Kim, J.; Sakamoto, Y.; Terasaki, O.; Ryoo, R. Stable single-unit-cell nanosheets of zeolite MFI as active and long-lived catalysts. *Nature* **2009,** *461*, 246-249.

(59) Na, K.; Jo, C.; Kim, J.; Cho, K.; Jung, J. Directing zeolite structures into hierarchically nanoporous architectures. *Science (New York, N.Y.)* **2011,** *333*, 328-332.

(60) Corma, A.; Fornes, V.; Pergher, S.; Maesen, T. L.; Buglass, J. Delaminated zeolite precursors as selective acidic catalysts. *Nature* **1998,** *396*, 353-356.

(61) Corma, A.; Fornes, V.; Martınez-Triguero, J.; Pergher, S. Delaminated zeolites: Combining the benefits of zeolites and mesoporous materials for catalytic uses. *J. Catal.* **1999,** *186*, 57-63.

(62) Wu, Y.; Emdadi, L.; Wang, Z.; Fan, W.; Liu, D. Textural and catalytic properties of Mo loaded hierarchical meso-/microporous lamellar MFI and MWW zeolites for direct methane conversion. *Appl. Catal., A* **2014,** *470*, 344-354.

(63) Schmidt, I.; Boisen, A.; Gustavsson, E.; Ståhl, K.; Pehrson, S.; Dahl, S.; Carlsson, A.; Jacobsen, C. J. Carbon nanotube templated growth of mesoporous zeolite single crystals. *Chem. Mater.* **2001,** *13*, 4416-4418.

(64) Jacobsen, C. J.; Madsen, C.; Houzvicka, J.; Schmidt, I.; Carlsson, A. Mesoporous zeolite single crystals. *J. Am. Chem. Soc.* **2000,** *122*, 7116-7117.

(65) Fan, W.; Snyder, M. A.; Kumar, S.; Lee, P.-S.; Yoo, W. C.; McCormick, A. V.; Penn, R. L.; Stein, A.; Tsapatsis, M. Hierarchical nanofabrication of microporous crystals with ordered mesoporosity. *Nat. Mater.* **2008,** *7*, 984-991.

(66) Liu, H.; Yang, S.; Hu, J.; Shang, F.; Li, Z.; Xu, C.; Guan, J.; Kan, Q. A comparison study of mesoporous Mo/H-ZSM-5 and conventional Mo/H-ZSM-5 catalysts in methane non-oxidative aromatization. *Fuel Processing Technology* **2012,** *96*, 195-202.

(67) Martínez, A.; Peris, E.; Derewinski, M.; Burkat-Dulak, A. Improvement of catalyst stability during methane dehydroaromatization (MDA) on Mo/HZSM-5 comprising intracrystalline mesopores. *Catalysis Today* **2011,** *169*, 75-84.

(68) Borry, R. W.; Kim, Y. H.; Huffsmith, A.; Reimer, J. A.; Iglesia, E. Structure and density of Mo and acid sites in Mo-exchanged H-ZSM5 catalysts for nonoxidative methane conversion. *The Journal of Physical Chemistry B* **1999,** *103*, 5787-5796.

(69) Cheng, X.-w.; Meng, Q.-y.; Chen, J.-y.; Long, Y.-c. A facile route to synthesize mesoporous ZSM-5 zeolite incorporating high ZnO loading in mesopores. *Microporous Mesoporous Mater.* **2012,** *153*, 198-203.

(70) Biscardi, J. A.; Iglesia, E. Reaction pathways and rate-determining steps in reactions of alkanes on H-ZSM5 and Zn/H-ZSM5 catalysts. *J. Catal.* **1999,** *182*, 117-128.

(71) Guczi, L.; Kiricsi, I. Zeolite supported mono-and bimetallic systems: structure and performance as CO hydrogenation catalysts. *Appl. Catal., A* **1999,** *186*, 375-394.

(72) Lacheen, H. S.; Iglesia, E. Isothermal activation of Mo 2 O 5 2+–ZSM-5 precursors during methane reactions: effects of reaction products on structural evolution and catalytic properties. *Physical Chemistry Chemical Physics* **2005,** *7*, 538-547.

(73) Bourlinos, A. B.; Zboril, R.; Petridis, D. A simple route towards magnetically modified zeolites. *Microporous Mesoporous Mater.* **2003,** *58*, 155-162.

(74) Wang, D.; Lunsford, J. H.; Rosynek, M. P. Characterization of a Mo/ZSM-5 Catalyst for the Conversion of Methane to Benzene. *J. Catal.* **1997,** *169*, 347-358.

(75) Matus, E. V.; Ismagilov, I. Z.; Sukhova, O. B.; Zaikovskii, V. I.; Tsikoza, L. T.; Ismagilov, Z. R.; Moulijn, J. A. Study of Methane Dehydroaromatization on Impregnated Mo/ZSM-5 Catalysts and Characterization of Nanostructured Molybdenum Phases and Carbonaceous Deposits. *Industrial & Engineering Chemistry Research* **2006,** *46*, 4063-4074.

(76) Kikuchi, S.; Kojima, R.; Ma, H.; Bai, J.; Ichikawa, M. Study on Mo/HZSM-5 catalysts modified by bulky aminoalkyl-substituted silyl compounds for the selective methane-to-benzene (MTB) reaction. *J. Catal.* **2006,** *242*, 349-356.

(77) Ding, W.; Meitzner, G. D.; Iglesia, E. The effects of silanation of external acid sites on the structure and catalytic behavior of Mo/H–ZSM5. *J. Catal.* **2002,** *206*, 14-22.

(78) Satterfield, C. N. Heterogeneous catalysis in industrial practice. **1991**.

(79) Liu, H.; Shen, W.; Bao, X.; Xu, Y. Methane dehydroaromatization over Mo/HZSM-5 catalysts: The reactivity of MoC x species formed from MoO x associated and non-associated with Brönsted acid sites. *Appl. Catal., A* **2005,** *295*, 79-88.

(80) Liu, H.; Shen, W.; Bao, X.; Xu, Y. Identification of Mo active species for methane dehydro-aromatization over Mo/HZSM-5 catalysts in the absence of oxygen: 1 H MAS NMR and EPR investigations. *Journal of Molecular Catalysis A: Chemical* **2006,** *244*, 229-236.

(81) Liu, Z.; Nutt, M. A.; Iglesia, E. The effects of CO2, CO and H2 co-reactants on methane reactions catalyzed by Mo/H-ZSM-5. *Catalysis letters* **2002,** *81*, 271-279.

(82) Li, S.; Zhang, C.; Kan, Q.; Wang, D.; Wu, T.; Lin, L. The function of Cu (II) ions in the Mo/CuH-ZSM-5 catalyst for methane conversion under non-oxidative condition. *Appl. Catal., A* **1999,** *187*, 199-206.

(83) Burns, S.; Hargreaves, J.; Pal, P.; Parida, K.; Parija, S. The effect of dopants on the activity of MoO 3/ZSM-5 catalysts for the dehydroaromatisation of methane. *Catalysis today* **2006,** *114*, 383-387.

(84) Wang, L.; Xu, Y.; Wong, S.-T.; Cui, W.; Guo, X. Activity and stability enhancement of MoHZSM-5-based catalysts for methane non-oxidative transformation to aromatics and C2 hydrocarbons: Effect of additives and pretreatment conditions. *Appl. Catal., A* **1997,** *152*, 173-182.

(85) Xiong, Z.-T.; Chen, L.-L.; Zhang, H.-B.; Zeng, J.-L.; Lin, G.-D. Study of W/HZSM-5-based catalysts for dehydro-aromatization of CH4 in absence of O2. I. Performance of catalysts. *Catalysis letters* **2001,** *74*, 227-232.

(86) Hassan, A.; Sayari, A. Highly active, selective and stable Mo/Ru-HZSM-5 catalysts for oxygen-free methane aromatization. *Appl. Catal., A* **2006,** *297*, 159-164.

(87) Sily, P. D.; Noronha, F. B.; Passos, F. B. Methane direct conversion on Mo/ZSM-5 catalysts modified by Pd and Ru. *Journal of Natural Gas Chemistry* **2006,** *15*, 82-86.

(88) Vosmerikov, A.; Zaikovskii, V.; Korobitsyna, L.; Echevskii, G.; Kozlov, V.; Barbashin, Y. E.; Zhuravkov, S. Nonoxidative conversion of methane into aromatic hydrocarbons on Ni-Mo/ZSM-5 catalysts. *Kinetics and Catalysis* **2009,** *50*, 725-733.

(89) Masiero, S. S.; Marcilio, N. R.; Perez-Lopez, O. W. Aromatization of methane over Mo-Fe/ZSM-5 catalysts. *Catal. Lett.* **2009,** *131*, 194-202.

(90) Chen, L.; Lin, L.; Xu, Z.; Zhang, T.; Li, X. Promotional effect of Pt on non-oxidative methane transformation over Mo-HZSM-5 catalyst. *Catalysis letters* **1996,** *39*, 169-172.

(91) Liu, B.; Zhang, Y.; Liu, J.; Tian, M.; Zhang, F.; Au, C.; Cheung, A.-C. Characteristic and mechanism of methane dehydroaromatization over Zn-based/HZSM-5 catalysts under conditions of atmospheric pressure and supersonic jet expansion. *The Journal of Physical Chemistry C* **2011,** *115*, 16954-16962.

(92) Zeng, J. L.; Xiong, Z. T.; Zhang, H. B.; Lin, G. D.; Tsai, K. Nonoxidative dehydrogenation and aromatization of methane over W/HZSM‐5‐based catalysts. *Catalysis letters* **1998,** *53*, 119-124.

(93) Weckhuysen, B. M.; Wang, D.; Rosynek, M. P.; Lunsford, J. H. Catalytic Conversion of Methane into Aromatic Hydrocarbons over Iron Oxide Loaded ZSM‐5 Zeolites. *Angewandte Chemie International Edition in English* **1997,** *36*, 2374-2376.

(94) Wang, L.; Ohnishi, R.; Ichikawa, M. Novel rhenium‐based catalysts for dehydrocondensation of methane with CO/CO2 towards ethylene and benzene. *Catalysis letters* **1999,** *62*, 29-33.

(95) Abdelsayed, V.; Shekhawat, D.; Smith, M. W. Effect of Fe and Zn promoters on Mo/HZSM-5 catalyst for methane dehydroaromatization. *Fuel* **2015,** *139*, 401-410.

(96) Solymosi, F.; Szöke, A.; Cserenyi, J. Conversion of methane to benzene over Mo2C and Mo2C/ZSM-5 catalysts. *Catalysis letters* **1996,** *39*, 157-161.

(97) Ma, H.; Kojima, R.; Ohnishi, R.; Ichikawa, M. Efficient regeneration of Mo/HZSM-5 catalyst by using air with NO in methane dehydro-aromatization reaction. *Appl. Catal., A* **2004,** *275*, 183-187.

(98) Honda, K.; Yoshida, T.; Zhang, Z.-G. Methane dehydroaromatization over Mo/HZSM-5 in periodic CH< sub> 4</sub>–H< sub> 2</sub> switching operation mode. *Catalysis Communications* **2003,** *4*, 21-26.

(99) Rinaldi, R.; Schüth, F. Design of solid catalysts for the conversion of biomass. *Energy Environ. Sci.* **2009,** *2*, 610-626.

(100) Tanabe, K.; Hölderich, W. F. Industrial application of solid acid–base catalysts. *Appl. Catal., A* **1999,** *181*, 399-434.

(101) Serrano, D.; Pizarro, P. Synthesis strategies in the search for hierarchical zeolites. *Chem. Soc. Rev.* **2013,** *42*, 4004-4035.

(102) Groen, J.; Peffer, L. A.; Moulijn, J.; Pérez-Ramí, J. On the introduction of intracrystalline mesoporosity in zeolites upon desilication in alkaline medium. *Microporous Mesoporous Mater.* **2004,** *69*, 29-34.

(103) Groen, J. C.; Jansen, J. C.; Moulijn, J. A.; Pérez-Ramírez, J. Optimal aluminum-assisted mesoporosity development in MFI zeolites by desilication. *J. Phys. Chem. B* **2004,** *108*, 13062-13065.

(104) Garcés, J. M.; Olken, M. M.; Lee, G. J.; Meima, G. R.; Jacobs, P. A.; Martens, J. A. Shape Selective Chemistries with Modified Mordenite Zeolites. *Top. Catal.* **2009,** *52*, 1175-1181.

(105) Chaikittisilp, W.; Suzuki, Y.; Mukti, R. R.; Suzuki, T.; Sugita, K.; Itabashi, K.; Shimojima, A.; Okubo, T. Formation of Hierarchically Organized Zeolites by Sequential Intergrowth. *Angew. Chem. Int. Ed.* **2013,** *125*, 3439-3443.

(106) Zhang, X.; Liu, D.; Xu, D.; Asahina, S.; Cychosz, K. A.; Agrawal, K. V.; Al Wahedi, Y.; Bhan, A.; Al Hashimi, S.; Terasaki, O. Synthesis of self-pillared zeolite nanosheets by repetitive branching. *Science* **2012,** *336*, 1684-1687.

(107) Choi, M.; Cho, H. S.; Srivastava, R.; Venkatesan, C.; Choi, D.-H.; Ryoo, R. Amphiphilic organosilane-directed synthesis of crystalline zeolite with tunable mesoporosity. *Nat. Mater.* **2006,** *5*, 718-723.

(108) El-Malki, E.-M.; Van Santen, R.; Sachtler, W. Introduction of Zn, Ga, and Fe into HZSM-5 cavities by sublimation: Identification of acid sites. *J. Phys. Chem. B* **1999,** *103*, 4611-4622.

(109) Pérez-Ramírez, J.; Santhosh Kumar, M.; Brückner, A. Reduction of N< sub> 2</sub> O with CO over FeMFI zeolites: influence of the preparation method on the iron species and catalytic behavior. *J. Catal.* **2004,** *223*, 13-27.

(110) Laursen, A. B.; Højholt, K. T.; Lundegaard, L. F.; Simonsen, S. B.; Helveg, S.; Schüth, F.; Paul, M.; Grunwaldt, J. D.; Kegnæs, S.; Christensen, C. H. Substrate Size ‐ Selective Catalysis with Zeolite ‐ Encapsulated Gold Nanoparticles. *Angew. Chem. Int. Ed.* **2010,** *122*, 3582-3585.

(111) Shan, W.; Yu, T.; Wang, B.; Hu, J.; Zhang, Y.; Wang, X.; Tang, Y. Magnetically separable nanozeolites: promising candidates for bio-applications. *Chem. Mater.* **2006,** *18*, 3169-3172.

(112) Li, B.; Sun, B.; Qian, X.; Li, W.; Wu, Z.; Sun, Z.; Qiao, M.; Duke, M.; Zhao, D. In-Situ Crystallization Route to Nanorod-Aggregated Functional ZSM-5 Microspheres. *J. Am. Chem. Soc.* **2013,** *135*, 1181-1184.

(113) Choi, M.; Wu, Z.; Iglesia, E. Mercaptosilane-assisted synthesis of metal clusters within zeolites and catalytic consequences of encapsulation. *J. Am. Chem. Soc.* **2010,** *132*, 9129-9137.

(114) Bian, S.-W.; Mudunkotuwa, I. A.; Rupasinghe, T.; Grassian, V. H. Aggregation and dissolution of 4 nm ZnO nanoparticles in aqueous environments: influence of pH, ionic strength, size, and adsorption of humic acid. *Langmuir* **2011,** *27*, 6059-6068.

(115) Krebs, F. C.; Thomann, Y.; Thomann, R.; Andreasen, J. W. A simple nanostructured polymer/ZnO hybrid solar cell—preparation and operation in air. *Nanotechnology* **2008,** *19*, 424013.

(116) Seow, Z.; Wong, A.; Thavasi, V.; Jose, R.; Ramakrishna, S.; Ho, G. Controlled synthesis and application of ZnO nanoparticles, nanorods and nanospheres in dye-sensitized solar cells. *Nanotechnology* **2009,** *20*, 045604.

(117) Dahlberg, K. A.; Schwank, J. W. Synthesis of Ni@ SiO2 nanotube particles in a water-in-oil microemulsion template. *Chem. Mater.* **2012,** *24*, 2635-2644.

(118) Groen, J. C.; Peffer, L. A.; Pérez-Ramírez, J. Pore size determination in modified micro- and mesoporous materials. Pitfalls and limitations in gas adsorption data analysis. *Microporous Mesoporous Mater.* **2003,** *60*, 1-17.

(119) Groen, J. C.; Pérez-Ramírez, J. Critical appraisal of mesopore characterization by adsorption analysis. *Appl. Catal., A* **2004,** *268*, 121-125.

(120) Tarazona, P.; Marconi, U. M. B.; Evans, R. Phase equilibria of fluid interfaces and confined fluids: non-local versus local density functionals. *Molecular Physics* **1987,** *60*, 573-595.

(121) Tarazona, P. Free-energy density functional for hard spheres. *Physical Review A* **1985,** *31*, 2672.

(122) Stöber, W.; Fink, A.; Bohn, E. Controlled growth of monodisperse silica spheres in the micron size range. *J. Colloid Interface Sci.* **1968,** *26*, 62-69.

(123) Meulenkamp, E. A. Synthesis and growth of ZnO nanoparticles. *J. Phys. Chem. B* **1998,** *102*, 5566-5572.

(124) Chen, J.; Feng, Z.; Ying, P.; Li, C. ZnO clusters encapsulated inside micropores of zeolites studied by UV Raman and laser-induced luminescence spectroscopies. *J. Phys. Chem. B* **2004,** *108*, 12669-12676.

(125) Spanhel, L.; Anderson, M. A. Semiconductor clusters in the sol-gel process: quantized aggregation, gelation, and crystal growth in concentrated zinc oxide colloids. *J. Am. Chem. Soc.* **1991,** *113*, 2826-2833.

(126) Cho, H. S.; Miyasaka, K.; Kim, H.; Kubota, Y.; Takata, M.; Kitagawa, S.; Ryoo, R.; Terasaki, O. Study of argon gas adsorption in ordered mesoporous mfi zeolite framework. *J. Phys. Chem. C* **2012,** *116*, 25300-25308.

(127) Cundy, C. S.; Cox, P. A. The hydrothermal synthesis of zeolites: Precursors, intermediates and reaction mechanism. *Microporous Mesoporous Mater.* **2005,** *82*, 1-78.

(128) Mullin, J. W., *Crystallization*. Butterworth-Heinemann: 2001.

(129) Lai, Y.; Veser, G. Zn-HZSM5 Catalysts for Methane Dehyroaromatization. *Environ. Prog. Sustain. Energy* **2015**, in review.

(130) Liu, S.; Wang, L.; Dong, Q.; Ohnishi, R.; Ichikawa, M. Catalytic dehydroaromatization of methane with CO/CO2 towards benzene and naphthalene on bimetallic Mo/zeolite catalysts: Bifunctional catalysis and dynamic mechanism. *Stud. Surf. Sci. Catal.* **1998**, 241-246.

(131) Szöke, A.; Solymosi, F. Selective oxidation of methane to benzene over K< sub> 2</sub> MoO< sub> 4</sub>/ZSM-5 catalysts. *Appl. Catal., A* **1996,** *142*, 361-374.

(132) Ma, S.; Guo, X.; Zhao, L.; Scott, S.; Bao, X. Recent progress in methane dehydroaromatization: From laboratory curiosities to promising technology. *J. Energy Chem.* **2013,** *22*, 1-20.

(133) Biscardi, J. A.; Iglesia, E. Structure and function of metal cations in light alkane reactions catalyzed by modified H-ZSM5. *Catalysis today* **1996,** *31*, 207-231.

(134) Biscardi, J. A.; Meitzner, G. D.; Iglesia, E. Structure and density of active Zn species in Zn/H-ZSM5 propane aromatization catalysts. *J. Catal.* **1998,** *179*, 192-202.

(135) Berndt, H.; Lietz, G.; Lücke, B.; Völter, J. Zinc promoted H-ZSM-5 catalysts for conversion of propane to aromatics I. Acidity and activity. *Appl. Catal., A* **1996,** *146*, 351-363.

(136) Gabrienko, A. A.; Arzumanov, S. S.; Freude, D.; Stepanov, A. G. Propane Aromatization on Zn-Modified Zeolite BEA Studied by Solid-State NMR in Situ. *J. Phys. Chem. C* **2010,** *114*, 12681-12688.

(137) Berndt, H.; Lietz, G.; Völter, J. Zinc promoted H-ZSM-5 catalysts for conversion of propane to aromatics II. Nature of the active sites and their activation. *Appl. Catal., A* **1996,** *146*, 365-379.

(138) Almutairi, S. M.; Mezari, B.; Magusin, P. C.; Pidko, E. A.; Hensen, E. J. Structure and reactivity of Zn-modified ZSM-5 zeolites: the importance of clustered cationic Zn complexes. *ACS Catalysis* **2011,** *2*, 71-83.

(139) Matus, E. V.; Ismagilov, I. Z.; Sukhova, O. B.; Zaikovskii, V. I.; Tsikoza, L. T.; Ismagilov, Z. R.; Moulijn, J. A. Study of methane dehydroaromatization on impregnated Mo/ZSM-5 catalysts and characterization of nanostructured molybdenum phases and carbonaceous deposits. *Industrial & engineering chemistry research* **2007,** *46*, 4063-4074.

(140) Tan, P.; Au, C.; Lai, S. Methane dehydrogenation and aromatization over 4 wt% Mn/HZSM-5 in the absence of an oxidant. *Catal. Lett.* **2006,** *112*, 239-245.

(141) Xiong, Z.-T.; Zhang, H.-B.; Lin, G.-D.; Zeng, J.-L. Study of W/HZSM-5-based catalysts for dehydro-aromatization of CH4 in absence of O2. II. Action of promoters Zn and Li. *Catal. Lett.* **2001,** *74*, 233-239.

(142) Lai, Y.; Rutigliano, M. N.; Veser, G. Controlled Embedding of Metal Oxide Nanoparticles in ZSM-5 Zeolites through Pre-encapsulation and Timed Release. *Langmuir* **2015**.

(143) Niu, X.; Gao, J.; Miao, Q.; Dong, M.; Wang, G.; Fan, W.; Qin, Z.; Wang, J. Influence of preparation method on the performance of Zn-containing HZSM-5 catalysts in methanol-to-aromatics. *Microporous Mesoporous Mater.* **2014,** *197*, 252-261.

(144) Penzien, J.; Abraham, A.; van Bokhoven, J. A.; Jentys, A.; Müller, T. E.; Sievers, C.; Lercher, J. A. Generation and characterization of well-defined Zn2+ Lewis acid sites in ion exchanged zeolite BEA. *J. Phys. Chem. B* **2004,** *108*, 4116-4126.

(145) Cui, Y.; Xu, Y.; Lu, J.; Suzuki, Y.; Zhang, Z.-G. The effect of zeolite particle size on the activity of Mo/HZSM-5 in non-oxidative methane dehydroaromatization. *Appl. Catal., A* **2011,** *393*, 348-358.

(146) Kazansky, V.; Borovkov, V. Y.; Serikh, A.; Van Santen, R.; Anderson, B. Nature of the sites of dissociative adsorption of dihydrogen and light paraffins in ZnHZSM-5 zeolite prepared by incipient wetness impregnation. *Catal. Lett.* **2000,** *66*, 39-47.

(147) Cao, A.; Veser, G. Exceptional high-temperature stability through distillation-like self-stabilization in bimetallic nanoparticles. *Nat. Mater.* **2010,** *9*, 75-81.

(148) Asche, F.; Oglend, A.; Osmundsen, P. Gas versus oil prices the impact of shale gas. *Energy Policy* **2012,** *47*, 117-124.

(149) Ding, W.; Li, S.; D Meitzner, G.; Iglesia, E. Methane conversion to aromatics on Mo/H-ZSM5: structure of molybdenum species in working catalysts. *The Journal of Physical Chemistry B* **2001,** *105*, 506-513.

(150) Ding, W.; Meitzner, G. D.; Marler, D. O.; Iglesia, E. Synthesis, structural characterization, and catalytic properties of tungsten-exchanged H-ZSM5. *The Journal of Physical Chemistry B* **2001,** *105*, 3928-3936.

(151) Smith, K. S.; Huyck, H. L. An overview of the abundance, relative mobility, bioavailability, and human toxicity of metals. *The environmental geochemistry of mineral deposits* **1999,** *6*, 29-70.

(152) Elements, Terrestrial Abundance. *www.daviddarling.info* **Retrieved 2015-09-23**.

(153) Guo, X.; Fang, G.; Li, G.; Ma, H.; Fan, H.; Yu, L.; Ma, C.; Wu, X.; Deng, D.; Wei, M. Direct, nonoxidative conversion of methane to ethylene, aromatics, and hydrogen. *Science* **2014,** *344*, 616-619.

(154) Pérez-Ramírez, J.; Mul, G.; Kapteijn, F.; Moulijn, J.; Overweg, A.; Doménech, A.; Ribera, A.; Arends, I. Physicochemical characterization of isomorphously substituted FeZSM-5 during activation. *J. Catal.* **2002,** *207*, 113-126.

(155) Berlier, G.; Zecchina, A.; Spoto, G.; Ricchiardi, G.; Bordiga, S.; Lamberti, C. The role of Al in the structure and reactivity of iron centers in Fe-ZSM-5-based catalysts: a statistically based infrared study. *J. Catal.* **2003,** *215*, 264-270.

(156) Mul, G.; Perez-Ramirez, J.; Kapteijn, F.; Moulijn, J. NO adsorption on ex-framework [Fe, X] MFI catalysts: novel IR bands and evaluation of assignments. *Catal. Lett.* **2002,** *80*, 129-138.

(157) Chen, H.-Y.; Sachtler, W. M. Activity and durability of Fe/ZSM-5 catalysts for lean burn NO x reduction in the presence of water vapor. *Catal. Today* **1998,** *42*, 73-83.

(158) Inamura, K.; Iwamoto, R.; Iino, A.; Takyu, T. Reduction and sulfidation properties of iron species in iron-supported Y-zeolite by temperature-programmed reduction and sulfiding. *J. Catal.* **1993,** *142*, 274-288.

(159) Krishna, K.; Seijger, G.; Van den Bleek, C.; Makkee, M.; Mul, G.; Calis, H. Selective catalytic reduction of NO with NH3 over Fe-ZSM-5 catalysts prepared by sublimation of FeCl3 at different temperatures. *Catal. Lett.* **2003,** *86*, 121-132.

(160) Delahay, G.; Valade, D.; Guzmán-Vargas, A.; Coq, B. Selective catalytic reduction of nitric oxide with ammonia on Fe-ZSM-5 catalysts prepared by different methods. *Applied Catalysis B: Environmental* **2005,** *55*, 149-155.

(161) Groen, J.; Brückner, A.; Berrier, E.; Maldonado, L.; Moulijn, J.; Pérez-Ramírez, J. Iron site modification upon alkaline treatment of Fe-ZSM-5 zeolites—Opportunities for improved N 2 O decomposition activity. *J. Catal.* **2006,** *243*, 212-216.

(162) Sun, K.; Xia, H.; Feng, Z.; van Santen, R.; Hensen, E.; Li, C. Active sites in Fe/ZSM-5 for nitrous oxide decomposition and benzene hydroxylation with nitrous oxide. *J. Catal.* **2008,** *254*, 383-396.

(163) Marturano, P.; Drozdová, L.; Pirngruber, G. D.; Kogelbauer, A.; Prins, R. The mechanism of formation of the Fe species in Fe/ZSM-5 prepared by CVD. *PCCP* **2001,** *3*, 5585-5595.

(164) Pérez-Ramírez, J.; Kumar, M. S.; Brückner, A. Reduction of N 2 O with CO over FeMFI zeolites: influence of the preparation method on the iron species and catalytic behavior. *J. Catal.* **2004,** *223*, 13-27.

(165) Selvam, P.; Dapurkar, S.; Badamali, S.; Murugasan, M.; Kuwano, H. Coexistence of paramagnetic and superparamagnetic Fe (III) in mesoporous MCM-41 silicates. *Catal. Today* **2001,** *68*, 69-74.

(166) Wang, H.; Tan, D.; Xu, Y.; Bao, X. Effect of Silanation of HZSM-5 Zeolite on Catalytic Performance of Mo/HZSM-5 in Methane Dehydroaromatization. *Chinese Journal of Catalysis* **2004,** *25*, 445-449.

(167) Weckhuysen, B.; Rosynek, M.; Lunsford, J. Characterization of surface carbon formed during the conversion of methane to benzene over Mo/H-ZSM-5 catalysts. *Catalysis Letters* **1998,** *52*, 31-36.

(168) Liu, H.; Su, L.; Wang, H.; Shen, W.; Bao, X.; Xu, Y. The chemical nature of carbonaceous deposits and their role in methane dehydro-aromatization on Mo/MCM-22 catalysts. *Appl. Catal., A* **2002,** *236*, 263-280.

(169) Han, S.; Shihabi, D. S.; Chang, C. D. Selective removal of surface acidity in ZSM-5 zeolite using (NH 4) 2 SiF 6 treatment. *J. Catal.* **2000,** *196*, 375-378.

(170) Kerr, G. T.; Chester, A. W. Quantitative thermoanalysis of evolved ammonia. Application to ammonium zeolite Y and some transition metal ammine chlorides. *Thermochimica Acta* **1971,** *3*, 113-124.

(171) Pérez-Ramıīrez, J.; Verboekend, D.; Bonilla, A.; Abelló, S. Zeolite catalysts with tunable hierarchy factor by pore-growth moderators. *Adv. Funct. Mater* **2009,** *19*, 3972-3979.

(172) Schweitzer, N. M.; Hu, B.; Das, U.; Kim, H.; Greeley, J.; Curtiss, L. A.; Stair, P. C.; Miller, J. T.; Hock, A. S. Propylene hydrogenation and propane dehydrogenation by a single-site Zn2+ on silica catalyst. *Acs Catalysis* **2014,** *4*, 1091-1098.

(173) Hu, B.; Schweitzer, N. M.; Das, U.; Kim, H.; Niklas, J.; Poluektov, O.; Curtiss, L. A.; Stair, P. C.; Miller, J. T.; Hock, A. S. Selective propane dehydrogenation with single-site Co II on SiO 2 by a non-redox mechanism. *J. Catal.* **2015,** *322*, 24-37.

(174) Hu, B.; Schweitzer, N. M.; Zhang, G.; Kraft, S. J.; Childers, D. J.; Lanci, M. P.; Miller, J. T.; Hock, A. S. Isolated FeII on silica as a selective propane dehydrogenation catalyst. *ACS Catalysis* **2015**.

(175) Nakata, K.; Yamaoka, Y.; Miyata, T.; Taniguchi, Y.; Takaki, K.; Fujiwara, Y. Palladium (II) and/or copper (II)-catalyzed carboxylation of small alkanes such as methane and ethane with carbon monoxide. *Journal of organometallic chemistry* **1994,** *473*, 329-334.

(176) Au, C.; Hu, Y.; Wan, H. Methane activation over unsupported and La2O3-supported copper and nickel catalysts. *Catalysis letters* **1996,** *36*, 159-163.

(177) Yan, Q.; Weng, W.; Wan, H.; Toghiani, H.; Toghiani, R.; Pittman, C. Activation of methane to syngas over a Ni/TiO 2 catalyst. *Appl. Catal., A* **2003,** *239*, 43-58.

(178) Williams, L. A.; Guo, N.; Motta, A.; Delferro, M.; Fragalà, I. L.; Miller, J. T.; Marks, T. J. Surface structural-chemical characterization of a single-site d0 heterogeneous arene hydrogenation catalyst having 100% active sites. *Proceedings of the National Academy of Sciences* **2013,** *110*, 413-418.

(179) Mamedov, E.; Corberán, V. C. Oxidative dehydrogenation of lower alkanes on vanadium oxide-based catalysts. The present state of the art and outlooks. *Appl. Catal., A* **1995,** *127*, 1-40.

(180) Gajan, D.; Copéret, C. Silica-supported single-site catalysts: to be or not to be? A conjecture on silica surfaces. *New Journal of Chemistry* **2011,** *35*, 2403-2408.